ABSTRACT

INTERMITTENT DYNAMICS OF DENSE PARTICULATE MATTER

by
Chao Cheng

Granular particle systems are scattered around the universe, and they can behave like solids when there exist strong force-bearing networks, so that the granular system can resist certain stress without deformation. When such a network is not present, particles yield to small stress and behave like a fluid. A wide range of systems exhibit intermittent dynamics as they are slowly loaded, with different dynamical regimes governing many industrial and natural phenomena. While a significant amount of research on exploring intermittent dynamics of granular systems has been carried out, not much is known about the connection between particle-scale response and the global dynamics. In this work, four different types of systems are investigated both through experiments and numerical simulations to reveal the connection.

At the beginning of this work, a spherical intruder is considered, which is initially buried in a granular column exposed to an upward pullout force. Analysis of the interparticle forces, using both classical and novel methods based on persistent homology, uncovers the details of the failure process. The intruder and the granular particles are essentially static before failure, however, the force network that includes the information about the particle contacts goes through significant changes. The failure occurs through a culmination of temporally intermittent changes that take place predominantly in the proximity to the intruder.

Next, experiments involving a slider moving on top of granular media consisting of photo-elastic particles in two dimensions are investigated. Such systems exhibit various dynamics, from continuous motion to crackling, and stick-slip type of behavior. By applying image analysis and persistence homology, a clear correlation between the slider dynamics and the response of the force network properties is revealed. Furthermore, the

correlation is particularly strong in the dynamical regime characterized by well-defined stick-slip type of dynamics.

The stick-slip dynamics of dense granular systems is further investigated via two dimensional discrete element simulations. The focus of this work is understanding what type of information is needed to be able to predict upcoming events. Both static and dynamic measures are considered. The static measures are obtained from observing the state of the system at a given time, while dynamic measures are obtained by considering the information from system evolution. A set of dynamic measures is identified with a promise to predict slip events.

Finally, the intermittent dynamics of a dense granular system, exposed to slow compression and decompression in three spatial dimensions, is considered. Both compression and decompression involve transitional events involving fast irreversible transitions which are not always associated with rearrangement of particles and contact networks. The analysis of the force networks using the tools of persistent homology shows that the evolution of pressure is strongly correlated with the evolution of the topological measures quantifying loops in the force networks. Frictional effects are found to smoothen system evolution and to decrease both the amplitude and the duration of the transition events that occur during compression or decompression.

INTERMITTENT DYNAMICS OF DENSE PARTICULATE MATTER

by
Chao Cheng

A Dissertation
Submitted to the Faculty of
New Jersey Institute of Technology and
Rutgers, The State University of New Jersey – Newark
in Partial Fulfillment of the Requirements for the Degree of
Doctor of Philosophy in Mathematical Sciences

Department of Mathematical Sciences
Department of Mathematics and Computer Science, Rutgers-Newark

May 2021

APPROVAL PAGE

INTERMITTENT DYNAMICS OF DENSE PARTICULATE MATTER

Chao Cheng

Dr. Lou Kondic, Dissertation Advisor — Date
Distinguished Professor of Applied Mathematics, NJIT

Dr. Denis L. Blackmore, Committee Member — Date
Professor of Mathematical Sciences, NJIT

Dr. Abram H. Clark IV, Committee Member — Date
Assistant Professor of Physics, Naval Postgraduate School, Monterey, CA

Dr. Konstantin M. Mischaikow, Committee Member — Date
Professor of Mathematics, Rutgers, The State University of New Jersey, Piscataway, NJ

Dr. Richard O. Moore, Committee Member — Date
Director of Programs and Services, Society for Industrial and Applied Mathematics (SIAM), Philadelphia, PA

BIOGRAPHICAL SKETCH

Author: Chao Cheng

Degree: Doctor of Philosophy

Date: May 2021

Undergraduate and Graduate Education:

- Doctor of Philosophy in Mathematical Sciences,
  New Jersey Institute of Technology, Newark, NJ, 2021
- Master of Science in Applied Mathematics,
  China University of Petroleum (Beijing), Beijing, China, 2015
- Bachelor of Economics in International Economics and Trade,
  Huazhong University of Science and Technology, Wuhan, China, 2012

Major: Mathematical Sciences

Presentations and Publications:

C. Cheng, A. Abed Zadeh, and L. Kondic, "Correlating the force network evolution and dynamics in slider experiments," *European Physical Journal Web of Conferences*, accepted, 2021

S. Shah, C. Cheng, P. Jalali, and L. Kondic, "Failure of confined granular media due to pullout of an intruder: from force networks to a system wide response," *Soft Matter*, vol. 16, pp 7685, 2020

C. Cheng, "The precursors to stick-slip events in sheared granular systems," *Poster Presentation*, 4th International Conference on Packing Problem, New Haven, CT, Yale University, June 2019

C. Cheng, "The precursors to stick-slip events in sheared granular systems," *Contributed Talk*, 16th Annual Conference on Frontiers in Applied and Computational Mathematics,11th Northeastern Complex Fluids and Soft Matter Workshop, Newark, NJ, NJIT, May 2019

C. Cheng, "The precursors to stick-slip events in sheared granular systems," *Poster Presentation*, 10th Northeast Complex Fluids and Soft Matter Workshop, Piscataway, NJ, Rutgers University, January 2019

C. Cheng, "The precursors to stick-slip events in sheared granular systems," *Poster Presentation*, Gordon Conferences: Granular Matter, Easton, MA, Stonehill College, July 2018

C. Cheng, "The precursors to stick-slip events in sheared granular systems," *Contributed Talk*, 16th Annual Northeaster Granular Materials Workshop, New Haven, CT, Yale University, June 2018

To Xianxiao Li

ACKNOWLEDGMENT

I would like to give a great gratitude to my advisor, Dr. Lou Kondic, for his untiring academic guidance, inspiring wisdom and support during the whole time of my doctoral study.

I am very thankful to Dr. Denis Blackmore, Dr. Abram Clark IV, Dr. Konstantin Mischaikow, and Dr. Richard Moore for the review of my dissertation and for agreeing to be on my committee.

This work was funded in part by the Army Research Office Grant No. W911NF1810184 and the financial support from Department of Mathematical Sciences.

I am grateful to Dr. Miroslav Kramar and Dr. Stefan Luding for the help and the fruitful discussions and guidance during our collaboration.

I would also like to thank the Department of Mathematical Sciences for creating a great environment for studying and working and for the effort that to maintain the administrative support for all doctoral students.

Finally, I want to thank my closest family for the support during the time.

TABLE OF CONTENTS

TABLE OF CONTENTS
(Continued)

Chapter Page

TABLE OF CONTENTS
(Continued)

Chapter Page

LIST OF TABLES

LIST OF FIGURES

Figure **Page**

LIST OF FIGURES
(Continued)

Figure **Page**

LIST OF FIGURES
(Continued)

Figure **Page**

LIST OF FIGURES
(Continued)

Figure **Page**

LIST OF FIGURES
(Continued)

Figure **Page**

LIST OF FIGURES
(Continued)

Figure **Page**

LIST OF FIGURES
(Continued)

Figure **Page**

CHAPTER 1

INTRODUCTION

1.1 Brief History and Application

Granular particles are scattered around the universe. They can form the Saturn rings in the outer spaces, sand dunes in Sahara, or a pile of cherries in a grocery store. We encounter granular material on a day-to-day basis, from a scoop of coffee beans in the morning to a pinch of salt at dinner. Granular material can be defined as assemblies of large particles, of the size larger than about 100 μm [9], so that thermal agitation is negligible. Granular materials are dealt with on a massive scale in industry. Nearly 75% of raw material in industry is in the form of granular materials [110]. Therefore, understanding the physics of handling and storing granular material is of importance to a number of practical situations.

Granular material can behave like solid when there exists strong force-bearing networks, so that the granular system can resist certain stress without deformation. When such a network is not present, particles yield to small stress and behave like a fluid. If granular particles are sparsely scattered and rarely collide, we can think of a granular system as a gas.

The transitions of dense particulate matter between solid-like and liquid-like states, jamming and unjamming, are similar to the phase transitions between solid and liquid. Jamming is the physical process by which granular materials become rigid with increasing density [110]. The reverse of jamming transition is unjamming, which is related with earthquakes and avalanches. Both jamming and unjamming transitions of dense particulate system are still poorly understood.

Characterizing the jamming transition in granular matter has attracted significant interest [30, 32, 43, 58, 110, 111, 116, 161, 201]. The dynamics close to jamming transitions exhibits percolation of strong force network [110], and is influenced by multiple

parameters, including friction and system preparation protocols [111, 201]. To understand the transitions between jammed and unjammed states, the connection between force networks and system response in jamming transition needs to be unveiled [32].

Stick-slip behaviors of granular system can be considered as unjamming transitions from jammed states, which is related to earthquakes in nature. Several mechanical models are developed to capture the nature of earthquakes [44, 54, 65, 144]. Since the mechanical properties of granular material are related to the force networks of the systems, force network distribution is studied in many works [140, 148]. From the perspective of force networks, we can understand stick-slip transition using topology tools [58, 93, 100, 103], with a particular goal of exploring the existence of precursors to slip events.

Due the complexity of granular material, the general approach is either experimental or numerical. Results from experiments are usually processed by statistical tools. Numerical approach includes two directions, continuum methods and discrete element methods. Continuum models consider granular material as a continuum domain, assuming that the particles have infinitesimal size [110]. Continuum models can effectively describe bulk properties of granular assemblies and system dynamics on macroscale. The fundamental laws for continuum models involve conservation laws which include mass, energy, and momentum. When a granular system is inelastic, such that energy is not conserved, continuum models are more challenging to formulate. In addition, it is difficult to describe the microscale structure and properties in granular systems for continuum models. An alternative is to consider discrete models, that focus on the particle scale. Here, interactions between particles are treated explicitly, via linear or nonlinear interaction laws. Such an approach, that we will follow in this work, leads to a large number of coupled ordinary differential equations that are solved numerically. One important challenge is correlating the results of these differential equations with the collective dynamics of granular particles on the scales that are much larger than the particle size itself.

1.2 Overview

This work consists of four separate but related projects described in Chapters 2-5. The material presented in Chapters 2 and 3 has been published, and the text of the chapters is essentially the one from the published papers, with minor modifications. The material in Chapters 4-5 is still under preparation. It should be noted that such a structure leads to some repetitions of the background material and some minor differences in the notation.

In Chapter 2, based on our published work [158], in collaboration with Drs. Srujal Shah and Payman Jalali from Lappeenranta-Lahti University of Technology, Finland, we investigate computationally the pullout of a spherical intruder initially buried at the bottom of a three dimensional (3D) granular column. The intruder starts to move out of the granular bed once the pulling force reaches a critical value, leading to material failure. The failure point is found to depend on the diameter of the granular column, pointing out the importance of particle-wall interactions in determining the material response. Discrete element simulations show that prior to failure, the contact network is essentially static, with only minor rearrangements of the particles. However, the force network, which includes not only the contact information, but also the information about the interaction strength, undergoes nontrivial evolution. An initial insight is obtained by considering the relative magnitudes of normal and tangential forces between the particles, and in particular the proportion of contacts that reach Coulomb threshold. More detailed understanding of the processes leading to failure is reached by the analysis of both spatial and temporal properties of the force network using the tools of persistent homology. We find that the forces between the particles undergo intermittent temporal variations ahead of the failure. In addition to this temporal intermittency, the response of the force network is found to be spatially dependent and influenced by proximity to the intruder. Furthermore, the response is modified significantly by the interaction strength, with the relevant measures describing the response showing differing behaviors for the contacts characterized by large interaction forces.

In Chapter 3, based on our work [41], in collaboration with Dr. Aghil Abed Zadeh from Duke University, which is accepted for publication the Powders & Grains proceedings (to appear 2021), we focus on the experiments involving a slider moving on top of granular media consisting of photo-elastic particles in two dimensions which have uncovered elaborate dynamics that may vary from continuous motion to crackling, periodic motion, and stick-slip type of behavior. We establish that there is a clear correlation between the slider dynamics and the response of the force network that spontaneously develop in the granular system. This correlation is established by application of the persistence homology that allows for formulation of objective measures for quantification of time-dependent force networks. We find that correlation between the slider dynamics and the force network properties is particularly strong in the dynamical regime characterized by well-defined stick-slip type of dynamics.

In Chapter 4, in collaboration with Dr. Miroslav Kramar at University of Oklahoma, we continue investigating the stick-slip dynamics of dense granular system in two dimensions (2D) via discrete element simulations. We focus on the discussion regarding what type of information is needed to be able to predict an upcoming slip event. We consider both static measures and dynamic measures. Static measures describe static properties of the system, obtained from observing the state of the system at a given time point, and dynamic measures are obtained by considering the information about system evolution. We identify a set of dynamic measures that show promise to be able to predict avalanche type of behavior in the considered system. The general pattern of the results is that dynamic information needs to be included in order for a considered measure to have a predictive power.

In Chapter 5, in collaboration with Drs. Stefan Luding and Kianoosh Taghizadeh from University of Twente, the Netherlands, we consider dense granular system in three spatial dimensions exposed to slow compression and decompression. The evolution of the granular system is nontrivial, with smooth, continuous (de)compression periods interrupted

by fast, irreversible transitions. These transitions are often, but not always, associated with rearrangement of the particles and of the contact network. The analysis of the force network that is built on top of the contact networks, shows that it is possible for the transitions to occur even if a rearrangement of the particles is absent. The analysis of the force networks, carried out using the tools of persistent homology, shows that the evolution of global measures, such as pressure, is strongly correlated with the evolution of the topological measures quantifying loops in the force networks. Frictional effects are found to lead to smoother system evolution, both decreasing the amplitude of the transition events, and decreasing their duration.

In Chapter 6, we conclude the work with summary and conclusions.

CHAPTER 2

FAILURE OF CONFINED GRANULAR MEDIA DUE AN INTRUDER

2.1 Introduction

The processes related to failure in soft solids have been explored for a long time, and in particular during last couple of decades a significant progress has been achieved; excellent review articles are available, discussing soft solids in general [62], failure in the context of fracture and avalanching [52], and related issue in the context of glass transition of amorphous materials [29], among other research directions. In the context of granular matter, the concept of failure is closely related to jamming, another topic that has produced a significant interest, see [25, 115, 117, 176] for reviews. In particular, a close connection between particle scale information, including local contact networks, and macroscale rheology of sheared or compressed granular materials, has been established. In addition, a point was made years ago [39, 40] that not only contact networks per sé are important in governing the system response, but also their strength; this point will be of particular relevance in present work.

In this chapter, we focus on a system in which the connection between contact and force networks, and material failure, can be analyzed in detail. We consider a spherical intruder, large compared to particles size, that is initially buried in a granular column. The intruder is exposed to an upward pullout force which increases with time until the material fails, similarly as considered recently in two dimensions (2D) in experiments with photoelastic particles [199], and even more recently in 3D experiments [89]. To some degree, this pull-out setup may be considered as a reverse of the impact of an object onto the surface of granular material [45, 95], although one may wonder to which degree slowing down a moving intruder is similar to the failure due to an applied force on an initially static object. Another related setup of relevance is the one of a solid rod that is pulled out of

a granular column. This setup was analyzed both computationally and experimentally, suggesting that, once the rod starts to move, shear occurring in a cylindrical shear zone surrounding the rod may lead to local jamming that increases frictional resistance [66].

After discussing general, system-wide response to applied pull-out force, we will focus in particular on the question of particle-scale response, both from static and dynamic points of view. As pointed out, even if the intruder and the granular particles are stationary, there could still be changes in the network describing mutual interactions between the granular particles, particles and the intruder, as well as particles and the walls. In the present context, such a network is weighted by the strength of the force between the particles. This strength can be quantified by either normal, tangential, or some combination of these force components. By now it has been established that the properties of such force network are crucial for the purpose of developing better understanding of granular systems in the context of analysis of static packs [196], shear [14, 58], compression [98, 100, 104], wave propagation [21, 22], or impact [165]; see also [25] for a recent review. Reaching this understanding is however complicated by the complexity of the force networks due to a large amount of time-dependent data. Obviously, some type of simplification is needed; in addition, one would like to use measures that are precisely defined and that allow for a meaningful comparison of the force networks at different time instances, since we will be also interested in a dynamic setting.

In recent years, significant progress has been made towards developing better understanding of force networks using a variety of tools, including force network ensemble analysis [153, 164, 170], statistics-based methods [33, 143, 172, 173], network type of analysis [21, 70, 82, 171, 182], and application of topological methods, more precisely persistent homology [10, 11, 12, 100, 101, 103, 104, 105, 147]; see [25, 141] for recent reviews. While different methods provide a complementary insight, we will focus here on persistent homology based approach since it allows for significant data reduction, for formulation of objective measures describing the force network, as well as for precise

comparison of different networks in a dynamic setting. Such an approach was used with success to discuss force networks for the systems that were compressed [100, 104], vibrated [101, 147], or sheared [67], as well as for the analysis of experimental data [58, 165]. For the problem considered in this chapter, one crucial aspect of the method is that it allows for consideration of the strength of interaction between the particles. This will be an important quantity in the analysis of the results. The robustness (and simplicity) of the measures describing the considered network will allow us to obtain both more precise and more intuitive understanding of the connection between the system-wide failure and force networks properties.

This chapter is organized as follows. We continue in Section 2.2 by discussing the methods used, providing first the basic description of the system considered in Subsection 2.2.1, and then describing briefly the discrete element techniques employed in simulations in Subsection 2.2.2, normalization and scaling in Subsection 2.2.3, followed by again brief description of the persistence homology techniques that allow for the analysis of time-dependent weighted networks in Subsection 2.2.4. Then, in Section 2.3, we discuss the main results, starting in Subsection 2.3.1 with the macro-scale results describing intruder dynamics, pullout force, as well as the force on the system boundaries. In Subsection 2.3.2, we analyze the force network, describing in detail the process of failure. Section 2.4 is devoted to the conclusions of the present study and to the discussion of possible future research directions.

2.2 Methodology

2.2.1 General Setup

The simulation geometry consists of a vertical column of diameter D_c filled with monodisperse spherical particles and a spherical intruder. The intruder is initially at contact with the center of the bottom of the column. Two column sizes are used, motivated by the ongoing experimental efforts [89]. The columns are filled with glass beads to a specified

height, H, by pouring them randomly from the top at a certain mass flow rate. The initial configuration of particles and intruder is shown in Figure 2.1. After filling to a desired

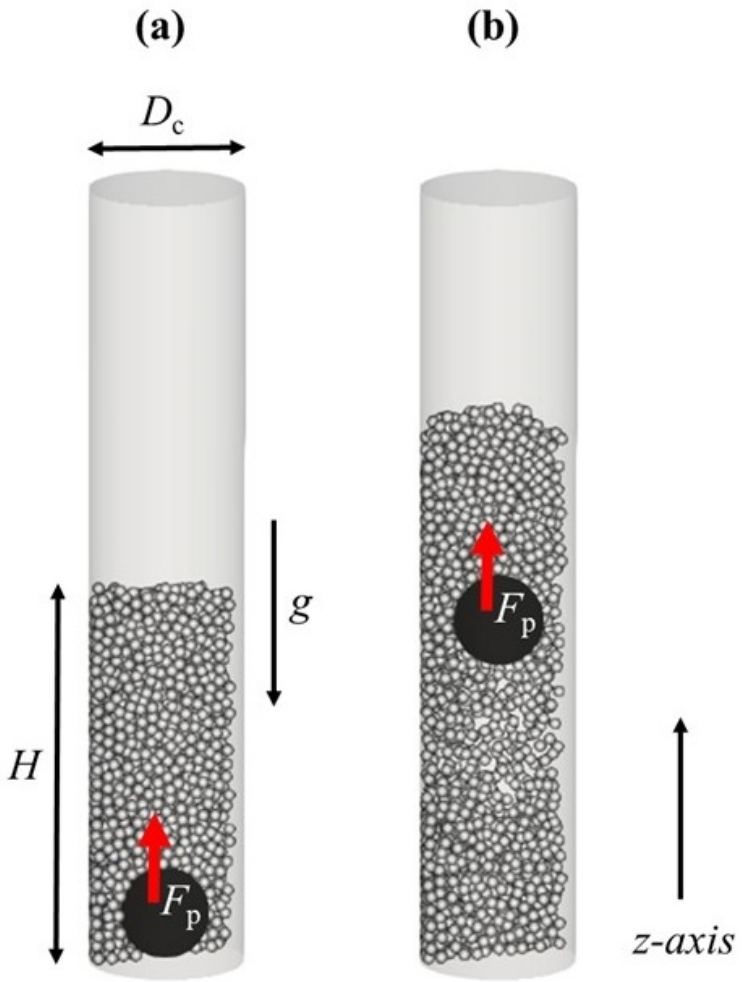

Figure 2.1 (a) Initial configuration of particles filling the column with the intruder at the bottom. (b) A snapshot showing the configuration of particles and the intruder as it travels upwards after failure. Note that the particles in the front half of the column are not shown for a clear visualization.

height, the granular material is relaxed until particles velocities are near zero. Once the particles come to a rest, the intruder is pulled vertically upward by a force, F_p, which is specified as a linear function of time with the slope of 1 N/s. At a certain force, namely the pullout force at failure $F_{pf}(H, D_c)$, the granular material fails and the intruder leaves the granular bed in fraction of a second. Figure 2.1(b) shows a snapshot of the assembly where the intruder is halfway out of the granular bed. For further illustration, Figure 2.2

shows the forces between granular particles just prior to the failure. Normal and tangential forces between the particles are displayed in this figure as a function of radial and vertical coordinates, and averaged over the angular direction. We note a significant modification of the inter-particle forces in the region just above the intruder, despite the fact that the intruder itself (and the granular particles, as we will discuss later in the manuscript) are essentially static.

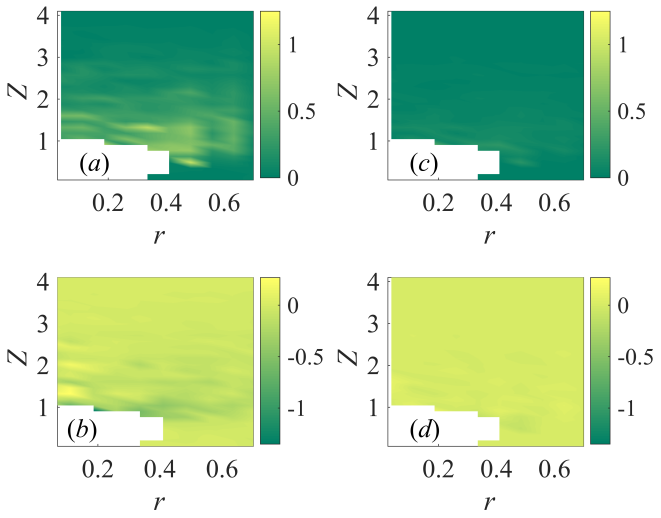

Figure 2.2 Forces between granular particles just before failure at the time when the pullout force (nondimensionalized as discussed later in the text) is $F_{\mathrm{p}} = 50$, as a function of r, z, both scaled by the intruder diameter. The intruder itself is at the bottom left corner of the figures, and the visibly step-like contour for intruder surface is the result of binning process used for the averaging of forces. The simulation parameters correspond to the reference case (circled data point in Figure 2.4) as presented later in the chapter. (a - b) Normal force between the particles in the r (a) and z (b) directions. (c - d) Tangential force between the particles in the r (c) and z (d) directions.

2.2.2 Computational Approach

DEM Solver We use the open source software, LIGGGHTS, for discrete element method (DEM) simulations of our granular system [96]. The DEM solves the equations of motion for individual particles and identifies the contacts and contact forces with neighboring particles. Applying the Newton's second law for a particle j with mass m_{j}, the moment

of inertia I_{j}, translation velocity, $\mathbf{v}_{\mathrm{j}}$, and angular velocity, ω_{j}, the equations of motion can be written as follows

$$m_{\mathrm{j}}\frac{d\mathbf{v}_{\mathrm{j}}}{dt} = \sum_{k}\left(\mathbf{F}_{\mathrm{n,jk}} + \mathbf{F}_{\mathrm{t,jk}}\right) + m_{\mathrm{j}}\mathbf{g},$$

$$I_{\mathrm{j}}\frac{d\omega_{\mathrm{j}}}{dt} = \sum_{k}\mathbf{T}_{\mathrm{jk}},$$

where $\mathbf{F}_{\mathrm{n,jk}}$ and $\mathbf{F}_{\mathrm{t,jk}}$ are the normal and tangential components of the contact forces between particles j and k. $\mathbf{T}_{\mathrm{jk}}$ is the torque imposed by the tangential component of the contact force from particle j on particle k, and $\mathbf{g}$ is the acceleration due to gravity. The normal and tangential forces contributing in building the two terms of stiffness and damping coefficients can be computed from the modified Hertz-Mindlin model as below [57, 174]

$$\mathbf{F}_{\mathrm{n,jk}} = -\frac{4}{3}\overline{Y}\sqrt{\overline{R}}\delta_{\mathrm{n}}^{\frac{3}{2}}\mathbf{n}_{\mathrm{jk}} + 2\sqrt{\frac{5}{6}}\beta\sqrt{S_{\mathrm{n}}\overline{m}}\mathbf{v}_{\mathrm{n,jk}}, \tag{2.1}$$

$$\mathbf{F}_{\mathrm{t,jk}} = -8\overline{G}\sqrt{\overline{R}\delta_{\mathrm{n}}}\mathbf{t}_{\mathrm{jk}} + 2\sqrt{\frac{5}{6}}\beta\sqrt{S_{\mathrm{t}}\overline{m}}\mathbf{v}_{\mathrm{t,jk}}, \tag{2.2}$$

where $S_{\mathrm{n}} = 2\overline{Y}\sqrt{\overline{R}\delta_{\mathrm{n}}}$ and $S_{\mathrm{t}} = 8\overline{G}\sqrt{\overline{R}\delta_{\mathrm{n}}}$. Here, δ_{n} is the normal overlap distance between the particles, $\mathbf{n}_{\mathrm{jk}}$ is the normal unit vector directed from the center of particle j to that of particle k, $\mathbf{t}_{\mathrm{jk}}$ is the tangential displacement vector calculated by integrating the relative tangential velocity at the contact over time, $\mathbf{v}_{\mathrm{n,jk}}$ and $\mathbf{v}_{\mathrm{t,jk}}$ are the normal and tangential components of the relative velocity of particles j and k. The expression for the torque is given as $\mathbf{T}_{\mathrm{jk}} = R_{\mathrm{j}}\mathbf{n}_{\mathrm{jk}} \times \mathbf{F}_{\mathrm{t,jk}}$. The magnitude of the tangential force is truncated by the Coulomb friction criterion: $\mathbf{F}_{\mathrm{t,jk}} \leq \mu\mathbf{F}_{\mathrm{n,jk}}$, where μ is the friction coefficient. In the above Equations 2.1 - 2.2, the coefficient β, expressed as a function of restitution coefficient e, is

given by $\beta = \ln e / \sqrt{\ln^2(e) + \pi^2}$. The other quantities used in Equations 2.1 - 2.2 are given as follows

$$\frac{1}{\overline{Y}} = \frac{1-\sigma_{\mathrm{j}}^2}{Y_{\mathrm{j}}} + \frac{1-\sigma_{\mathrm{k}}^2}{Y_{\mathrm{k}}},$$

$$\frac{1}{\overline{R}} = \frac{1}{R_{\mathrm{j}}} + \frac{1}{R_{\mathrm{k}}}, \quad \frac{1}{\overline{m}} = \frac{1}{m_{\mathrm{j}}} + \frac{1}{m_{\mathrm{k}}},$$

$$\frac{1}{\overline{G}} = \frac{2\left(2-\sigma_{\mathrm{j}}\right)\left(1+\sigma_{\mathrm{j}}\right)}{Y_{\mathrm{j}}} + \frac{2\left(2-\sigma_{\mathrm{k}}\right)\left(1+\sigma_{\mathrm{k}}\right)}{Y_{\mathrm{k}}},$$

where $\overline{Y}$ is the effective Young's modulus, $\overline{G}$ is the effective shear modulus, σ is the Poisson's ratio, $\overline{R}$ is the effective radius and $\overline{m}$ is the effective mass. Similar equations as the above-mentioned ones are used to compute particle-wall contact forces, in which particle k is assumed to be a particle with infinite radius and mass.

Simulation Details Table 2.1 specifies the mechanical properties of materials and simulation parameters. The mechanical properties of materials as given in Table 2.1 represent glass beads as the granular material, the sidewall of the column has properties close to PVC, and the intruder and bottom wall of the column have properties close to steel, motivated by recent experiments [89]. The Young's modulus and the Poisson's ratio were obtained from literature [85, 97, 166].

The value of the restitution coefficient between glass beads is taken as 0.9 [97]. The restitution coefficient of steel is typically in the range of about $0.6-0.9$, and a value of 0.8 is assigned here for steel and glass bead contacts. The restitution coefficient between glass beads and sidewall is assigned as 0.85. The relevance of all above-mentioned values of the coefficient of restitution is found to be insignificant in present simulations as the granular material remains essentially in static state prior to failure.

Table 2.1 Mechanical Properties of Materials and Simulation Parameters

Mechanical properties	Value	Mechanical properties	Value
Young's modulus, GPa		Friction coefficient	
intruder, bottom wall	200	intruder-glass beads, μ_{ig}	0.45
glass beads	10	glass beads-glass beads, μ_{gg}	0.4
sidewall	3	glass beads-sidewall, μ_{gw}	0.3
Poisson's ratio		Restitution coefficient	
intruder, bottom wall	0.3	intruder-glass beads	0.8
glass beads	0.2	glass beads-glass beads	0.9
sidewall	0.4	glass beads-sidewall	0.85
Simulation parameters	Value	Simulation parameters	Value
Density, kg/m^3		Diameter, m	
intruder	7728	intruder	0.0349
glass beads	2500	glass beads	0.005
Mass of intruder, kg	0.172	DEM time step, s	5×10^{-7}

2.2.3 Normalization of Relevant Quantities

To obtain a better insight into the physics of the studied system, and for simplicity, we normalize the relevant quantities using the intruder diameter, D_i and the reference force, F_0. The choice of F_0 is based on the weight of a reference volume, which is taken as a cylinder of diameter D_i and height D_i, filled with granular matter. Since the volume

fraction changes (very slightly) with filling height, H, due to gravitational compaction, we choose the average value obtained in simulations (that use different H), giving the value of $F_0 = 0.425$ N. We will see later in Subsection 2.3.1 that the force scale chosen as specified is natural for the considered problem. From this point, all the results are given using D_i and F_0 as the scales for the length and force, except if specified differently. At a couple of places we will also need a time scale, which for simplicity we take as $\sqrt{D_\mathrm{i}/g}$.

We note that the pullout force, F_p, does not include the weight of intruder. Therefore, the value of $F_\mathrm{p} = 0$ corresponds to the time at which the applied force on the intruder is exactly equal to its weight.

2.2.4 Persistent Homology

For the present purposes, persistent homology could be thought of a tool for describing a complicated weighted network (such as the one describing interaction forces between the particles) in a form of diagrams, so called persistent diagrams (PDs). These diagrams are obtained by filtration, or thresholding, the strength of the interactions between the particles. As an example, let us assume that this strength is quantified by the normal interaction force between the particles in the system. Then, the simplest persistence diagrams, which we refer to as β_0 PD for the reasons that will become clear shortly, essentially traces how 'structures' (could be thought of as 'force chains', without attempting to define them) appear as a filtration level is decreased, or disappear as two structures merge. Such a PD contains rather complete information about how connectivity between the contacts depends on their strength. Figure 2.3 shows examples of the PDs computed at a given time for the system considered in the chapter (both for β_0 discussed above, and for β_1, that describes loops or cycles, and discussed further below). Each point (generator) in this diagram has two coordinates, 'birth' - specifying when (at which filtration level) it appeared, and 'death' - specifying when it disappeared, due to merging with another structure. Note that the term 'persistence' in this context refers to the force range over which a certain structure

'persists', or survives, as a considered filtration level is changed. The interested reader could find rather detailed description on how these diagrams can be (properly) defined and computed in [105], and a simplified description including toy examples and insightful animations in [104]. For the purposes of the chapter, we list here few key features of PDs that are important for understanding their meaning, relevance, and use:

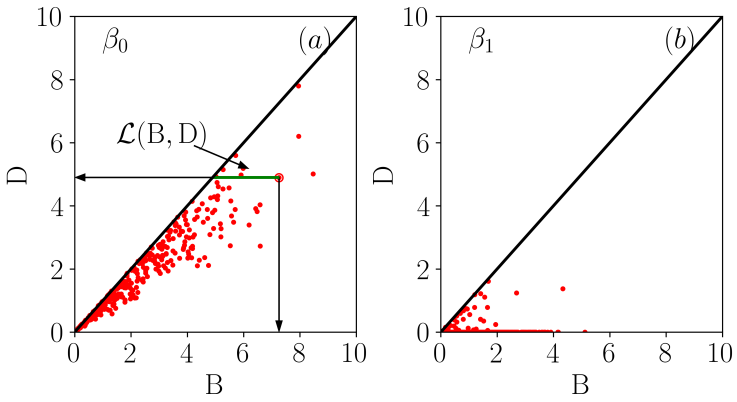

Figure 2.3 Examples of persistence diagrams, PDs, for (a) components (clusters), β_0, and (b) for loops (cycles), β_1. The axes show the force level at which a structure appears (B) and disappears (D) The lifespan $\mathscr{L}$ = B-D illustrates the force threshold range over which a structure persists. These particular PDs were obtained for the reference case discussed later in the text (circled data point in Figure 2.4), and for pulling force $F_{\mathrm{p}} = 9$ (dimensionless value, as discussed in Subsection 2.2.3).

- Persistent diagrams live in a metric space and therefore can be compared in a meaningful manner. This means that one can compare the weighted force network at different points in time, which is a crucial feature if one wants to understand an evolving system.

- Since the description of a weighted force network in terms of persistence diagrams provides a significant data reduction, there is an associated loss of information, and therefore PDs do not provide full information about the underlying network. However, the information contained in PDs still provides for all practical purposes a reasonably precise insight not only regarding the number of structures, but about how their connectivity changes as one considers different thresholding (filtering) levels.

- The number of PDs for a given weighted network is equal to the number of spatial dimensions: i.e., for a 3D system considered here, in principle there are three PDs that can be associated: β_0 PD describing clusters; β_1 PD describing loops (cycles), and β_2 PD describing three dimensional holes. In the present work, we do not find β_2's, and therefore focus on β_0 and β_1 PDs. Figure 2.3 shows that the β_0 generators appear on higher force level than β_1 ones, since β_0 structures need to merge to form loops, and this happens on lower force levels. The points at the death level $D = 0$ in Figure 2.3(b) show all the loops that formed, but never died: a loop dies at the threshold level D when it is filled up with contacts with the force of at least D, and for many loops this does not happen; see [105] for more details. On the other hand, all β_0 components disappear at nonzero D, since for low values of force all separate clusters merge.

- A PD provides information about a weighted network that is threshold independent: there is no need to specify a threshold level to describe the considered network. A PD provides information about all threshold levels at once. This is a major difference compared to other measures describing force networks, which often require separation of a force network into a 'strong' or a 'weak' network. With this being said, one can in principle consider only a subset of points in a PD, and focus on a particular range of interest. For example, for the diagram shown in Figure 2.3, one could consider only the points found for large thresholds, describing a strong part of the force network, or the points for small thresholds, describing a weak part of the network.

- The number of 'force chains' or 'clusters' of connected contacts (or the number of loops (cycles)) characterized by a force larger than a specified threshold can be easily extracted from the PDs, providing therefore information about Betti numbers, β_n, that essentially measure a number of features of a given type. Note however that the number itself does not provide any information about connectivity. Furthermore, one can show [105] that Betti numbers are susceptible to noise, meaning that a small change in the input data could lead to a large change of the Betti numbers. Finally, the β_n's are threshold dependent, and therefore provide less complete information about the underlying weighted network.

- The PDs are essentially point clouds, and an appropriate measure for their quantification needs to be developed. One possibility is based on the idea that both the number of points in a diagram, and for how long (that is, for how many thresholds levels) a point persists, are appropriate measures describing the force network between particles. Using landscape as an analogy, the number of points in β_0 PD specifies the number of (mountain) peaks, and their lifespan (see below) describes how well developed these peaks are, or, to push the landscape analogy further, how high they are compared to the 'valleys' that surround them. The concept of lifespan, $\mathscr{L}$ is illustrated in Figure 2.3, as essentially the difference between birth (B) and death, D, coordinates, so $\mathscr{L} = \mathrm{B} - \mathrm{D}$. Both measures could be combined into one by defining total persistence, TP, as a sum of all lifespans. We will be using TP in discussing some properties of the force networks in the considered system.

- The reader should note the enormity of the data reduction described so far: first a weighted force network is reduced to a point cloud (PD) and then this point cloud to a single number (TP). Such a reduction clearly leads to huge data loss, but as we will see, still provides an insightful information about the underlying weighted network.

PDs provide information about the state of the system at a given time, and do not include any information about the dynamics. As pointed out, however, PDs can be compared, and in particular the concept of *distance* between PDs is well defined [105]. The distance between two PDs could be thought as a minimum (Euclidian) distance by which the points in one diagram need to be adjusted to map them exactly to the other one; if the number of points in two PDs is different, then extra points are mapped to the diagonal. Stated formally

$$d_{W^q}(\mathsf{PD}, \mathsf{PD}') = \inf_{\gamma:\ \mathsf{PD}\to\mathsf{PD}'} \left(\sum_{p\in\mathsf{PD}} \|p - \gamma(p)\|_\infty^q \right)^{1/q}. \tag{2.3}$$

Here, d_{W^q} stands for the degree q Wasserstein distance, and PD, PD$'$ are the two considered PDs. Computing the distance is a computationally expensive process in particular for complex diagrams with many points. In the present work, we focus on $q = 2$ for simplicity, and perform calculations using the method discussed in [1, 64].

2.3 Results and Discussion

We discuss main findings in this section, focusing first in Subsection 2.3.1 on the system-scale response, including the force at the failure point, the influence of system boundaries, geometry, and material parameters. These results set a stage for Subsection 2.3.2, where more in-depth analysis of the failure process itself is discussed by considering the weighted force networks that form spontaneously between granular particles.

2.3.1 Failure: Macro-scale Picture

Failure Force We start by discussing the magnitude of the pulling force applied to the intruder that causes failure. Figure 2.4(a) shows how the pullout force at failure, F_{pf}, depends on the filling height, H, for the two granular columns; at first we focus on the ▲ symbols (connected by the solid lines) which show the results obtained using the friction parameters given in Table 2.1.

We see that F_{pf} increases with H, as expected, since larger H leads to a larger pressure on the intruder. Figure 2.4(a) (inset) also clarifies the force scaling: with the choice of F_0 specified in Subsection 2.2.3, F_{pf} extrapolates to $F_{\mathrm{pf}} \approx 1$ as $H \to 1$ (note that all quantities are dimensionless). Furthermore, we observe that F_{pf} is larger for the smaller diameter column, showing the relevance of particle-wall interactions. This finding can be understood based on an increased forces on the side walls (Janssen effect, see [126] for a recent discussion), which are considered in more detail in Subsection 2.3.1. Note that the effect of the sidewall on F_{pf} diminishes as H decreases, since for small H we enter the hydrostatic regime where the column size is not relevant. Figure 2.4(b), which also plots the results obtained using smaller particles (diameter 3 mm, in contrast to 5 mm particles used in Figure 2.4(a) while keeping D_{c} the same) leads to a consistent conclusion: influence of the sidewall decreases as the number of particles increases, since for smaller particle sizes there are more particles between the intruder and the sidewall.

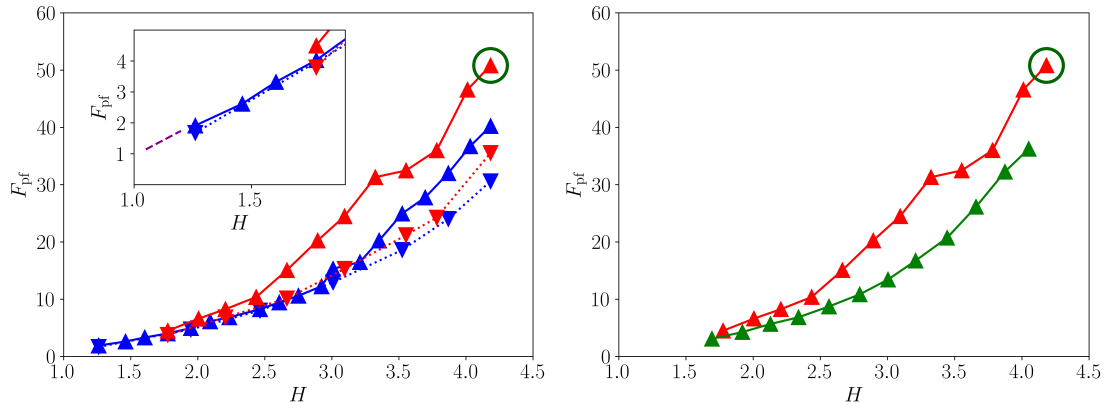

Figure 2.4 (a) The pullout force at failure, F_{pf}, for different filling heights, H, and for two different column diameters, (red), $D_c = 1.49$, and (blue) $D_c = 1.75$. ▲ and ▼ corresponding to the higher (given in Table 2.1) and lower (discussed in the text) values of the friction coefficients, respectively. The circled data point shows the reference case that is analyzed in detail later in the chapter. The inset expands the region for small H, showing that $F_{pf} \to 1$ as $H \to 1$ ((purple) dashed line). (b) The pullout force at failure, F_{pf}, as the size of particles is modified, and the tube diameter is kept fixed at $D_c = 1.49$: (red) 5 mm particles (the same data as shown in (a), and (green) 3 mm particles. Note that all quantities in this and the following figures are dimensionless.

One important question involves the influence of friction coefficient on the pullout failure force. In the present DEM simulations, there are three relevant friction coefficients: intruder - glass beads, μ_{ig}, glass beads - sidewall, μ_{gw}, and glass beads - glass beads, μ_{gg}. Figure 2.4 shows the influence of friction: ▲ were obtained using the values of friction coefficients given in Table 2.1, and the values shown by ▼ were obtained for lower values of friction coefficients ($\mu_{ig} = 0.4$, $\mu_{gg} = 0.35$, and $\mu_{gw} = 0.25$). One could wonder which of the three friction coefficients is the most/least relevant; to answer this question, we discuss the reference case (circled data point in Figure 2.4) in more detail. The F_{pf} for the reference case is 50.8. When only μ_{ig} is reduced, we find $F_{pf} = 50.1$; when μ_{gg} is reduced, $F_{pf} = 46.6$, and when μ_{gw} is reduced, $F_{pf} = 43.8$. Thus, the effect caused by the change in particle-wall friction coefficient is the most dominant, although all friction coefficients influence F_{pf}. We note that these variations are considerably larger than the ones found between different realizations of nominally the same simulation, when initial particle configurations were modified. This variability is less than 1%.

The relevance of particle-wall friction discussed above also suggests a possible explanation for a slightly weaker influence of friction for a larger column diameter, D_c. Furthermore, the influence of friction disappears for small values of H. This finding shows that in the hydrostatic regime frictional effects do not influence the failure process; it should be noted however that frictional effects may be important once the system fails and the intruder starts to move, as discussed for the case of a rod pulled out of granular matter [66].

Parameter Study Here we compare the results obtained using the smaller column diameter, and varying the height of the granular material, H. Figure 2.5(a) shows the (vertical) z-component of the force exerted by particles on the sidewall, F_w, versus the pullout force, F_p, as H is varied. The reported values of F_w are obtained by averaging the instantaneous values over a short time window (of duration $t \approx 0.13$).

We focus at first on the results obtained for large filling heights in Figure 2.5(a). Clearly F_w grows with F_p, showing that the pullout force is transferred via particles to the sidewall. This growth is non-trivial however: as F_p increases, the difference $F_p - F_w$, shown in the inset of Figure 2.5(a), reaches a plateau whose height depends on H. Therefore, for small F_p, the coupling of F_p and F_w is not complete, with F_p increasing faster than F_w. However, for larger values of F_p, the coupling becomes stronger, with essentially all the applied force transferred to the sidewall. The fact that the height of the plateau is H-dependent suggests that the forces between the particles (that may depend on both H and F_p) play a role. We defer further discussion of this effect until considering these forces in Subsection 2.3.2.

For small filling heights ($H = 1.78$ and $H = 2.21$ in Figure 2.5(a)) the results are less clear, with non-monotonous growth of F_p and $F_p - F_w$ as H is increased; possibly in this regime inverse Janssen effect discussed recently [126] becomes relevant. We leave detailed discussion of this regime for future work.

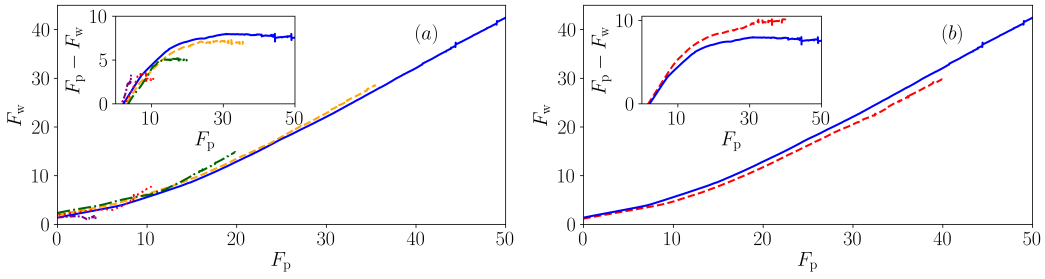

Figure 2.5 The sidewall force, F_w in the (vertical) z direction exerted by the particles. (a) $D_c = 1.49$ with variation of the filling height: $H = 4.18$ (solid blue line), $H = 3.78$ (dashed orange line), $H = 2.89$ (dash-dot green line), $H = 2.21$ (dotted red line), and $H = 1.78$ (loosely dashed purple line). (b) $H = 4.18$ with variation of the column diameter: $D_c = 1.49$ (solid blue line) and $D_c = 1.75$ (dashed red line).

Next, we focus on comparing the results of simulations carried out using different column diameters, D_c, with the height, H, kept fixed. Figure 2.5(b) shows the results: we observe F_w depends on D_c, with the larger magnitude of F_w at the failure for smaller D_c. The inset in Figure 2.5(b), which plots the difference $F_p - F_w$, shows that the height of the plateau at which this difference saturates increases as D_c increases, and the plateau itself becomes less clearly defined. This again shows that for larger column diameters, the wall forces become less important in helping the granular material to avoid failure. This motivates us to analyse further the response of the force networks prior to the failure. This is discussed in the next section.

2.3.2 Road to Failure

In this section, we discuss the failure process itself, focusing on a single choice of parameters, represented by the reference case (circled data point in Figure 2.4). To analyze the failure, we use the measures that are appropriate for discussion of the static and dynamic properties of the system, starting from the classical ones, such as forces, energies, and particle contacts, and then focusing on the force networks between the particles and the particles and the intruder.

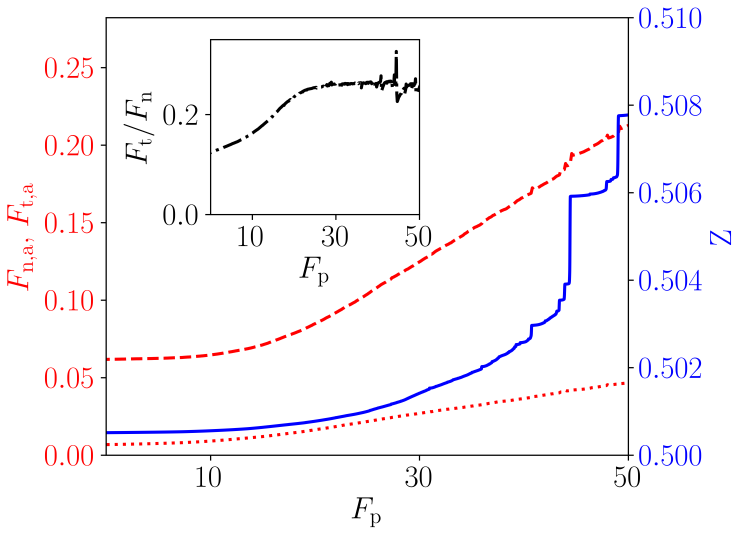

Figure 2.6 Average normal (dashed red line) and tangential (dotted red line) forces, $F_{n,a}$, $F_{t,a}$, respectively, between the granular particles, and the particles and the intruder (left vertical axis); z-position (solid blue line) of the intruder (right vertical axis); Inset: average ratio of F_t/F_n.

Forces, Energies, Contacts Figure 2.6 shows the normal and tangential average forces, $F_{n,a}$, $F_{t,a}$, respectively, between the particles (and the particles and the intruder), as well as the intruder's z-position. We focus on the time period for which the pulling force is positive (after subtracting scaled intruder's weight). Figure 2.6 shows that the dynamics of the intruder is minimal before the granular system fails: note that the whole range on the vertical z axis is just 1% of the intruder's diameter. While for smaller values of F_p, $F_{n,a}$ does not change much, for larger F_p's, $F_{n,a}$ grows approximately linearly with F_p. Since the change of $F_{n,a}$ is considerable, in what follows we will use this time-dependent value of $F_{n,a}$ for normalization of the results discussing properties of the force network.

The tangential force, $F_{t,a}$, also shown in Figure 2.6, provides relevant additional information. While $F_{t,a}$ is smaller than $F_{n,a}$ (being limited by the Coulomb threshold), the ratio $F_{t,a}/F_{n,a}$ grows as failure is approached. This result provides an initial insight regarding failure: the particle contacts get increasingly loaded by the tangential force, and approach sliding. Significant amount of sliding contacts appears as a precursor to failure. The sliding effect is also confirmed by the inset which shows the average of F_t/F_n value

at each contact (note that this quantity is not necessarily the same as $F_{\mathrm{t,a}}/F_{\mathrm{n,a}}$). We also comment on the similarities of the insets of Figures 2.6 and 2.5, with both showing similar qualitative behavior: this is not surprising since the tangential inter-particle force clearly plays a role in determining F_{w}. For larger filling height, H, the normal forces between the granular particles will be larger due to gravitational effects and therefore the allowed range for tangential forces would be larger as well, leading to stronger wall force, consistently with the results shown in the inset of Figure 2.5(a).

Continuing the discussion of sliding contacts, Figure 2.7 plots three quantities of interest: N_{s}, the ratio of the number of contacts that have reached Coulomb threshold (sliding contacts) and the total number of contacts; N_{b}, the ratio of the number of broken contacts and the total number of contacts, and the ratio of kinetic and potential energies of the granular particles, $E_{\mathrm{k}}/E_{\mathrm{p}}$ (here E_{k} includes only translation degrees of freedom, and E_{p} is measured relative to the bottom of the column). All quantities are calculated over the time intervals of duration $\Delta t \approx 0.84$. While the results are rather noisy, we can still reach some relevant conclusions, which could be also verified by inspecting the inset of Figure 2.7, which shows an expanded view of the energy ratio and N_{s}. First of all, very small values of $E_{\mathrm{k}}/E_{\mathrm{p}}$ suggest minimal rearrangements of the particles during the period before failure, consistently with small N_{b} (note that the latter quantity is barely visible in Figure 2.7, showing that only small fraction of contacts breaks before failure). While detailed inspection of the data does not show any correlation between N_{b} and $E_{\mathrm{k}}/E_{\mathrm{p}}$, the same conclusion does not apply to N_{s}, for which we find significant (anti)correlation with $E_{\mathrm{k}}/E_{\mathrm{p}}$. This result shows that, while reaching Coulomb threshold may not lead to breaking of a contact, it may lead to sliding, which reflects itself in an increase of kinetic energy. We note that E_p itself is essentially constant before failure.

The results presented so far provide a basic idea about the processes leading to failure: the tangential force increases at particle-particle and particle-intruder contacts faster than the normal force; the number of sliding contacts increases as well, until at

failure point the Coulomb threshold is overcome and the intruder starts to move. Until failure occurs, the intruder is essentially static, with the change of position measured as a small fractions of the intruder diameter. Additional insight can be reached by considering spatial and temporal properties of the force network, as discussed next.

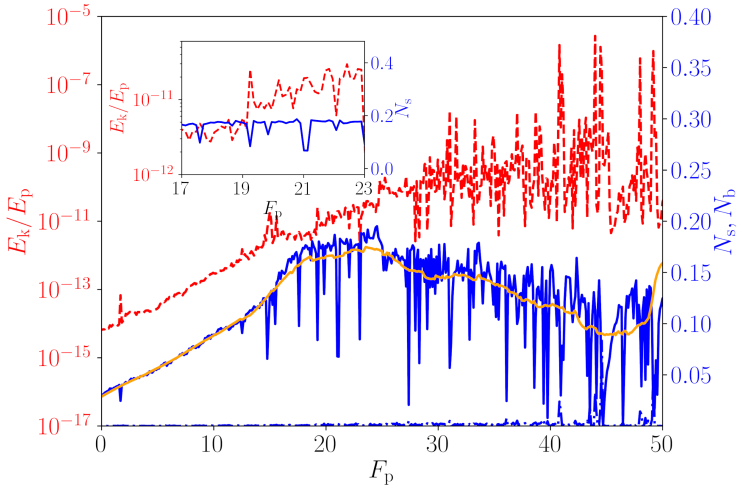

Figure 2.7 (left) E_k/E_p (dashed red line): the ratio of kinetic and potential energies of the particles; (right) N_s (solid blue line): the ratio of the number of contacts reaching Coulomb threshold and the total number of contacts, the orange solid line shows the running average of N_s; N_b (dash-doted blue line): the ratio of the number of broken contacts and the total number of contacts. Inset: expanded view showing E_k/E_p and N_s illustrating frequent anti-correlation.

Force Network and Failure The tools of persistent homology, discussed briefly in Subsection 2.2.4, provide an extensive information about the force networks. We start by discussing rather straightforward measures focusing on the structures (clusters or loops) introduced in Subsection 2.2.4. For brevity, we focus in this section on discussing the measures computed using the normal force, F_n, only; the findings obtained by considering the tangential forces are found to provide consistent information with the one reported here.

Figure 2.8 shows the results for the β_0 (a, c), and β_1 (b, d), both for the size, S_c (a, b) and the (Betti) numbers (c, d) of the structures. These quantities can be easily extracted from the corresponding persistence diagrams: Betti numbers, β_0, β_1 could be

found by subtracting the number of components that die from the number of components that are born above specified threshold, and S_c is simply the number of contacts (with force above chosen threshold) divided by β_0 or β_1. Consistently with the results discussed in Subsection 2.3.2, Figure 2.8 shows that the force network evolves even while the intruder is almost stationary, and the contact network is essentially unperturbed. This evolution is particularly obvious when considering β_1 structures for the large thresholds values: the (average) size of β_1 structures increases significantly as F_p increases, see Figure 2.8(b), while the corresponding β_1 decreases, Figure 2.8(d), albeit not so fast (note the log scale on the vertical axes). Basically, what happens here is that the loops become smaller and their number grows as the pullout force increases. The conjecture is that the loops play an important role in stabilizing the system exposed to external forcing, consistently with the findings reached by considering impact experiments [165], where loops were found to play a significant role in slowing down an intruder entering the domain filled with particles. The changes in the size and number of β_0 structures are much more gradual, but consistent, showing (again for the large thresholds) a slow increase in the size and slow decrease in the number - essentially, the clusters merge together and encompass more and more contacts as the pullout force increases. Regarding the threshold dependence, we note that the number of β_0 structures is an increasing function of chosen threshold for the range chosen: here we are considering the range of thresholds at which we still have many contacts (viz. the PD diagrams shown in Figure 2.3; for even larger thresholds, β_0 would decrease similarly as observed in a recent study of suspensions [67]. We also note that the sizes, S_c, of β_0 and β_1 structures are comparable at large thresholds, as expected. We remind the reader that the force thresholds used in this figure are normalized by the current value of the average (normal) contact force plotted in Figure 2.6.

The concept of clusters and loops is useful since these quantities provide an initial insight, and also since they can be related to the commonly considered 'force chains' and 'cycles'. However, this concept suffers from a significant deficiency, and that is

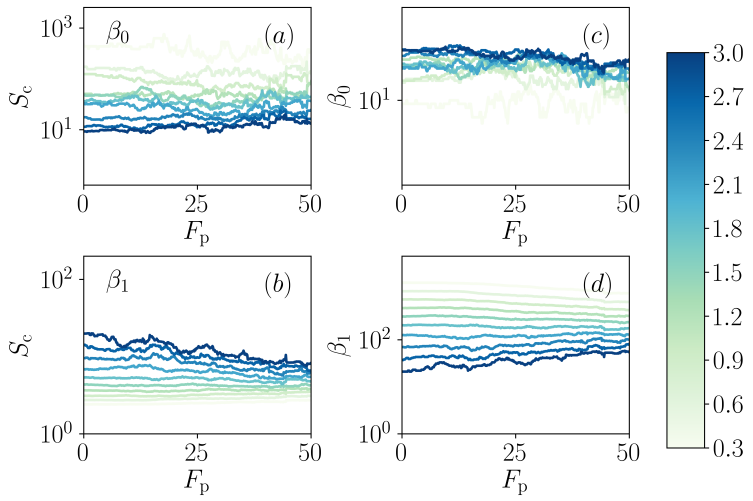

Figure 2.8 (a, c) β_0 component ('force chains') size (a) and number (c); (b, d) β_1 component (loops, 'cycles') size (b) and number (d) for different force threshold values (shown by the color bar). Note the opposing trend of β_0 and β_1; e. g., Betti numbers for the clusters (β_0) increase for the considered thresholds since for small threshold values all clusters are connected; the loops (β_1) (d) are more numerous for small threshold values due to merging of the clusters. Note the use of log scale on the vertical axes.

the threshold dependence. This deficiency is removed by the total persistence, which essentially merges the complete information (for all thresholds) into a single number, as discussed in Subsection 2.2.4. Figure 2.9 shows the total persistence, TP for β_0 (and for β_1 in the inset) structures. The TP for β_0 structures (clusters) increases continuously with the pullout force, showing again that restructuring of the force network takes place (even when rescaling by the average time-dependent normal force). We could now ask whether TP increases across the whole range of the interaction forces, or whether the increase is concentrated in a particular range. Figure 2.9 shows that the latter is correct: the values of TP for the β_0 structures characterized by the force significantly larger than the average force, $F_{n,a}$, increase strongly, while the TP for the structures born at the medium or weak level remain essentially the same. The inset of Figure 2.9 shows that the trend for β_1 structures (loops) is different, since TP decreases as F_p increases; we discuss this behavior further below.

One could ask what is the nature of the changes in the force networks that leads to such a strong increase of TP for the β_0 structures born at a large force level: to use a landscape analogy, one could ask whether the hills become higher, or there are more hills as F_p increases (recall that TP essentially combines the information about lifespans, $\mathscr{L}$, of the generators in PD's, and the number of generators). To answer this question, Figure 2.10 shows the number of generators. Most interestingly, we observe that the number of β_0 generators is essentially constant, saying that the reason for the increase of TP for strong forces is an increased range of the interaction forces: the strong generators are born at even higher force levels. Regarding the loops, Figure 2.10(b, d, f) show an increase of the number of loops in the strong region, on the expense of the medium ones, consistently with the results for TP in Figure 2.9 (inset); however overall number of generators decreases, leading do a decrease of total TP.

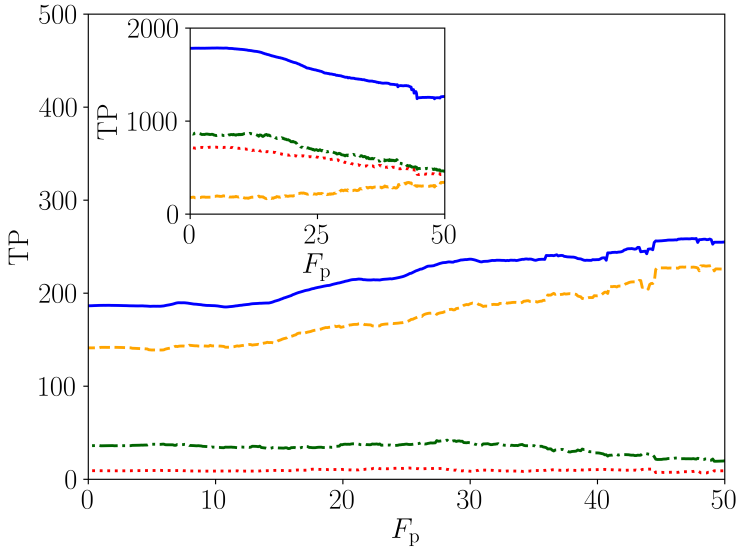

Figure 2.9 Total persistence, TP for β_0 structures (clusters) (main figure) and for β_1 structures (loops) (inset). The total value (solid blue line) of TP is shown, as well as the values of TP for the birth coordinate in strong range (dashed orange line) (> 2.5), medium range (dash-dotted green line) $[1.0 - 2.5]$ and weak range (dotted red line) $[0.0 - 1.0]$.

Another question to ask is to which degree TP captures spatial dependence of the particle interactions, illustrated for $F_\mathrm{p} = 50$ (so just before failure) in Figure 2.2. To answer

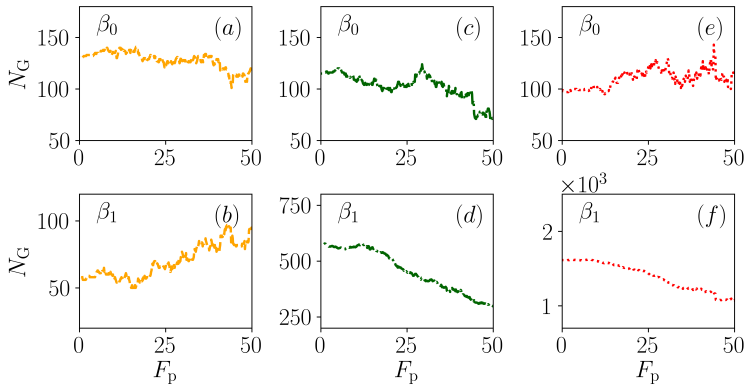

Figure 2.10 Number of generators (points in the PD's) using the same line and color convention as in Figure 2.9: strong (a, b), medium (c, d), and weak (e, f).

this question, we compute TP separately for five different parts of the system, according to the distance from $z = 0$ (bottom of the column). Figure 2.11(a) shows the results; for simplicity, here we consider TP β_0 only, and also normalize TP by the number of particles, N_p, in each of the separate regions the size of the regions was chosen so that N_p does not change much between the regions. We see that the changes of TP are concentrated in the parts of the system that are close to the intruder, with the most pronounced changes in the layer just above the intruder itself, consistently with the snapshot shown in Figure 2.2.

So far, we have focused on the analysis of system properties at a specified time instant, without attempting to discuss temporal evolution of the force network. However, temporal evolution is very much of interest as well, since time dependency of force networks is far from simple. To gain at least basic insight into this evolution, we use the concept of distance between PDs, discussed in Subsection 2.2.4, see Equation 2.3, normalized by the number of particles in each region, N_p. Figure 2.11(b) shows the results, again for the five regions mentioned above. For simplicity, we consider only d_{W^2} distance. Figure 2.11(b) shows the localized (both in space and time) changes of the distance, which are particularly prominent in the region close to the intruder itself. The inset of Figure 2.11(b) shows expanded view, illustrating sudden changes of the considered distance measure. These results show clearly that the force network starts evolving while

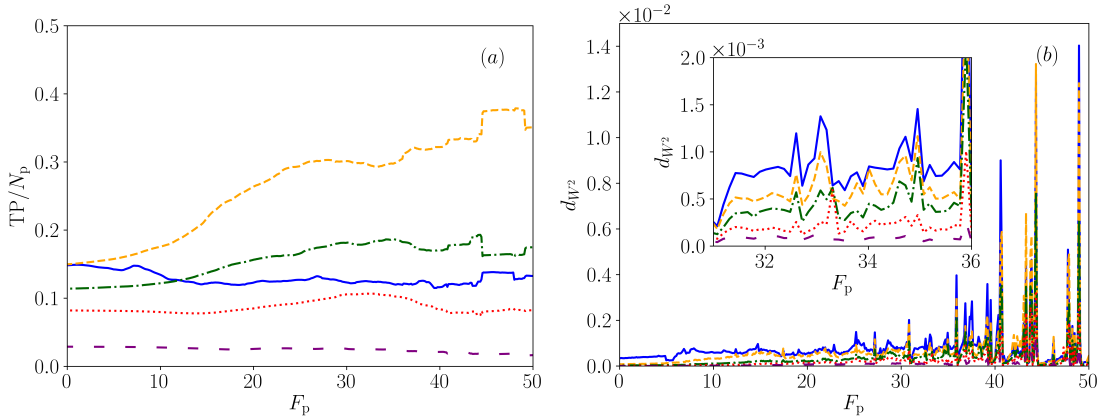

Figure 2.11 (a) Total persistence, TP for β_0 structures (clusters), computed separately for the five parts of the system, for $0 < z < 1$ (solid blue line), $1 < z < 1.72$ (dashed orange line), $1.72 < z < 2.44$ (dash-dotted green line), $2.44 < z < 3.16$ (dotted red line), and $3.16 < z < 4.18$ (loosely dashed purple line). (b) Distance d_{W^2} for β_0 structures for the same five regions as in (a), using the same convention for lines patterns and colors. The inset expands a part of the considered range of the pulling force, F_p.

the particles (and the contact network) are essentially static, and that the changes of the force network are not continuous, but consist of short bursts of activity, which become more prominent as the system approaches failure.

As mentioned at the beginning of Subsection 2.3.2, we focus on the normal forces only in this section. While we found that the tangential forces provided relevant information about the mechanism of failure as well, the measures obtained by computing persistence and derived quantities turn out to be qualitatively similar to the ones obtained based on the normal forces only, so for brevity we do not discuss them further.

2.4 Conclusions

DEM simulations of the pullout of an intruder buried in confined granular media show that the force required to fail the material varies both with the height of the granular material and with the column diameter. Frictional effects are found to be important for large material heights only, showing that in hydrostatic regime (for small filling heights), the frictional effects are not relevant. While for smaller pullout forces the force exerted by the granular

particles on the sidewall remains small, for larger pullout forces, these two forces change at the same pace, illustrating the role that the sidewalls and particle-wall interactions play in the failure process.

Analysis of the interparticle forces, using both classical and novel methods based on persistent homology, uncovers the details of the failure process. While the intruder and the granular particles are essentially static before failure, and characterized by a (static) contact network, the (weighted) force network that includes the information about the particle contacts goes through significant changes. The tangential forces between the particles increase as the applied force becomes larger, leading to a larger number of sliding contacts. The normal force between the particles evolves as well, and the force network based on the normal force becomes more structured, involving larger number of loops and stronger forces between the particles, even when normalized by the mean. The failure itself occurs through a culmination of temporally intermittent changes that take place predominantly in the physical proximity to the intruder. Furthermore, the changes in the force network are focused in particular on the strong forces when considering clusters of contacts, while the loops that form in a network are evolving at all considered levels of the interaction strength. We find that careful analysis of the evolving loops provides particularly useful insight into the failure process.

By combining classical and newly developed approaches for describing both statics and dynamics of a granular system, we have discussed in this chapter precise and objective measures that can be used to describe a failure process in the considered system. It remains to be seen to which degree the presented findings apply to other systems close to failure. We hope that both the methods and the results presented in this chapter will provide guidance for future research in this direction.

CHAPTER 3

CORRELATING THE FORCE NETWORK EVOLUTION AND DYNAMICS

3.1 Introduction

A wide range of systems exhibit intermittent dynamics as they are slowly loaded, with different dynamical regimes governing many industrial and natural phenomena. In these systems, the energy is loaded gradually with a stable configuration and then is dissipated in fast dynamics with microscopic and macroscopic rearrangements [155]. Examples are fracture [18, 19], magnetization [175], and seismic activities [18, 53] such as earthquakes, in which the slowly loaded energy relaxes via fast reconfiguration. This intermittent behavior has been observed in a number of granular experiments and simulations [4, 56, 118, 134]. In analyzing such behavior, a significant progress has been reached by studying the dynamics of a slider coupled with the boundary of a granular system. A slider can exhibit a wide variety of dynamics, including continuous flows and periodic or intermittent stick-slip behavior [2, 4, 43, 144].

While a significant amount of research on exploring intermittent dynamics of granular systems has been carried out, not much is known about the connection between particle-scale response and the global dynamics, in particular for experimental systems. In slider experiments [2, 4], see also Figure 3.1, it is possible to measure particle scale response by using photoelastic techniques. These techniques allow for extracting dynamic information about evolving particle interactions which typically involve meso-scale force networks (so-called 'force chains'). Analysis of such time-dependent weighted networks is not a simple task, and it has evolved through last decades in a variety of different directions, including force network ensemble [153, 170], statistics-based methods [33, 143], and network type of analysis [21, 182]. In this research, we will consider application of persistent homology (PH), which allows for formulating precise and objective measures

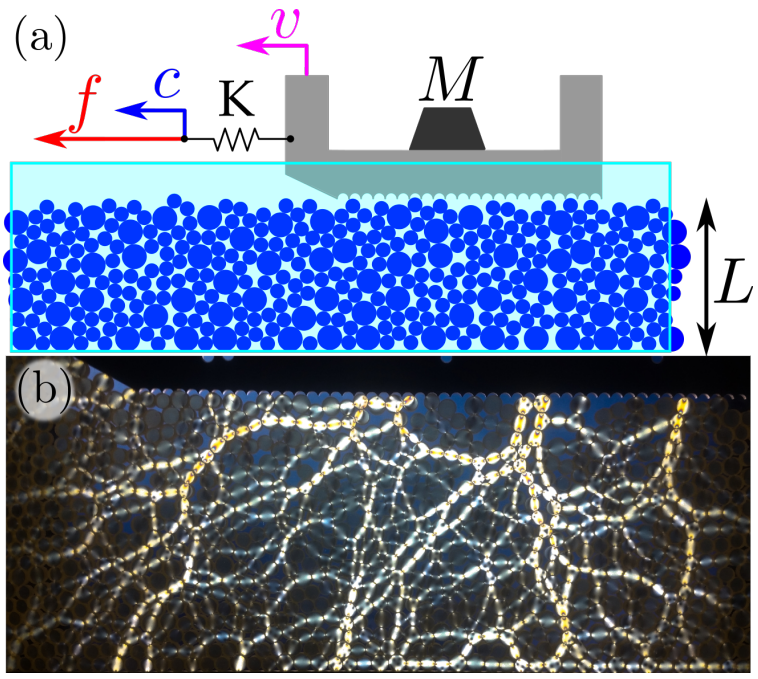

Figure 3.1 (a) Sketch of the experiment. A slider sits on top of a 2D granular system with photoelastic disks, and is connected to a stage by a spring of constant k, pulled by a constant speed c. A force gouge measures the force f; the granular medium is imaged with fast cameras. (b) Photoelastic response during loading [2].
Source: [2]. Reprinted with permission

of static and dynamic properties of the force networks. This approach has been used extensively in analysis of the data obtained via discrete element simulations in the context of dry granular matter [10, 105] and suspensions [67], but its application to experimental data has so far been rather sparse [58, 165]. We show that this method allows to develop clear correlations between the static and dynamic properties of the force networks on micro- and meso-scale and the macro-scale system dynamics.

3.2 Techniques

3.2.1 Experimental Techniques

In our experiments, as shown in Figure 3.1(a), a stage pulls a 2D frictional slider with toothed bottom, of a fixed length of 25 cm and a mass of $M = 85$ g. The stage, which moves at constant speed c, is connected to the slider by a linear spring of stiffness K. The

slider rests on a vertical bed of fixed depth $L = 9.5$ cm and length 1.5 m, consisting of bi-disperse photo-elastic disks with radii of 0.4 cm and 0.5 cm. A camera, recording the photo-elastic response of the medium at 120 fps, is connected to the stage. We also record the force f experienced by the spring.

We consider three experiments characterized by different configurations of c and K: Experiment 1: $K = 14$ N/m, $c = 0.5$ mm/s; Experiment 2: $K = 70$ N/m, $c = 0.5$ mm/s, and Experiment 3: $K = 70$ N/m, $c = 1.0$ mm/s. The total number of analyzed frames (images) is 30,000 for each experiment, corresponding to 250 seconds of physical time.

3.2.2 Image Processing

The goal of the image processing in this study is to reveal clear force signal and reduce noise effects as much as possible. As the fast imaging in our experiments constrains the resolution of images, we use brightness method to capture force information, which works better that G^2 method for the type of data collected, see [3]; similar approach was used in [165]. We first remove background noise from the original images by applying a filter that removes pixels of brightness below chosen threshold value so to remove low light area and particle textures. Multiple threshold values were investigated, giving no quantitatively difference in the results of the topological analysis that follow; we typically use threshold value of 90 (the maximum brightness is 255), which is appropriate for capturing the relevant information. After thresholding, the image brightness is linearly mapped to 0-255 range. MATLAB built-in functions *imerode* and *imdilate* were applied to slightly dilate the bright regions so to fill the gaps between neighboring particles where in force chains are connected, and then to erode away the unwanted excessive dilation to restore the force networks with more accuracy. Figure 3.2 shows an example of image processing; in our computations discussed in what follows, we use grey scale version of the figures such as Figure 3.2 for the purpose of computing considered topological measures.

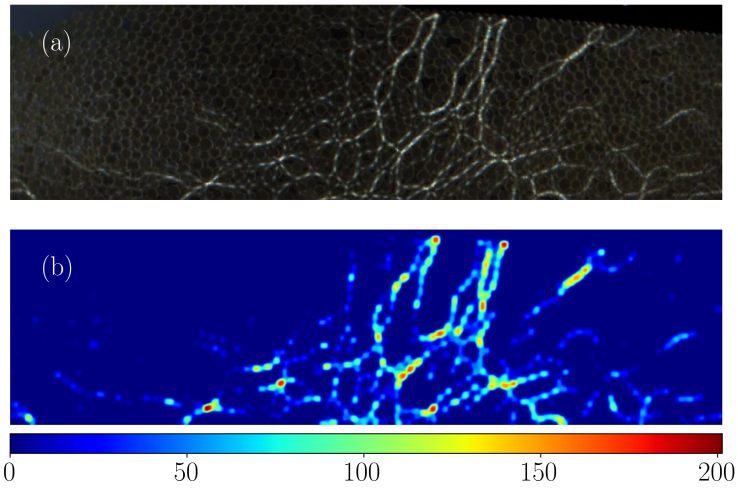

Figure 3.2 An example of image processing. (a) An original experimental image. (b) A processed image; color scheme shows pixel intensity.

3.2.3 Topological Measures

Persistence homology (PH) allows for formulating objective measures describing force networks in both simulations and experiments. Analysis of experimental data, such as the ones considered here, presents some challenges which are discussed in some detail in [105].

Each experimental image can be considered as an array of pixel brightness $\theta \in [0,255]$. Since the pixels of high brightness correspond to the particles experiencing large forces, we can apply PH to the pixels to track and quantify their connectivity to extract (approximate) information about the actual force networks. PH techniques essentially encode the appearance (birth) and disappearance (death) of force networks by generating persistence diagrams (PDs) that encode the birth and death brightness levels for components (loosely speaking, force chains), and loops (cycles). The PDs therefore reduce the complexity of underlying force networks into point clouds where the coordinates are $(\theta_{\text{birth}}, \theta_{\text{death}})$ and each point represents an object that could be either connected component (chain) or a loop (cycle). The lifespan of an object is defined as $\theta_{birth} - \theta_{death}$, measuring how long the object lasts as the threshold is varied. Total persistence (TP) of a PD is defined as the sum of all lifespan of the points, $\text{TP}(\text{PD}) = \sum_{(\theta_{\text{birth}},\theta_{\text{death}})\in \text{PD}} (\theta_{\text{birth}} - \theta_{\text{death}})$,

which further reduce the complexity of force networks to a single number [101]. Note that TP is influenced by both how many components there are, and by their lifespans.

Another quantity related to PDs is the distance (or difference) between them. The distance measures essentially the cost of mapping points in one PD to those in another PD; in the case of different number of points, the extra ones are mapped to the diagonal. In particular, the *degree-q Wasserstein distance* between two persistence diagrams PD and PD' is defined as

$$d_{Wq}(\mathsf{PD},\mathsf{PD}') = \inf_{\gamma:\mathsf{PD}\to\mathsf{PD}'} \left(\sum_{p\in\mathsf{PD}} \|p-\gamma(p)\|_\infty^q \right)^{1/q},$$

where γ is a bijection between points from PD to PD', $\gamma : \mathsf{PD} \to \mathsf{PD}'$. In the present work we use $q = 2$ and carry out the calculations using the method discussed in [64, 48].

3.3 Results

3.3.1 Structural Response

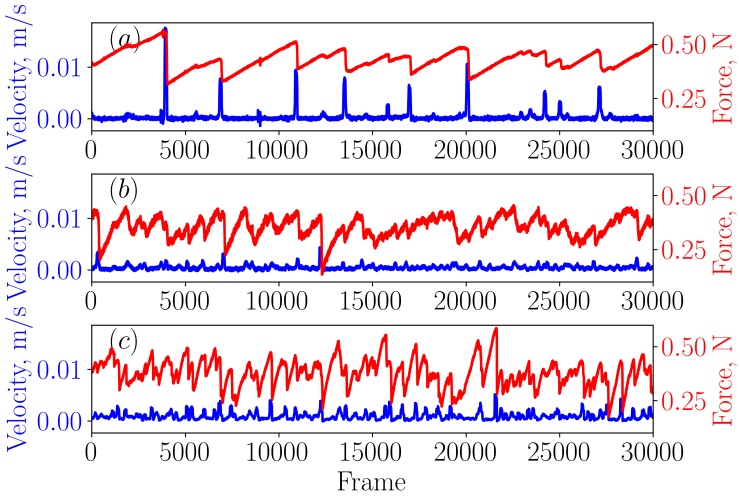

Figure 3.3 Sliders' velocity and spring force for the considered experiments: (a) Experiment 1, (b) Experiment 2, (c) Experiment 3.

Figure 3.3 shows the calculated velocity of the slider and the measured force, f, on the spring. This figure illustrates clearly the slider's dynamics. We note that Experiment 1

exhibits crackling stick-slip behavior as the driving rate is small. During a stick, the spring builds up the stress, while the slider is almost fixed, until the spring eventually yields, leading to a sharp velocity jump and drop of the force. The system behaves more similarly to a continuous flow for Experiments 2 and 3, as also discussed in [2].

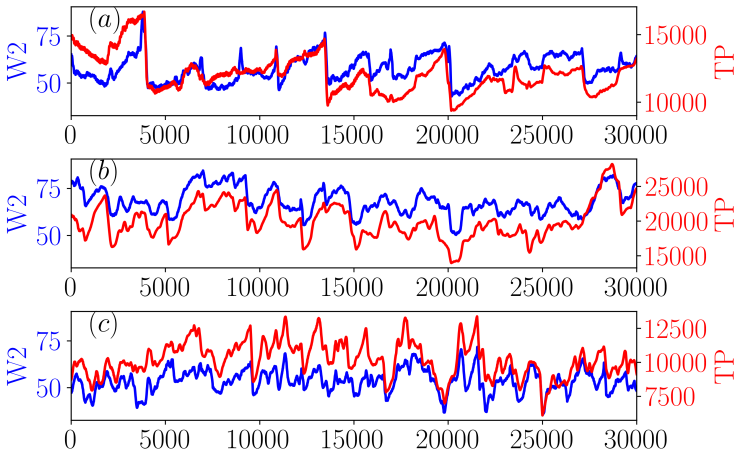

Figure 3.4 $W2$ distance and total persistence, corresponding to the experiments shown in Figure 3.3.

Next, we proceed with considering persistence measures. Figure 3.4 shows the Wassertein $q = 2$ distance (W2) for the considered experiments, as well as the total persistence (TP), for the same time interval as shown in Figure 3.3. Direct comparison with Figure 3.3 shows good agreement between the force network measures, W2 and TP, from the one side, and the sliders' velocity and the spring force, on the other. Figure 3.5 illustrates in more detail the degree of agreement between the force and W2 for Experiment 1. We note that this experiments shows particularly good agreement, suggesting stronger correlation between the force on the slider and force network properties for well defined stick-slip dynamics. We note good agreement between W2 and TP, suggesting the existence of a correlation between the 'strength' of the network measured by TP, and its temporal evolution, measured by W2.

Having established correspondence between the slider dynamics and the force network, we proceed to discuss whether such correlation could be explored for predictive

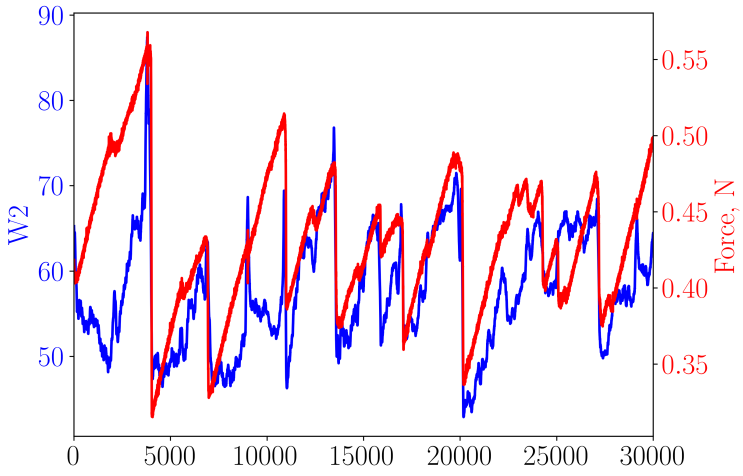

Figure 3.5 Force on the slider and W2 distance (data from Figures 3.3(a) and 3.4(a)).

purposes. To explore this question, we consider the cross-correlation between considered quantities. More precisely, consider two time series x_t, y_t, with the data $(x_1, x_2, \cdots, x_m)$, and $(y_1, y_2, \cdots, y_m)$. The cross-covariance is defined by

$$c_{xy}(k) = \frac{1}{m}\sum_{t=1}^{m}(x_t - \bar{x})(y_{t-k} - \bar{y}) \tag{3.1}$$

where $\bar{x} = \sum_{i=1}^{m} x_i/m$, $\bar{y} = \sum_{i=1}^{m} y_i/m$, and $k = 0, \pm 1, \pm 2, \cdots$ is the chosen lag. When m is outside the range of y, $y_m = 0$. Note that for the positive lag k, x_t is correlating with y_{t-k} (at earlier time), which means that we may be able to use such correlation to predict the future x from earlier y. Finally, we define the sample standard deviations of the series as

- $s_x = \sqrt{c_{xx}(0)}$, where $c_{xx}(0) = Var(x)$.
- $s_y = \sqrt{c_{yy}(0)}$, where $c_{yy}(0) = Var(y)$.

The cross-correlation coefficient is given by

$$r_{xy}(k) = \frac{c_{xy}(k)}{s_x s_y}, k = 0, \pm 1, \pm 2, \cdots \tag{3.2}$$

Figure 3.6 shows the cross-correlation coefficients for Experiment 1, where r_{f*}, r_{v*} correspond to the cross-correlation coefficient between the f or v and the measure of

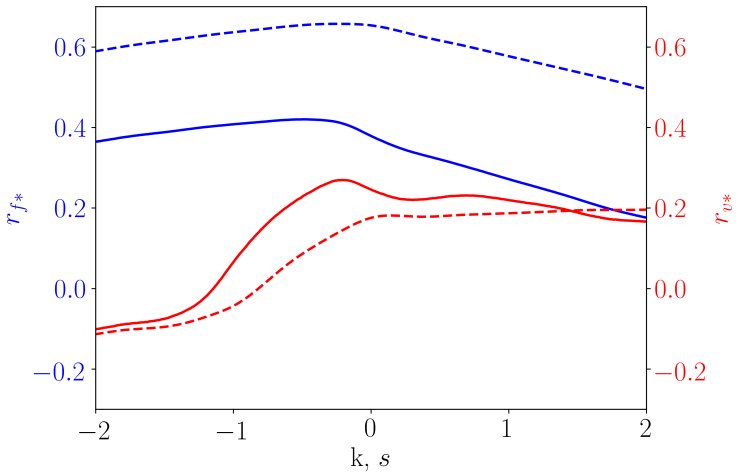

Figure 3.6 Cross correlation coefficient as a function of lag k (in seconds). r_{f*} and r_{v*} for Experiment 1, where $*$ stands either for W2 distance (solid line), or for TP (dashed line).

interest *, which can be w for W2 distance or t for TP. Focusing first at the results without lag, $k = 0$, we note that the r_{f*} correlations are higher than the r_{v*} ones; we expect that this is due to the fact that the velocity data were obtained by taking a discrete derivative of the slider position data, introducing further noise which may blur the actual signal. The r_{f*} results show that the correlation is higher for the TP data, which is not surprising since TP is expected to reflect the force on the slider, while W2 distance measures the temporal difference in PDs.

Considering next the results for non-zero lags, we note a different behavior of r_{f*} and r_{v*} curves, with r_{v*} curves rising from negative to positive as lag is increased. Such difference results from the fact that the structure of the force and velocity profiles are rather different. The velocity profile shows sharp transitions, while the force profile slowly builds up during the stick periods and drop dramatically at the events. More importantly, we note that within a reasonable range of positive lags, the r_{fw} and r_{ft} are still significant in size, suggesting a potential for predictability. It should be noted however, that since the main part of the data is in a ”stick” region, the correlation will naturally weight more on these data points. A more insightful procedure would involve correlating the measures just before

a slip event. Such an analysis would however require more data points, and possibly also more detailed experimental input and therefore we leave if for the future work.

Before closing, we note that for Experiment 2 and 3 we obtain consistent results, however the correlations are weaker; e.g., the max of r_{ft} goes down from 0.65 (Experiment 1), to 0.45 (Experiment 2), and to 0.3 (Experiment 3). Despite the fact that all three experiments fall into the same category of stick-slip in the dynamic phase diagram [2], clearly (see Figure 3.3) the slip events are much stronger and better defined for Experiment 1, suggesting that in particular for such situation the persistence measures provide insightful information.

3.4 Conclusion

We find that the tools of persistent homology (PH) allow for correlating the dynamics of a slider and the photoelastic response of granular particles. In particular stick and slip regimes of the slider dynamics are well captured by the PH measures. These results suggest that there is a potential for developing predictive capabilities by analyzing the response of the force network to an external perturbation. One open question is how precise should the information about the forces between the granular particles be so to allow for further development of this potential. We hope that our results set up a stage for this future work.

CHAPTER 4

ON PREDICTING AVALANCHING

Avalanching is a phenomena that is well known on the geological scales, with a number of familiar examples, from earthquakes to snow avalanching and landslides [52]. The behavior that is seen on the large scales is statistically similar to the one observed in many other systems where the consequences are less spectacular, but are crucial for understanding material response that may be of significant technological importance. Relevant systems include dry and wet granular systems, suspensions, colloids, foams, yield-stress fluids, glass-forming materials, and a number of other soft matter systems relevant to our everyday life. The response of these systems to external driving is a subject of an active research area, with a large body of research considering intermittent response, where a considered system evolves via stick-slip type of dynamics [55, 62]. Developing predictive models that could inform about the conditions required for an avalanche (slip) is of significant relevance. So far, however, the progress has been limited mostly to the predictions of statistical nature. One would like to be able to come up with more precise predictions, or at least to be able to decide what type of information about the considered system would be needed so that such predictions are feasible.

4.1 Introduction

Granular systems are often explored in the context of intermittency since they provide a good testing ground for various theoretical approaches. Experiments provide significant information, and simulations based on discrete element method (DEM) are relatively straightforward. In particular (quasi) two dimensional (2D) systems are useful since observation of the results is simplified significantly.

One important question when considering intermittent dynamics is the connection between micro (particle scale) and macro (system size) behavior. Here, granular systems

are again useful since one can see and analyze not only particles, but also how they interact. In experiments, photoelasticity has been used extensively for this purpose [2, 3, 41, 45, 63, 172, 183]. From computational side, the corresponding information can be obtained directly from DEM simulations. Either approach identifies force networks that form spontaneously on mesoscale. By now, it has been widely accepted that these networks play an important role in determining system wide response. One open question is whether relevant information about intermittent dynamics can be extracted based on the properties of these networks.

The focal point of this chapter is the discussion regarding what type of data is needed to be able to predict an upcoming event. More specifically, the question is whether there are some characteristics of the force network describing the interaction between granular particles, or of the global dynamics of the system, that would allow to predict with a reasonable accuracy that the system is close to an avalanche. In addition to global measures, we will also discuss the differences between the information that can be extracted by considering stationary (static) and non-stationary (dynamic) data. To be able to come up with a precise answer to the postulated question, we will consider a very simple system of planar Couette shear, where one of the system boundaries is sheared in intermittent flow regime. We analyze the resulting stick-slip dynamics using a variety of measures, some of them classical, and some of them based on recently developed approach [100, 101, 103, 104, 105, 147] based on persistent homology (PH) and applied to force networks.

4.2 Simulations and Force Networks

The simulations are similar in spirit to the previous works [103, 104]; see Appendices A and B for more details. The 2D soft frictional bidisperse disks are placed between two rough walls, with 25% of large particles and 75% small particles, and the ratio of large diameter to small diameter is approximately 15.9/12.7 [58, 102]; the bottom wall is fixed and top

wall is exposed to a force by a harmonic spring, as well as to a pressure by applied force in the $-y$ direction, see Figure 4.1(a). It is well known that for a sufficiently large applied pressure, and for sufficiently slow shearing, the system enters into a stick-slip regime [144].

The simulation starts by applying pressure to the top wall, and then letting the system relax until the ratio of kinetic/potential energy drops below 10^{-5}. Then, we start moving the spring by a constant speed. The wall remains still until the spring force becomes sufficiently large and then slips. Figure 4.1(b-d) shows a short time window of the wall speed in the shearing, x, direction, as well as wall positions. in the x and y direction. (Note that throughout this chapter the results are presented in nondimensional form, using as scales the smaller particle diameter, $d = 1.27$ cm, binary collision time, $\tau_c = 1.25 \times 10^{-3}$ s, and particle mass, $m = 1.32$ g, see Appendix B.) We note in passing that each slip is accompanied by a jump of the wall in the y direction due to Reynolds dilatancy effect, see Figure 4.1(c). To reach reasonable statistics, we carry out simulations for a long time so that a large number (400-500) of slip events occurs. We extract the force information every 10 time units, leading to the total of 3×10^5 data points.

For the future purposes, it is important to carefully define what a slip event is. In this chapter, we define slip event based on the top wall velocity in the x direction, v_x. First, we apply a relatively coarse velocity threshold of $v_f^* = 2 \times 10^{-3}$ (note that this threshold is an order of magnitude smaller than a typical velocity during a slip, see Figure 4.1(b)). We then calculate the mean, $\bar{v}_x$, and standard deviation, s_{v_x}, of v_x in the "stick" phase, and define the new threshold $v_f = \bar{v}_x + s_{v_x}$. Then, we define the beginning of a slip as t_0 when $v_x > v_f$. This gives $v_f \approx 2.5 \times 10^{-4}$, providing a rather stick criteria: essentially even very slow motion of the wall is considered as a start of a slip.

In what follows, we will discuss utility of various measures for the purpose of prediction when next slip event will occur. Some of these measures are based on the concept of force network, that we define first. We define the magnitude of the contact forces as a continuous scalar field, $f : C \to [0, +\infty)$, where C denotes the particles' contacts. The

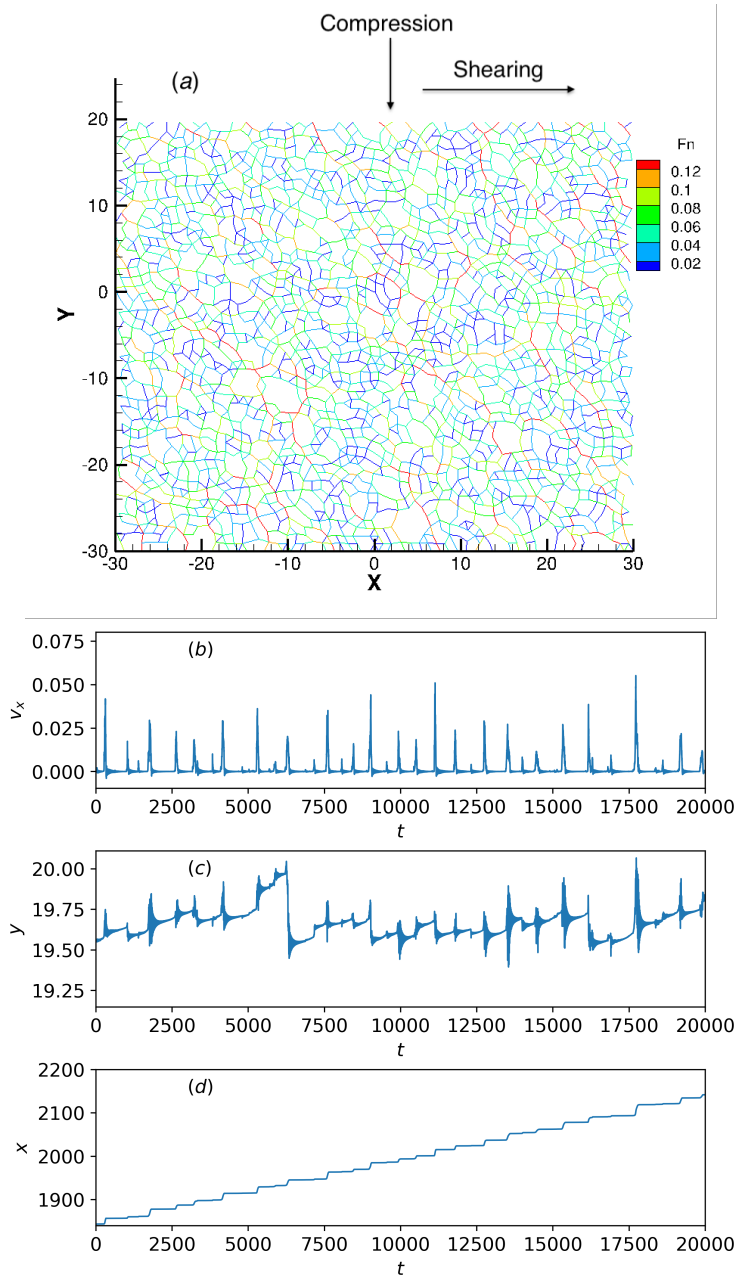

Figure 4.1 (a) Geometry of the simulations and snapshot of the force network. The arrow shows the direction of shearing (x axis) (y axis is pointing up). The wall particles are not shown. (b) Speed of the wall, v_x, in the shearing direction; (c) y position of the shearing wall, and (d) x position of the wall. Total of 300,000 outputs were recorded, and only a fraction of the used data is shown in (b-d). Note that the time (horizontal) axis is given in units of output time step, which is $\delta t = 10\tau_c$, see Appendix B.

force network at time t can then be defined as $FN(f;t) = \{c_i(t)|f(c_i(t))$, where $c_i(t)$ are the particle contacts that make up the force network at time t.

The force network can be quantified by the tools emerging from persistent homology, PH, which has been used extensively for the purpose for describing weighted networks in a variety of settings [83, 84, 106, 168]. While applications to granular systems are still rather limited, PH has been used for the systems exposed to compression [100, 104], vibrations [10, 101, 147], or shear [67]. In 2D, there are two independent sets of measures that could be considered, the ones based on the connected components (one could relate these to so-called 'force chains') and the ones based on loops (also called cycles [173]). The first set is related to the first topological invariant, zeroth Betti number, β_0, and the second one to the second topological invariant, or β_1. PH describes the given force network in terms of persistent diagrams, PDs, which are essentially point clouds, and then various measures could be extracted from PDs.

Perhaps the simplest measure that could be used to describe a PD and therefore underlying force network, is total persistence (TP) which essentially assigns a number to a force network based on its connectivity properties; one can define TP separately for β_0 (TP0) and for β_1 (TP1). We note that while TP is based on the concept of force thresholding, it includes the information about the connectivity at all threshold levels at once, and therefore does not require considering separately weak and strong forces.

In addition to considering static measures, derived from a state of the system at a given time, PH also allows for quantifying dynamics of the considered network. For this purpose, it is crucial to observe that these diagrams live in a metric space, and therefore the concept of distance between two diagrams is well defined. For our purposes here, what is important is that the distance describes in clear and precise terms the difference between two PDs and therefore by extension, the difference between the underlying networks. In this chapter, we will focus on the use of Wasserstein W2 distance, which is essentially an L_2 norm quantifying the difference between two PDs, see Subsection 2.2.4. The distance can be computed separately for the components and loops, therefore we have W2 for β_0 and β_1. One should note that the considered dynamical measures depend on the time interval

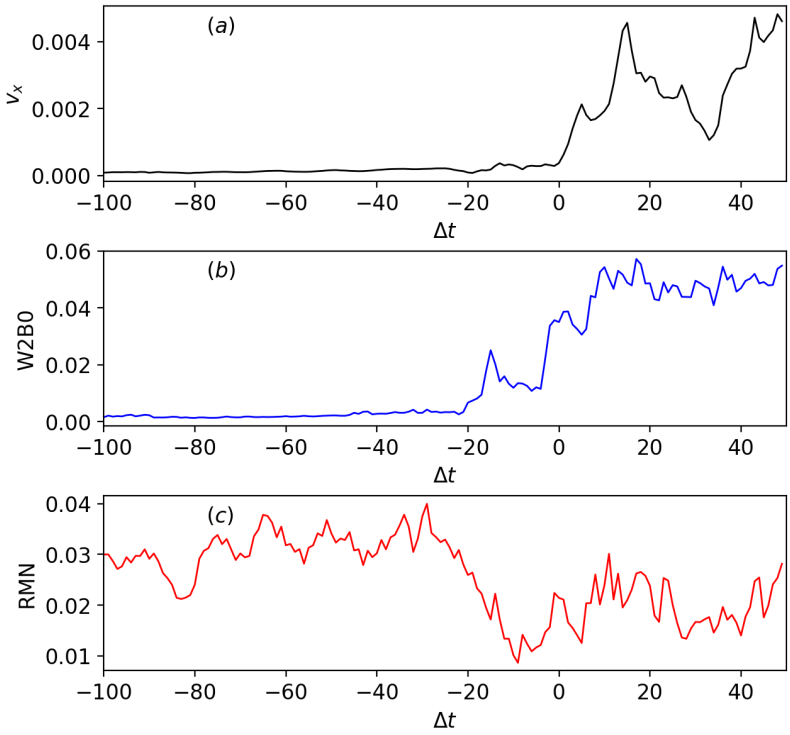

Figure 4.2 (a) Top wall velocity in the x direction, v_x, of an example slip event, $\Delta t = 0$ indicates the start of the event, (b) W2 β_0, (c) ratio of mobile to non-mobile contacts, RMN.

involved in their computation: we have verified that this difference is approximately linear for the considered time intervals. We note that for the purpose of PH-based analysis, in the present work we use the normal forces between the particles only.

4.3 Results

4.3.1 Motivation: A Single Slip Event

To motivate the analysis which will be presented in this section, we start by discussing briefly a single slip event. Here we also introduce another of the measures that we will consider, and that is the ratio of mobile to non-mobile contacts (RMN). The motivation for considering this measure is related to the expectation that application of shearing force will lead to an increase of F_t relative to F_n; ultimately, when the ratio F_t/F_n reaches the Coulomb threshold, sliding occurs, making a contact mobile. Therefore one could expect that RMN increases as a slip event occurs. Figure 4.2(a-c) shows velocity of top wall v_x,

W2 β_0, and RMN. Here, Δt measures the difference between t and t_0, in units of δt, where t_0 indicates the beginning of the slip event and δt is output time step. The velocity is very small before slip event starts, as expected based on our definition of t_0. W2 β_0, however, shows a significant change some time before beginning of the slip. On the other hand, RMN does not seem to provide any useful information, at least for the considered slip event. As we will see in what follows, this difference between the insight that can be reached from W2 β_0 and RMN appears to be generic, and reflects that difference in the information that can be obtained based on dynamic measures (such as W2) and static ones, such as RMN.

To illustrate more clearly the behavior of the system close to a start of a slip event, Figure 4.3 shows the heatmaps of the top wall position (a) and of W2 β_0 (b). These heatmaps show the difference in a value of a considered quantity between time $\Delta t = -100$ and $\Delta t + i\delta t$ ($i = 1,\ 150$ in Figure 4.3). From Figure 4.3(a) we conclude, as expected, that there is no observable motivation of the top wall (note that the slip event is identified to start at time $t_0 = 0$). However, Figure 4.3(b) shows significant changes of W2 β_0 *before* time zero: already 20-30 δt before the slip event starts W2 β_0 changes. This finding motivates more careful analysis of a large number of slip events to explore whether the described finding is general, and whether there are other measures that could be used for slip prediction.

4.3.2 Static Measures

We start by discussing some of the measures describing static properties of the system, obtained from observing the state of the system at a given time point. To obtain reasonably accurate representation of the data, we use the following approach: we record the starting time of each slip event, and then compute the relevant quantities for a certain time interval preceding a slip event. The question is whether, based on the behavior of the considered quantities before slip event starts, we could predict that a slip is imminent.

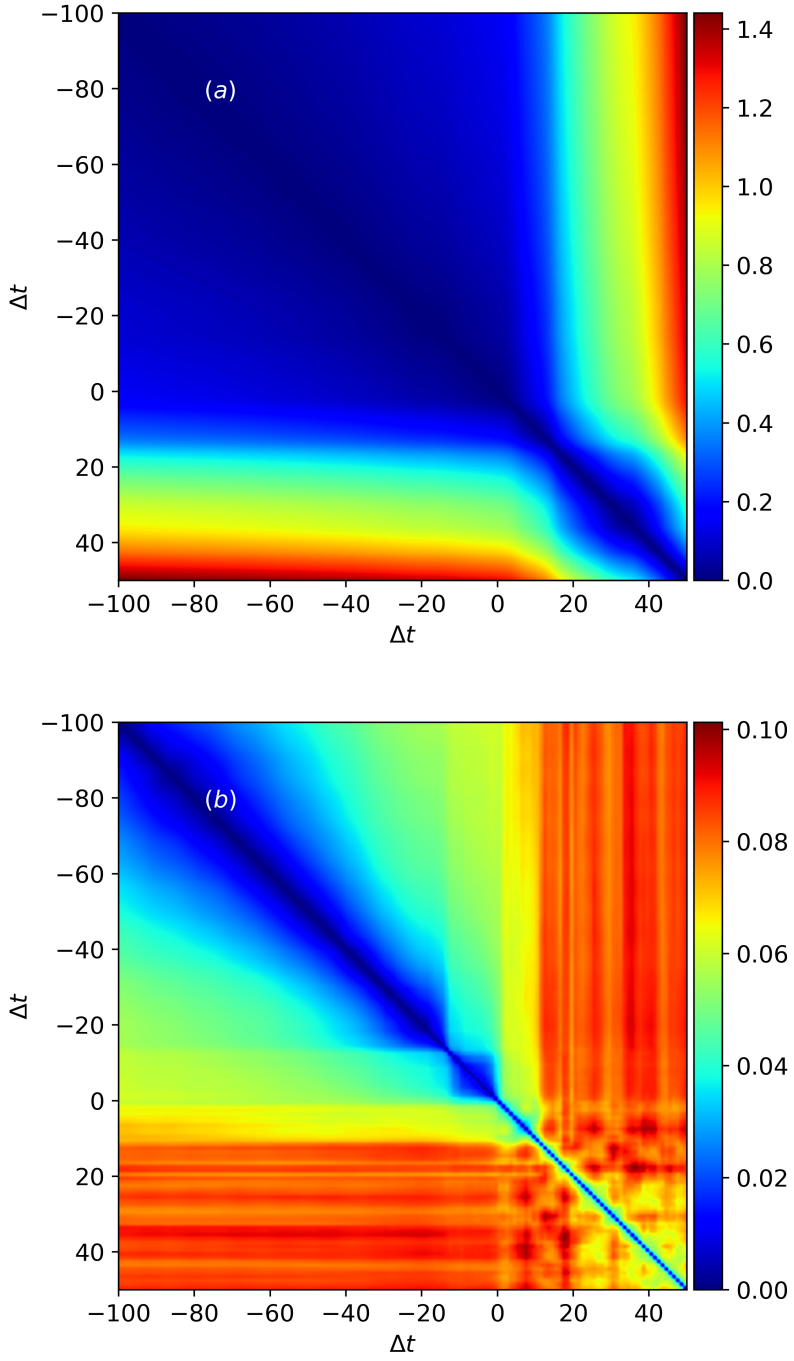

Figure 4.3 (a) Heat map (a symmetric matrix) of top wall position of the event shown in Figure 4.2, where the color of element (i, j) illustrates the difference of top wall's x position between time $\Delta t = i$ and $\Delta t = j$, (b) heat map of W2 β_0, where the color of element measures the distance between PDs at $\Delta t = i$ and $\Delta t = j$. Slip event starts at $\Delta t = 0$.

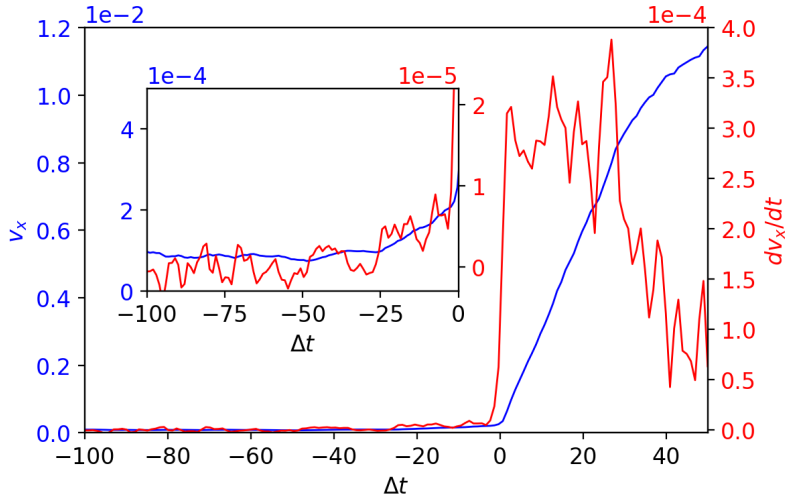

Figure 4.4 The mean of v_x and its derivative before slip events, averaged over slips events. Here $\Delta t = 0$ corresponds to the time the slip starts, t_0.

Figure 4.4 shows the mean of wall velocity, v_x and its derivative (acceleration) averaged over all slip events. We could see that v_x and acceleration remain flat and close to zero until t_0 is reached.

Figure 4.5 shows the measures that we have considered. We start with the most obvious measures that could be expected to have a potential to predict an upcoming slip event: (a) spring force, and (b) the y position of the top wall. We see that these measures increase only very slowly before en event, and therefore do not seem to have useful predictive abilities. Then, we consider (c) the ratio of tangential, F_t, and normal, F_n, forces between the particles, averaged over all contacts, (d) RMN, (e) total persistence for components, TP0, and (f) total persistence for loops, TP1. Note that the oscillations seen in Figure 4.5(f) are due to very small oscillations of the top wall, barely visible in Figure 4.5(b), illustrating how sensitive measure TP1 is.

Figure 4.5(c-f) shows that the considered measures, all based on static information, do not provide information that could be useful from the point of view of predicting upcoming slip event. They mostly slowly grow as a slip event approaches, however this growth is very gradual and difficult to use for predictive purposes. We conclude that at least

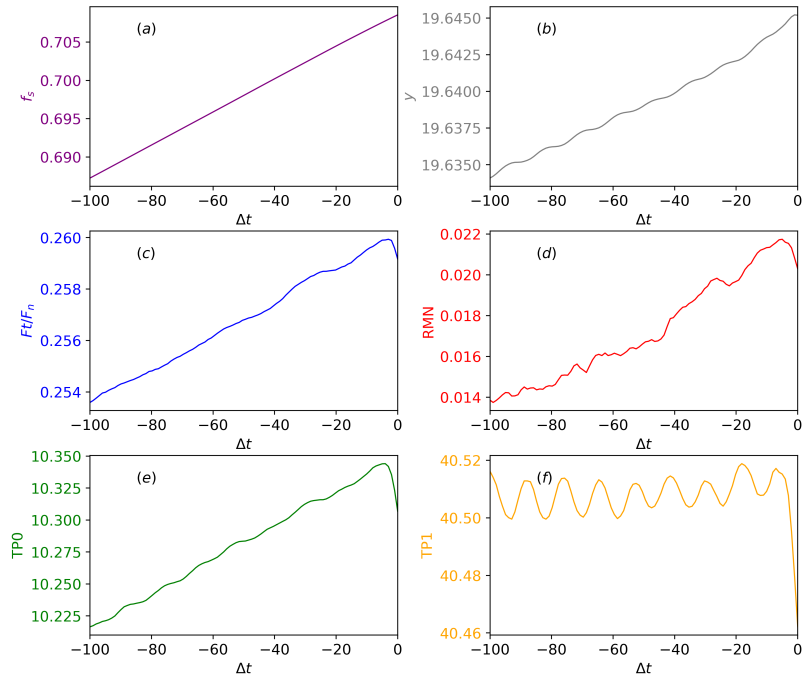

Figure 4.5 (a) spring force, f_s, (b) y position of the top wall, (c) the ratio of F_t/F_n, (d) the ratio of mobile to non-mobile contacts, RMN, (e) TP0, (f) TP1.

for the present system, developing prediction based on the considered (static) measures is not feasible. See additional discussions of static measures in Appendix D.

4.3.3 Dynamic Measures

We proceed by discussing the results that could be obtained by considering dynamic information, and by this we mean the information which can be extracted by considering system evolution, and therefore based on more than a single state of the system. Figure 4.6 shows the results for the dynamic measures that we have considered, averaged over all slip events. One set of measures that is rather natural to consider is based on broken contacts. One could expect that even before slip actually starts, there could be local rearrangements of the particles taking place, leading to breaking up of the contacts. Note that this measures involves dynamics of the particles: the particles need to move in order for contacts to break. We consider two measures: the average broken normal force, and the number of broken contacts. The broken contacts can be defined as the difference between the contact network

C between time t and $t+\delta t$, $BC(t+\delta t) = C(t) - C(t+\delta t)$. The broken contact number, bc, and total contact number, tc, at time t are $bc = \sum_{c\in BC(t)} 1$, $tc = \sum_{c\in C(t)} 1$. Hence, the broken contact ratio is defined as $r_{bc} = bc/tc$. The broken normal contact force at time t is $f_{bc} = \sum_{c\in BC(t)} \|f(c)\|/bc$, where $f(c)$ is the normal component of the broken contact force.

Another two sets of measures are based on the (dynamic) properties of the normal or tangential force network itself and do not involve particle dynamics. The first set is rather intuitive and it emerges from observing the 'differential force network', which is the difference between the network at the times t and $t+\delta t$. The animations of such differential force networks show that just before a slip event, this network appears to percolate across the domain (in either x or y directions, or both) for nonzero level of force, and snapshots of the animations are shown in Figures D.2 and D.3 in Appendix D. One obvious question is whether such percolation can be used to suggest that a slip is imminent. We define the differential normal force network between time t and $t+\delta t$ given a threshold $\hat{f}$:

$$\begin{aligned} DFN_k(\hat{f}) &= |FN(f;t+\delta t) - FN(f;t)|_{\hat{f}} \\ &= \{c_i(t+\delta t) || f(c_i(t+\delta t)) - f(c_i(t))| \geq \hat{f}\}. \end{aligned} \tag{4.1}$$

The maximum percolating differential normal force is the threshold of differential normal force f^* at which $DFN(f^*)$ percolates through the whole system via system particles. The f^* is calculated in both directions from left to right, notated as f_{plr}, and top to bottom, as f_{ptb}. Similarly, we could define the differential tangential force network and its corresponding percolating threshold, see Appendix D for more detail.

We also consider the mean of system particles' speed, $\bar{v}_p$, and its standard deviation, s_{v_p}, as dynamic measures, which can be calculated from the magnitude of system particle velocity, where $\bar{v}_p = \sum_{i=1}^{N} v_i/N$, $s_{v_p} = \sqrt{\sum_{i=1}^{N}(v_i - \bar{v}_p)^2/N}$, and v_i is the speed of system particle i, N is the total number of system particles.

Figure 4.7 shows all described dynamic measures in the format similar to Figure 4.6. We observe no different behaviors of the measures considered in this figure: they all change

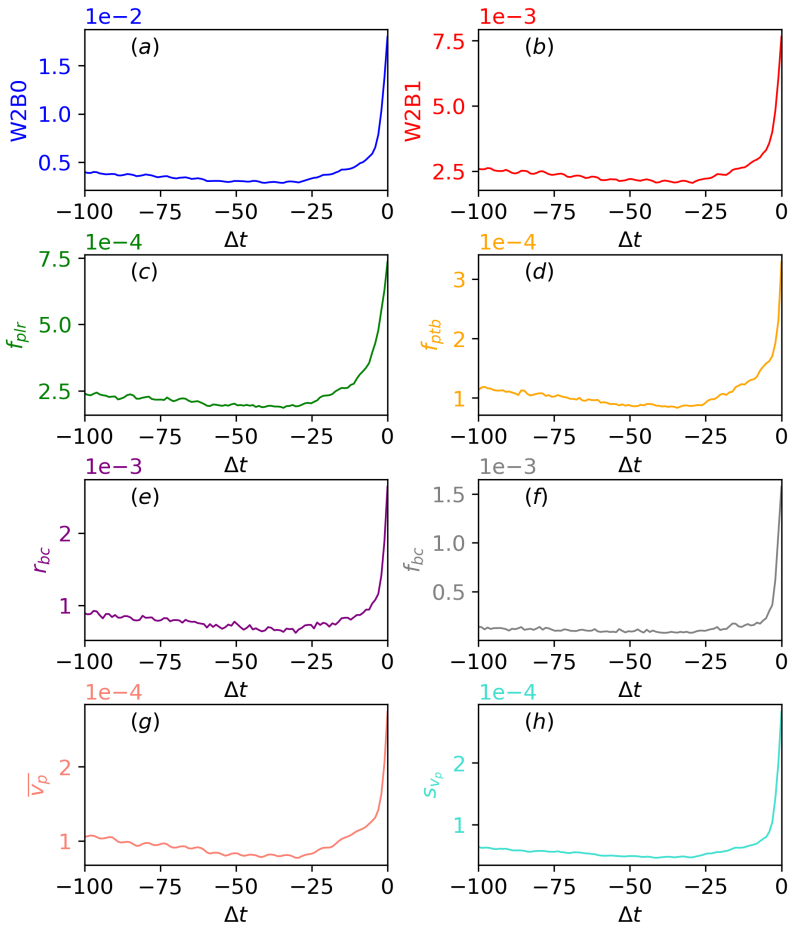

Figure 4.6 (a) W2 β_0 distance, (b) W2 β_1 distance, (c) the horizontal percolating differential normal force, f_{plr}, (d) the vertical percolating differential normal force, f_{ptb}, (e) the ratio of broken contacts to total contacts, r_{bc}, (f) the average normal force of broken contacts, f_{bc}, (g) the mean of system particle speed, $\overline{v_p}$, (e) the standard deviation of system particle speed, s_{v_p}.

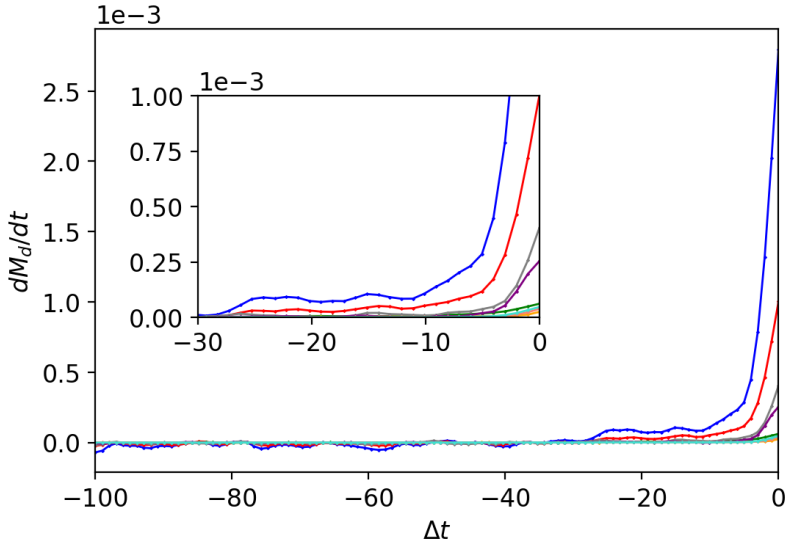

Figure 4.7 Derivatives of dynamic measures, presented with different colors as W2 β_0 (blue), W2 β_1 (red), maximum percolating differential normal force from left to right f_{plr} (green), maximum percolating differential force from top to bottom f_{ptb} (orange), ratio of broken contacts to total contact number r_{bc} (gray), average broken contact force f_{bc} (purple), average system particles velocity (salmon), standard deviation of system particle velocity (turquoise). The inset zooms into the range of [-30, 0].

dramatically *before* a slip actually takes place. In addition, we note that the considered measures start evolving earlier and earlier, with the earliest changes observed for the persistence distances, in particular the W2 β_0. These results suggest that it should be possible to anticipate upcoming slip event by considering evolution of underlying force network.

4.4 Conclusion

In this chapter, we introduced two ways to measure a granular system, either dynamically or statically. We further discussed the insights into the precursors to slip events of a 2D dense granular system from these two measures. As a dynamic measure, we introduced the concept of differential force network and the percolation of these differential force networks before slips. Thus, we have identified a set of dynamic measures that show promise to be able to predict avalanching type of behavior in the considered system. The

general pattern of the results (both for the measures discussed here and for other ones not discussed for brevity) is that dynamic information needs to be included in order for a considered measure to have predictive power. The discussion of slip statistics and its relations between static and dynamic measures is presented in Appendix D. While our findings are based on the computational results, we hope that they will inspire future experiments that will be positioned to verify our findings in an experimental setup as well.

CHAPTER 5

UNDERSTANDING SLOW (DE)COMPRESSION OF GRANULAR MATTER

5.1 Introduction

In non-Newtonian systems, complex fluids [77], colloidal suspensions, [136], and especially granular matter in its flowing states [88], the transport coefficients depend on various state-variables such as the density and the granular temperature [145]. This interdependence and the presence of energy dissipation is at the origin of many interesting phenomena like clustering [121], shear-band formation [113], jamming/un-jamming [32, 75], dilatancy [149], shear-thickening [129, 136, 163] or shear-jamming [32, 111, 187]. While granular gases are very well described by kinetic theory [145], dense granular fluids and granular solids are much harder to understand, in particular since they can transit from fluid-like flowing states to static, reversibly elastic ones. How and why they achieve this is still under debate, e.g., by irreversible plastic deformations [61, 119, 128, 186, 197], related also to creep/relaxation [8, 36, 87, 149], and many other studies.

In order to describe solid-like granular matter on the macroscopic scale, concepts from elasto- and visco-plastic theories were used [6, 7, 59, 61, 71, 72, 94, 112, 178, 185, 186] including instabilities, yield and failure [50, 51, 76, 137, 159, 160, 185, 189, 193, 202]. Recently, statistical mechanics/physics concepts [80], helped to better understand the probabilities for plastic deformations [34, 72, 90, 91, 111, 119, 128, 197], force network change/growth [146, 151], stress-based meso ensembles [31], or stress-relaxation [36, 37, 87, 149]. A traditional subject of research are stress-fluctuations [26, 109, 132, 177], and the quest for the "effective temperature" [81, 90, 91, 139] of thermal or a-thermal granular packings [31, 91, 194]. Most recently, universal scaling laws [16] were reported, and compression and shear in particularly small systems [192] could be understood. Considering granular solids, their stiffness, and the elastic moduli [24, 46, 112] have to

be considered in the presence of non-affine deformations [46]. For this, over-compression and shear [16, 24, 111, 188, 198] cyclic loading [13] or even thermal cyclic loading [86] were applied.

When sheared granular matter starts to flow and (for large enough strain) reaches a steady state, or critical state [123, 163, 200], the nowadays widely accepted "classical" $\mu(I)$-rheology [131] holds. It was recently extended to include friction, softness and cohesion [27, 28, 123, 129, 150, 200], but it does not have a fully tensorial form [162, 190], and issues regarding its wellposedness are still discussed [20, 73, 154].

Modern experimental techniques [8, 15, 191], also with focus on low confining stress [42], shed new light on classical works on the response to local perturbations [68], jamming and un-jamming [36, 49, 68, 127, 138], in particular by shear [16, 32, 111, 122, 156, 179, 188], and transients, fabric/micro-structure evolution [26, 112, 111, 125, 142, 181, 183]. One of the classical experimental techniques involves photoelastic materials that allow to visualize stress [3, 17, 35], as complemented by a huge amount of particle simulations, e.g., see [38, 113] and references therein.

One important success of granular research was to bring solid-like and flowing behavior of granular matter together, e.g., in a continuum theory with fluidity [79, 90, 91, 197], and to understand anisotropy [125, 142, 181, 200], also shape induced [63, 135], as well as involving the rotational degrees of freedom and micro-polar models [27, 78, 108, 130, 152, 184], not to forget wet particle systems [136, 167], for which a thermodynamically consistent theory [60] and numerical solutions [23] were recently proposed.

Dynamics of dense granular matter is necessarily related to the evolution of the force networks describing the interparticle interactions. By now it is well accepted that the static and dynamic properties of these networks are closely related to the mechanical properties of a whole granular sample. It is therefore important to be able to describe the properties of these networks in a way which is simple but also precise, and that could be applied in three

spatial dimensions (3D). This is not an easy task since the force networks are built on top of contact networks, which for a dynamic system evolve as well. While there is a number of various approaches that could be used to describe the considered networks, they often do not satisfy some of the requirements specified above. In the present work, we focus on application of persistent homology, which is a technique based on computational topology allowing for a concise description of weighted networks, and is therefore appropriate for description of force networks, where the role of weight is played by the magnitude of the force (normal or tangential) between granular particles. Persistent homology allows for a significant data reduction, since it describes a complicated weighted network in terms of a point clouds, known as persistent diagrams, that contain the information about connectivity of the force networks, and how such connectivity depends on the force magnitude. One strength of this approach is that all force magnitudes can be considered at once, that is, it is not necessary to, e.g., separate the network into weak or strong network. This being said, the concept of force threshold is inherent in persistent homology calculations and the information about the connectivity for different thresholds is readily available.

Persistent homology has been extensively for a number of systems involving weighted networks, ranging from social [168] to fluid dynamics [106] and material science context [83, 84]. While applications to granular systems are still rather limited, the approach based on persistent homology has been used for the systems exposed to compression [100, 104], vibrations [10, 101, 147], or shear [67]. In the present work, we will illustrate some of the strengths of this approach, including ability to easily carry out computations in 3D, as well as to consider evolving networks, including computing their differences. The computations are carried out using Gudhi library [1].

The remainder of this chapter is structured as follows. After discussing discrete element and persistent homology methods in Section 5.2, we proceed to discuss the results. Section 5.3 focuses on the preliminary discussion of the transitions, which are essentially irreversible events frequently occurring both during compression (loading) and

decompression (unloading) of the considered granular system. Then, in Section 5.4 we follow by discussing the results obtained by applying persistent homology analysis to the considered system, as well as by developing the relation of the quantities derived based on persistent homology to classical measures, such as pressure or kinetic energy. The discussion in Sections 5.3 and 5.4 focuses on frictionless particles. Then, in Section 5.5 we follow up by describing the results of simulations of frictional particles, focusing on the differences between frictionless and frictional results. Section 5.6 is devoted to the summary and conclusions.

5.2 Methods

5.2.1 Introduction to Discrete Element Method

The approach towards the microscopic understanding of macroscopic particulate material behaviour is the modelling of particles using the so-called discrete element method (DEM), a numerical scheme originally formulated and developed by Cundall et al [47].

DEM is a straightforward implementation to solve the transitional and rotational equations of motion for a system of many interacting particles:

$$m_i \ddot{\mathbf{a}}_i = \mathbf{f}_i + m_i \mathbf{g} \qquad\qquad I_i \dot{\omega}_i = \tau_i \tag{5.1}$$

where m_i is the mass of the i-th particle with position x_i. It is subjected to two kinds of forces, one due to contacts with other particles ($\mathbf{f}_i = \sum_c \mathbf{f}_i^c$) and one due to volume forces (i.e., gravity acceleration, $\mathbf{g}$ which are neglected in this study. I_i is the spherical particles moment of inertia, $\dot{\omega}_i$ is the angular velocity and $\tau_i = \sum_c (\mathbf{l}_i^c \times \mathbf{f}_i^c + \mathbf{q}_i^r + \mathbf{q}_i^t)$ is the total torque, where $\mathbf{l}_i^c$ is the branch vector and $\mathbf{q}_i^r$, $\mathbf{q}_i^t$ are torques due to rolling and torsion.

The basis of DEM consists of the force laws that relate the interaction force to the overlap of two particles. This force can be decomposed into a normal and tangential component $\mathbf{f}_i^c = \mathbf{f}_n + \mathbf{f}_t$. With the normal and tangential forces acting on all particles, one can numerically

integrate the equations of motion and obtain the next position of particles. Below, we will describe a force law used in this research.

Normal Contact Law The elementary units of granular material are mesoscopic grains which deform under contact forces, induced by an externally applied stress. For realistic modeling of the deformation of particles we relate the interaction force to the overlap δ of two particles. Note that the evaluation of the inter-particle forces based on the overlap may not be sufficient to account for the inhomogeneous stress distribution inside the particles. Two particles only interact if they are in contact, resulting in an overlap:

$$\delta^n = (r_i + r_j) - (\mathbf{x}_i - \mathbf{x}_j) \cdot \mathbf{n} > 0, \tag{5.2}$$

where $\mathbf{n} = (\mathbf{x}_i - \mathbf{x}_j)/|\mathbf{x}_i - \mathbf{x}_j|$ is the unit vector pointing from particle j to particle i.
From the equations of motion, Equation 5.1, it is apparent that the contact force is needed to determine particles trajectory. This force is calculated through a contact force law, which is a simplification of the contact between two particles. Linear contact model is the most simplified contact model in DEM which is a linear model based on the spring-dashpot theory of elastic contact [92, 120, 169, 195]:

$$f^n = f^n_{el} + f^n_{visc} = k_n \delta^n + \eta_n \dot{\delta}^n \tag{5.3}$$

with k_n as the spring stiffness between two particles. In reality, particles collisions are inelastic, i.e., energy loss occurs during collisions. Here, the dissipation is related to relative velocity ($v^n_{rel} = -(\mathbf{v}_i - \mathbf{v}_j) \cdot \mathbf{n} = \dot{\delta}^n$) of interacting particles with the viscoelastic damping constant for normal contact viscosity η_n which is an intrinsic material parameter.
This model assumes that the particles are spherical and do not deform during the simulation. In addition, this model considers binary contacts between two particles which means particles are in contact through a single point during their collisions.

Tangential Contact Law Modeling the tangential forces that arise from oblique particle impacts has elicited a considerably wider range of force models than those of normal interactions [5, 107, 114, 169]. Here, the tangential force is modeled by the theory of Mindlin [133]. When two contacting surfaces are subjected to an increasing tangential displacement, δ^t, then relative slip is initiated at the perimeter and progresses inward over an annular area of the contact surface. The incremental tangential force Δf^t due to the incremental tangential displacement $\Delta\delta^t$ depends not only on the loading history but also on the variation of the normal force. Therefore, the incremental tangential force is obtained from the following equation:

$$\Delta f^t = f^t_{i+1} - f^t_i \tag{5.4}$$

where f^t_{i+1} is the new and f^t_i is the old tangential force.

An approach based on the constant normal force solution of Mindlin was proposed by Tsuji et al. [174]. This approach is based on a linear tangential spring, k_t, with a stiffness coupled non-linearly to the normal displacement and was applied to a study on plug flow. Although strictly speaking, the proposed tangential model is only valid in case of a fully elastic material, it was combined with the non-linear viscoelastic model without adjusting any parameter [69]. Hence, the incremental tangential force is calculated as:

$$\Delta f^t = \Delta f^t_{el} + \Delta f^t_{visc} = k_t \Delta\delta^t + \eta_t \Delta v^t \tag{5.5}$$

where k_t is the tangential stiffness. Likewise the normal direction, we consider a dissipation term along the tangential direction using of viscosity term η_t [169] which is combined with the change of velocity along the tangential direction Δv^t.

The elastic tangential displacement, $\Delta\delta^t$, between spheres, obtained by integrating surface relative tangential velocities during elastic deformation of the contact and given as [157, 161]:

$$\delta^t = \int_{t_i}^{t_{i+1}} v^t dt \longrightarrow \Delta\delta^t = v^t \Delta t \tag{5.6}$$

where v^t is the component velocity tangent to the contact surface and Δt is the time-step. For the tangential degrees of freedom, we only consider sliding resistance between particles, rolling and torsion resistance are neglected for the sake of simplicity.

The tangential force as calculated in Equation 5.5 is subjected to the Coulomb's law attrition. Tangential force is calculated based on Equation 5.5 in the case of static friction, i.e., no slip. Dynamic friction happens when the tangential component of force, f^t, which was calculated from Equation 5.5, exceeds the maximum value of static force (μf^n), hence two particles start to slide against each other. In this case, the tangential force becomes $f^t = \mu f^n$ where f^n is the updated value and μ is the friction coefficient.

Input Parameters The $N = 4913$ particles, with particle diameters drawn from a random homogeneous size distribution with maximum to minimum width, $d_p^{max}/d_p^{min} = 3$, are the same as used in [111]. The parameters given in the following with a prime, e.g., $\rho_p^{'} = 2000$ or $d_p^{'} = 2$, are used in the simulations shown in this chapter. For working with units, there are two alternatives: Either one can read the numbers in chosen units or the units are chosen based on physical properties to achieve *non-dimensional quantities*. The latter option is adopted here, i.e., the unit of length is chosen as the mean particle diameter, $x_u^{'} = \langle d_p^{'} \rangle = 2$, so that $\langle d_p \rangle = 1$ is the dimensionless diameter. The second unit is the material density, $\rho_u^{'} = \rho_p^{'} = 2000$, so that one has the dimensionless density, $\rho = \phi$, and thus the unit of mass, $m_u^{'} = \rho_u^{'}(x_u^{'})^3$, i.e., the particle mass, $m_p = (\pi/6)$. For the third unit one has several choices, where we adopt here the units of elastic stress, $\sigma_u^{'} = k_n^{'}/d_p^{'}$, with the linear normal contact stiffness, $k_n^{'} = 10^5$, which yields the dimensionless stress $\sigma = \sigma^{'} d_p^{'}/k_n^{'}$, and results in the unit of time $t_u^{'} = (m_u^{'}/k_n^{'})^{1/2} = 0.4$ [1]. In the chosen units, the dimensionless linear stiffness is $k_n = k_n^{'}(t_u^{'})^2/m_u^{'} = 1$, and the linear contact viscosity, $\gamma_n^{'} = 10^3$, becomes $\gamma_n = \gamma_n^{'} t_u^{'}/m_u^{'} = \gamma_n^{'}/[k_n^{'} t_u^{'}] = 4 \times 10^{-3}$, with background viscosity,

[1] The alternative dimensionless stress: $\sigma_\gamma = \sigma^{'}/[\rho_p^{'}(d_p^{'}\dot{\gamma}^{'})^2]$, with the unit of time set by the shear rate, $t_u^{'} = \dot{\gamma}^{'}$, is more useful for collisional shear flows, see [180], and is thus not adopted here fore the sake of brevity.

$\gamma_b^{'} = 10^2$, or $\gamma_b = \gamma_b^{'} t_u^{'}/m_u^{'} = 4 \times 10^{-4}$. Following the parameters used for normal contact law, input parameters of tangential contact law are chosen to be $k_t^{'} = 2 \times 10^4$, $\gamma_t^{'} = 2 \times 10^2$ ($k_t = 0.2$ and $\gamma_t = 8 \times 10^{-4}$) with a friction coefficient $\mu = 0.1$. In this study, rolling and torsion resistance are not considered.

The consequent *physically relevant properties* are the restitution coefficient $r = \exp(-\eta_n t_c) \approx 0.855$, with damping factor $\eta_n = \gamma_n/(2m_{12})$, reduced mass, $m_{12} = 0.063$, and contact duration, $t_c = \pi/\sqrt{k_n/m_{12} - \eta_n^2} = 0.79$, or $t_c^{'} = t_c t_u^{'} = 0.316$, all considered for a contact between the largest and the smallest particle, with the larger viscous damping time-scale, $t_v = 2m_{12}/\gamma_n \approx 5$, and the even larger background damping time-scale $t_b = 2m_{12}/\gamma_b \approx 50$. Note that this choice of units corresponds to setting $t_u^{'} \propto t_c^{'}$, which corresponds to collapsing different stiffness simulations in the elastic regime [162, 180].

To prepare samples, first particles are randomly placed in a 3D simulation box with a periodic boundary condition at a low volume fraction, well below jamming point (transition point from liquid- to solid-like behavior). Then, the simulation box is compressed to homogeneously from all direction up to volume fraction $\phi = 0.9$ and then decompressed. Simulations carried out using isotropic strain-rate, $\dot{\varepsilon}_v^{'} = 1.05 \times 10^{-6}\,\mathrm{s}^{-1}$ ($\dot{\varepsilon}_v = 4.2 \times 10^{-7}$), for both loading and un-loading.

In the following sections, we will present a few typical particle simulations from loading-unloading cycles with the goal to zoom in to the slow rate data to display dynamics of what is going on during plastic, irreversible re-arrangement events.

5.2.2 Persistent Homology

For the present purposes, we could think of persistent homology (PH) as a tool for describing a complicated weighted network (such as the one describing interaction forces between the particles) in a form of diagrams, so called persistence diagrams (PDs). These diagrams are obtained by filtration, or thresholding, the strength of the interactions between the particles. As an example, let us assume that this strength is quantified by the normal

interaction force between the particles in the system. Then, the simplest persistence diagrams, which we refer to as β_0 PD essentially traces how 'structures' (could be thought of as 'force chains', without attempting to define them) appear as a filtration level is decreased, or disappear as two structures merge. Such a PD contains rather complete information about how connectivity between the contacts depends on their strength.

Figure 5.1 shows examples of the PDs computed at a given time for the system considered in the chapter (both for β_0 discussed above, and for β_1, that describes loops or cycles, and discussed further below). Each point (generator) in this diagram has two coordinates, 'birth' - specifying when (at which filtration level) it appeared, and 'death' - specifying when it disappeared, due to merging with another structure (as an example, consider two force chains: this chains will merge once the considered force threshold is decreased to the level of the force experienced by the particle contacts in between thee chains). Note that the term 'persistence' in this context refers to the force range over which a certain structure 'persists', or survives, as a considered filtration level is changed. We note that the number of PDs for a given network corresponds to the number of physical dimensions; therefore for 3D (three dimensional) system, there are three potentially relevant PDs: β_0, corresponding to components, β_1, corresponding to loops, also known as cycles [173], and β_2, corresponding to closed surfaces. The reader is referred to [158] for a more detailed overview of application of PH to dense granular matter from a physics point of view, and to [105] for a more in depth presentation. To facilitate understanding of the insight that can be reached by analysis of PDs, we briefly outline some of their properties:

- Persistence diagrams live in a metric space and therefore can be compared. This means that one can compare the weighted force network at different points in time, which is a crucial feature if one wants to understand an evolving system; we follow up on this by defining distances between PDs below.

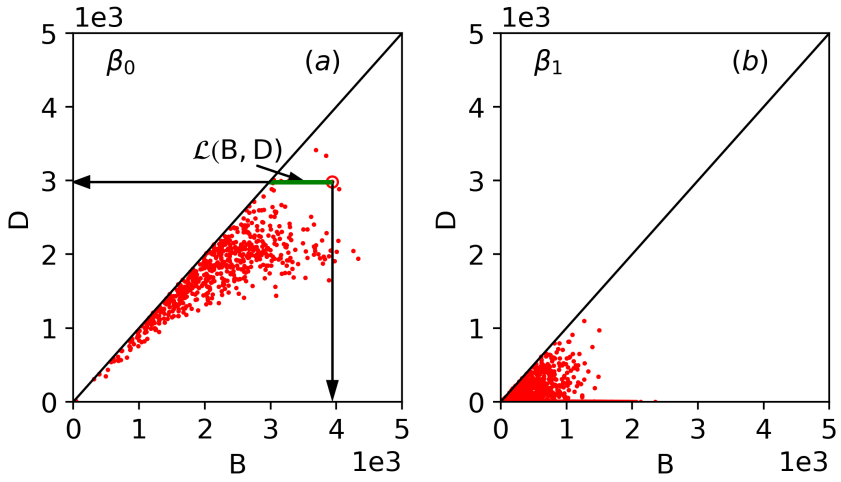

Figure 5.1 Examples of persistence diagrams, PDs, for (a) components (clusters), β_0, and (b) for loops (cycles), β_1. The axes show the force level at which a structure appears (B) and disappears (D) The lifespan $\mathscr{L}$ = B - D illustrates the force threshold range over which a structure persists.

- Since the description of a weighted force network in terms of persistence diagrams provides a significant data reduction, there is an associated loss of information, and therefore PDs do not provide full information about the underlying network. However, the information contained in PDs still provides for all practical purposes a reasonably precise insight into topological properties of the considered weighted networks.

- A PD provides information about a weighted network that is threshold independent; a PD provides information about all threshold levels at once. This is a major difference compared to other measures describing force networks, which often require separation of a force network into a 'strong' or a 'weak' network.

- The PDs are essentially point clouds, and an appropriate measure needs to be developed for their quantification. One possibility is based on the idea that both the number of points (generators) in a diagram, and for how long (that is, for how many thresholds levels) a point persists, are appropriate measures describing the force network between particles. Using landscape as an analogy, the number of points in β_0 PD specifies the number of (mountain) peaks, and their lifespan (see below) describes how well developed these peaks are, or, to push the landscape analogy further, how high they are compared to the 'valleys' that surround them. The lifespan, $\mathscr{L}$ is introduced as the difference between birth (B) and death, D, coordinates, so $\mathscr{L} = \mathrm{B} - \mathrm{D}$ (note that birth occurs on high threshold level than death). Both measures could be combined into one by defining total persistence, TP, as a sum of all lifespans. We will be using TP in discussing some properties of the force networks in the considered system.

- To further facilitate the information which can be extracted using PH based measures, let us connect them to some of the other concepts and quantities used in describing force networks. As mentioned above, the number of generators is related to the common (even if undefined) concept of force chains, and lifespan corresponds to how strong these force chains are. Then, β_1 measures can be related to the concept of cycles, properties of which are expected to be connected to the mechanical response of the system [173]. One important aspect of PH measures is that all these quantities are defined in a clear and precise manner which facilitates an objective description of static and dynamic weighted networks and of their evolution.

- As pointed out above, the number of PDs corresponds to the number of physical dimensions. For the system considered here, it turns out that the structures corresponding to β_2 do not form, and therefore our focus will be on β_0 and β_1 PDs. An interpretation of the lack of β_2 generators is that force networks in the considered system do not form closed three dimensional structures for the contacts with non-zero force. We are not aware that the consequences of this observation have been explored in the literature so far.

- The reader should note the enormity of the data reduction described so far: first a weighted force network is reduced to a point cloud (PD) and then this point cloud to a single number (TP). Such a reduction clearly leads to huge data loss, but as we will see, still provides an insightful information about the underlying weighted network.

PDs provide information about the state of the system at a given time, and do not include any information about the dynamics. As pointed out, however, PDs can be compared, and in particular the concept of *distance* between PDs is well defined [105]. The distance between two PDs could be thought as a minimum (Euclidean) distance by which the points

in one diagram need to be adjusted to map them exactly to the other one; if the number of points in two PDs is different, then extra points are mapped to the diagonal. Stated formally

$$Wq(\mathsf{PD},\mathsf{PD}') = \inf_{\gamma:\ \mathsf{PD}\to\mathsf{PD}'} \left(\sum_{p\in\mathsf{PD}} \|p-\gamma(p)\|_\infty^q \right)^{1/q}. \tag{5.7}$$

Here, Wq stands for the degree q Wasserstein distance, and PD, PD$'$ are the two considered PDs. Computing the distance is a computationally expensive process in particular for complex diagrams with many points. In the present work, we focus on $q=2$ for simplicity, and perform calculations using the Gudhi library [1].

5.3 Frictionless Particles: Analysis of DEM Results Based on Classical Measures

In this section, we compare the loading and unloading branches at the full range of volume fractions during the strong loading, overcompression, and unloading. Here, we focus on DEM particle simulation output/information, whereas in the next section, we will discuss in more detail the properties of force networks and their relation to the classical measures.

Figure 5.2 shows the results for the dimensionless pressure, $p = p'd_p/k_n$. Comparing to the results obtained using slower deformation, it is confirmed that already the simulation is in the quasi-static, rate-independent regime.

Figure 5.3 shows the energy ratio (kinetic to potential), E_k/E_p. It is a known fact that the energy ratio drops rapidly below unity at jamming [75], it sharply increases at unjamming, at a significantly different, larger value of ϕ. There are strong peaks whenever the system structure re-arranges during loading (blue) or unloading (red). A few of strong rearrangements are marked with △ and ◯ from loading and unloading branches, respectively, which are used for further study in the next section.

Next, we consider the coordination number C^* which is related to the contact number per particle $C = 2M/N$ (given the total number of contacts M) by $C^* = C/(1-f_r)$ in which f_r is the fraction of rattlers. Figure 5.4 shows that the coordination numbers, C^*, are very similar for the loading and unloading branches, i.e., on this scale, like for pressure, the

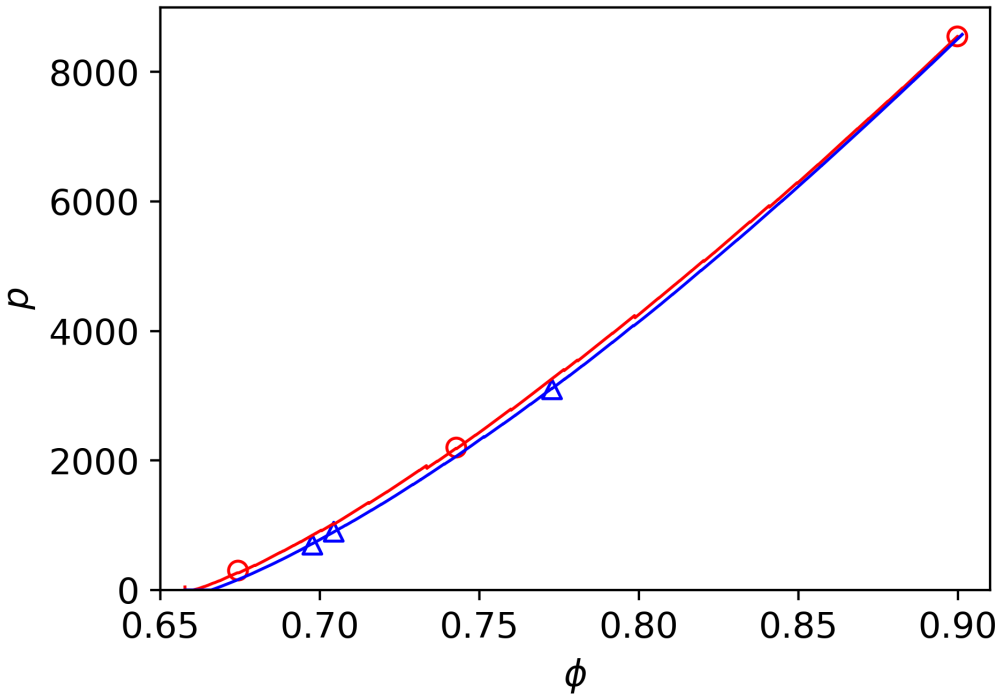

Figure 5.2 Pressure plotted against volume fraction, ϕ, for loading (L) (red) and unloading (UL) (blue). The symbols indicate the location of three selected simulation event windows, respectively, for both L and UL.

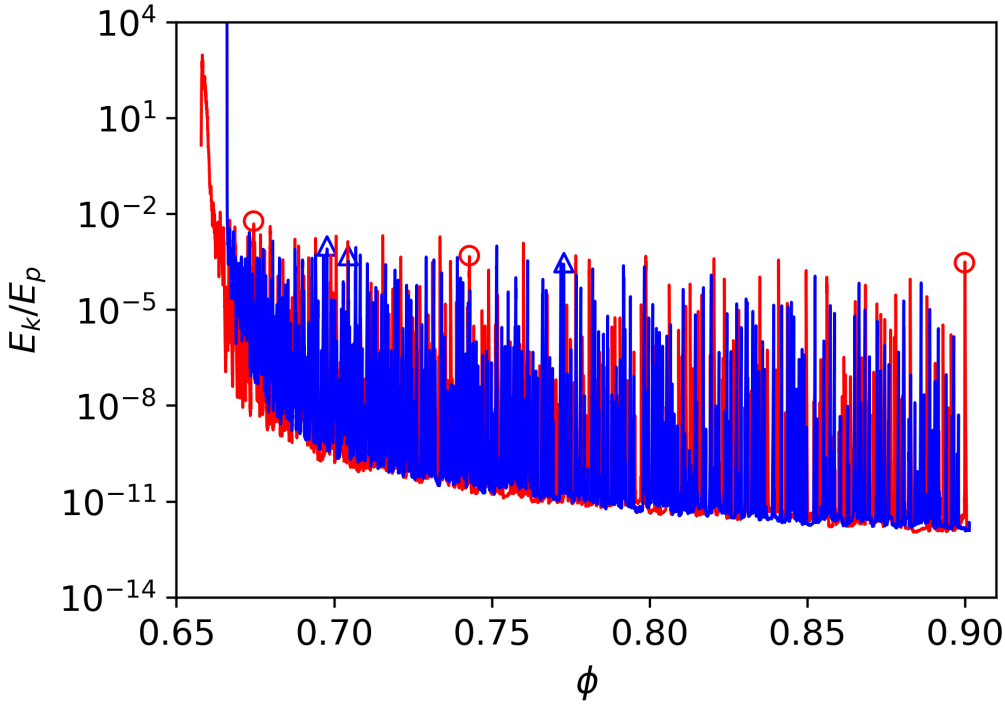

Figure 5.3 Kinetic to potential energy ratio, E_k/E_p, plotted against ϕ for the same simulations as in Figure 5.2, with the same colors/symbols.

tiny differences can be seen only when zooming in to the data, as we will do in the later sections.

5.3.1 Loading and Unloading Events

We proceed by comparing the loading and unloading branches at a few different selected values of ϕ so to be able to zoom into the rearrangement events marked in Figures 5.2-5.4.

When zooming into a small window of $\Delta\phi = \pm 0.0025$ around the value of ϕ at which an event takes place, the pressure, p, in Figure 5.5, differs significantly between loading (L) and unloading (UL). Only the last event on the loading branch is followed by an elastic regime that is exactly, reversible, elastically traced back during unloading from the maximum density $\phi_{\max} = 0.9013$, confirming reversibility for small enough strain rates and small enough strains.

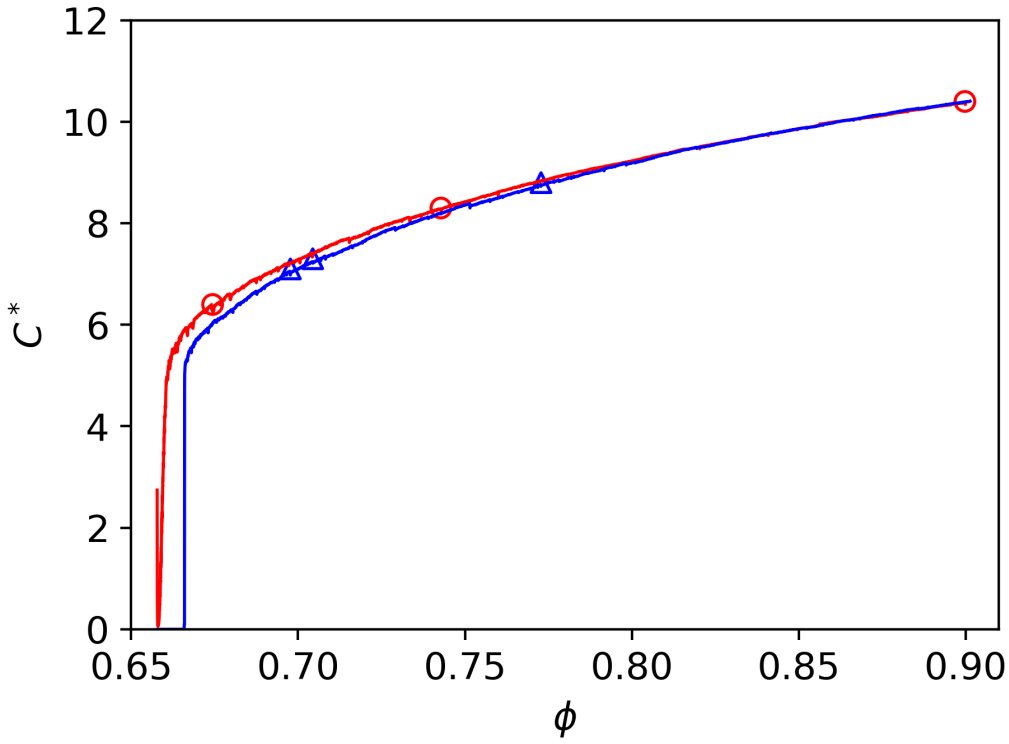

Figure 5.4 Coordination number, C^*, plotted against volume fraction, from the same simulations as in Figure 5.2, with same colors/symbols.

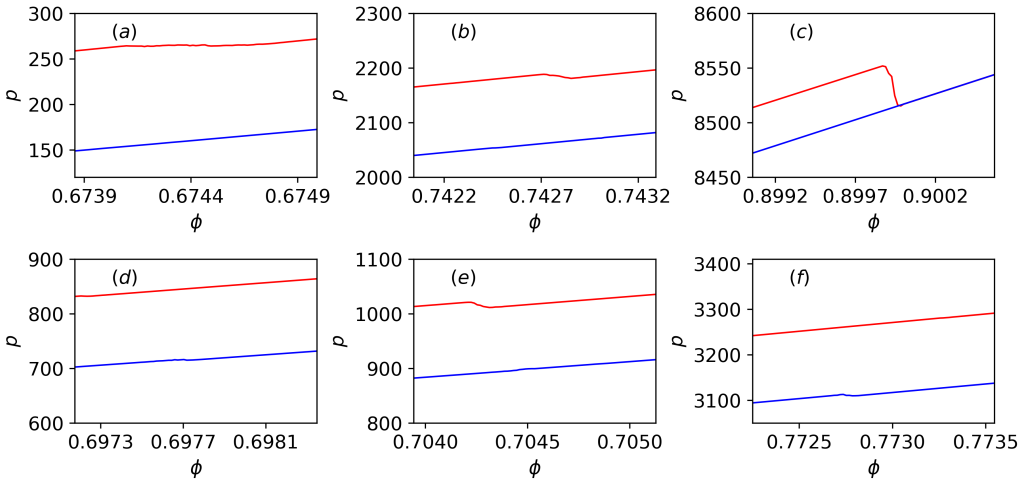

Figure 5.5 Pressure versus volume fraction, ϕ, from the same data as in Figure 5.2 (red and blue lines), but here zooming into three events on each branch, for loading (L) (red) and unloading (UL) (blue). The same color/symbols are applied to Figures 5.6 and 5.7. (a) L1, (b) L2, (c) L3, (d) UL1, (e) UL2, (f) UL3.

All the events are characterized by (sometimes tiny, sometimes large) changes in pressure: For L we observe pressure drops, while for UL, we also observe considerable increases in pressure (note that the UL figures need to be viewed from right to left since ϕ is decreasing).

Evidently, the energy ratio, E_k/E_p, changes frequently while looking at a zoomed window in Figure 5.6. It is not surprising to see the energy ratio during loading and unloading does not follow the same trend since the sample configuration has changed even though the overall ϕ is the same. What can be found is that before the start of rearrangements, the configuration tends to reach an equilibrium, i.e., decrease in energy ratio. To be more specific, one needs to look at the compression plots (red line) left to right and decompression plots (blue line) right to left, in which after every rearrangement the energy ratio decays before the start of the next local rearrangement.

To obtain the data at higher temporal resolution, we run the simulations at an arbitrary density before the start of an event until the next equilibrium state is reached. Even though the coordinate data available for the restart were only stored with 12 digits accuracy, the re-runs match perfectly.

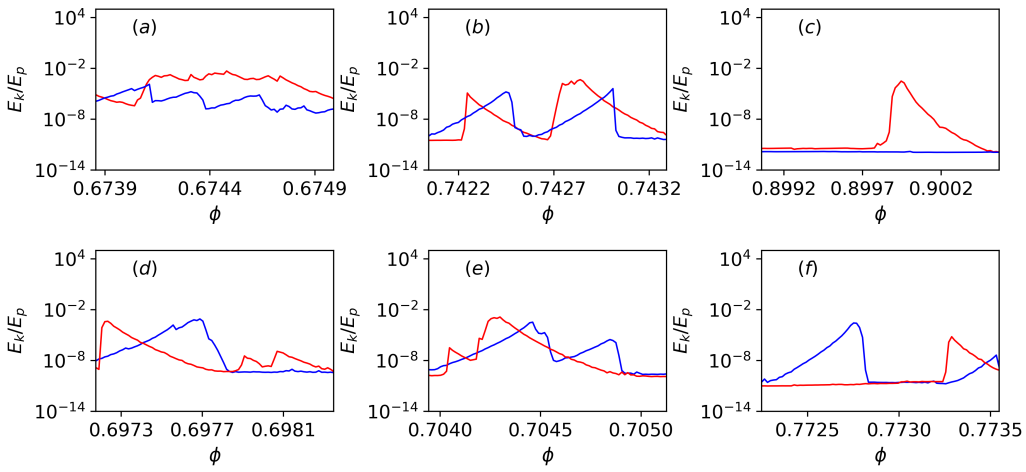

Figure 5.6 Kinetic to potential energy ratio, E_k/E_p, plotted against volume fraction, from the same events as in Figure 5.5.

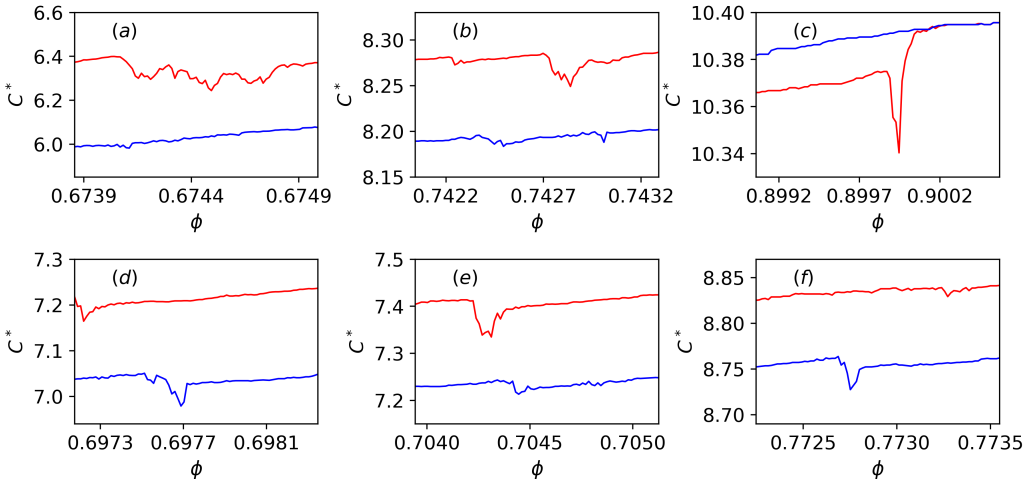

Figure 5.7 Coordination number, C^*, plotted against volume fraction, from the same events as in Figure 5.5.

Finally, the coordination number, C^*, in Figure 5.7, is plotted for the same data as in Figure 5.6. Similarly to the energy ratio shown in Figure 5.6, the coordination number plot reveals clearly the irreversible rearrangements before and after events. The path of the coordination number result remains in elastic regime before events taking place. Right after the start of an event, the coordination number drops. The drops show up when one of the two configurations has considerable energy ratio, E_k/E_p, which leads to opening and closing of contacts, i.e., local rearrangements. After the events, the coordination number recovers its original elastic path almost in all cases unless many local events take place simultaneously, restructuring the network configuration.

5.3.2 Events Contact Networks

In Figure 5.8, contact networks are plotted during events, for the loading branch only, with a threshold set such that the plots have similar density, even with a few holes/gaps that indicate extended islands of weak contacts only. The intensity of forces is color coded the same way in all plots, where blue, green, red range from low to high densities and, equivalently, forces.

The four snapshots shown in Figure 5.8 for each of the events L1 ($\phi = 0.6735$), L2 ($\phi = 0.742$), and L3 ($\phi = 0.899$), are equally spaced within the event window, $\Delta\phi \approx 0.00023$, so that biggest changes are expected between the two middle panels. However, given the rather small relative changes in pressure during events, also the force intensity change is practically invisible, and only a few changes in lines are visible. This observation brings us to the conclusion that the visualisation of the force network is not very helpful to understand the evolution during events; further analysis of these networks based on persistent homology method will be discussed in Section 5.4.

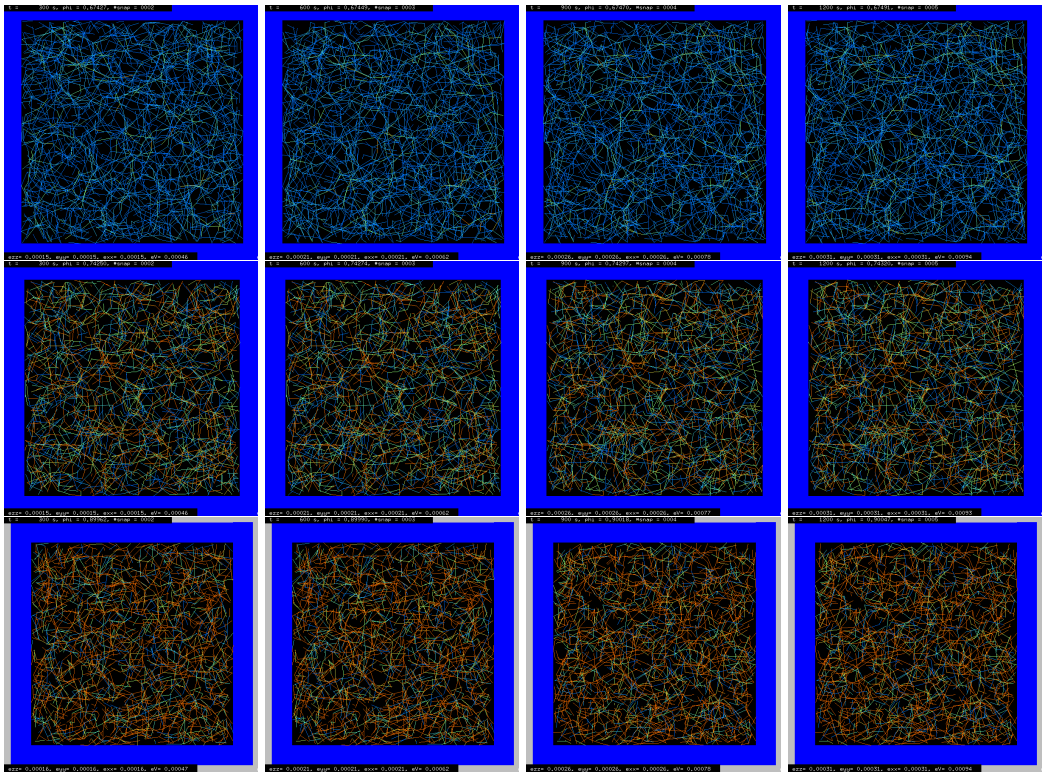

Figure 5.8 Force network during the three loading events L1, L2, and L3 (each event represented by a row of four snapshots), where the forces are plotted only above a threshold for the overlap of $\delta/(2R) > 0.006$, 0.04, and 0.11, respectively, while all lines are color coded the same way, from small (blue), moderate (green) to large (orange). Forces across the periodic boundaries are omitted.

5.4 Frictionless Particles: Force Network Analysis Based on Persistent Homology

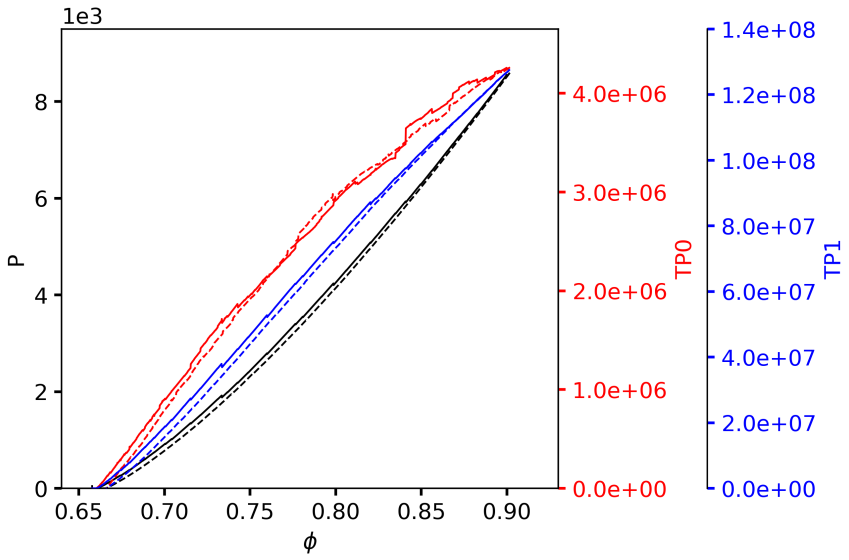

Figure 5.9 Loading (solid line) and unloading (dashed line) branches of pressure (black), TP β_0 (TP0) (red), TP β_1 (TP1) (blue).

Global view Figure 5.9 shows total persistence, TP, for components (β_0) and for loops (β_1), together with the pressure for both loading and unloading branches. There is a number of features to be noted. First, as expected, the pressure between loading and unloading measures differ, with loading pressure being always higher than the unloading one, for the same ϕ. Careful inspection of the pressure curves show also that the process of unloading is smoother than loading. Further comparison reveals also that TP for β_1 (TP1) closely follows the pressure, while TP for β_0 (TP0) is much more noisy. In particular, while the loading pressure is always larger than the unloading one, the same does not apply to TP0. We note that the evolution of TP0 is particularly nonuniform for large ϕ's, suggesting significant rearrangements of the force network.

We will discuss the fine features of the pressure and TP in what follows. Before that, we discuss the correlation between pressure and TP in more quantitative terms. For this purpose, we compute their correlation function. Since the functions that are correlated are rather noisy, we will consider the data averaged over a moving window, as described next.

The moving correlation between the two time series $x(t)$ and $y(t)$ is calculated by first finding the covariance between the subseries x_i and y_i in the moving window centered at time = t_0,

$$c^{t_0}_{w,s}(x,y) = \frac{1}{w} \sum_{x_i,y_i \in W^{t_0}_{w,s}} (x_i - \bar{x}_{t_0})(y_i - \bar{y}_{t_0}) \tag{5.8}$$

where $W^{t_0}_{w,s}$ is a selected window which centers at t_0, w is the total number of samples selected in W_{t_0}, and s is the sampling frequency. Also, $\bar{x}_{t_0}$, $\bar{y}_{t_0}$ is the mean of x_i, y_i.

The standard deviation, $s^{t_0}_{w,s}(x)$, of x_i at time t_0 is given by

$$s^{t_0}_{w,s}(x) = \sqrt{\frac{1}{w} \sum_{x_i \in W^{t_0}_{w,s}} (x_i - \bar{x}_{t_0})^2}, \tag{5.9}$$

with corresponding expression for $s^{t_0}_{w,s}(y)$. Then, the corresponding correlation function is

$$r^{t_0}_{w,s}(x,y) = \frac{c^{t_0}_{w,s}(x,y)}{s^{t_0}_{w,s}(x) s^{t_0}_{w,s}(y)}. \tag{5.10}$$

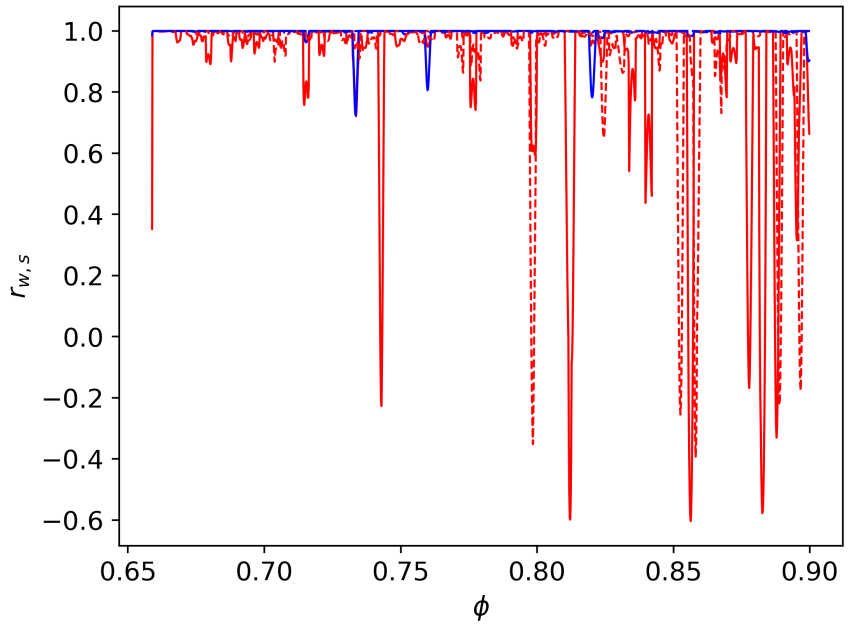

Figure 5.10 Correlation Coefficient between pressure and TP0 (red) and TP1 (blue) for loading (solid line) and unloading (dashed line) with $s = 1, w = 15$.

Figure 5.10 shows that the correlations between the pressure and total persistence TP (separately for TP0 and for TP1). We immediately observe that the correlation between pressure and TP1 is very high, in particular for the large values of ϕ. The correlation decreases only for few isolated events, which we discuss further below, but even for these events the correlation is still very strong. This result suggests that the properties of the loops in the force network are strongly related to the pressure. On the other hand, the correlation between TP0 and pressure is much more noisy, in particular during the rapid isolated events showing as peaks in the correlation curve. Therefore, the topological properties of the components are much less representative of the pressure in the system.

As already discussed above, the analysis of the considered quantities (pressure, TP) at the system is compressed suggests that the evolution is not smooth, but that it may include isolated events during which the structure of the system changes. We proceed by more detailed discussion of these events.

Analysis of the events Figure 5.10 suggests that a large number of events or transitions (tens or hundreds, depending on how an 'event' is defined) occur in particular during loading. In what follows, we consider few of these events, so to understand more clearly what kind of transitions they involve. We start with loading stage and consider first (on a much finer scale now) the pressure and total persistence, TP. Figure 5.11 shows the results, where all shown quantities are normalized by their value at the center of the event; for example, pressure is plotted as $\Delta p = (p - p*)/p*$, where $p*$ is the reference value shown by the arrow tip. We see that even on this very fine scale, and during a transition, TP1 closely follows the pressure. TP0 changes much more dramatically, showing that the topology of the weighted network changes during an event, but not all of these changes lead to pressure modification.

Figure 5.12 shows the same event from Figure 5.11 from the different perspective. Here we plot the distance between the persistence diagrams, defined by Equation 5.7,

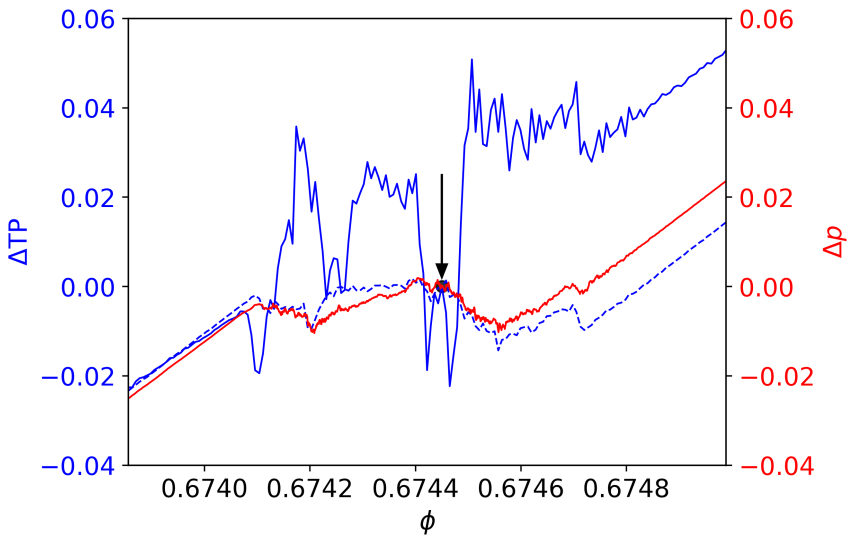

Figure 5.11 Normalized values for the pressure change Δp (red solid), ΔTP0 (blue solid) and ΔTP1 (blue dashed) for Event L1, all shown quantities are normalized by their value at the center of the event; for example, pressure is plotted as $\Delta p = (p - p*)/p*$, where $p*$ is the reference value shown by the arrow tip. The meaning of colors and line patterns is the same in the figures that follow.

together with the relative change of the kinetic energy of the particles. We see that the changes in $W2$ distances follow the changes in kinetic energy, although not too closely.

The fact that the $W2$ distances before and after an event are similar in Figure 5.12 inspires another question: is the topology of the force network before and after an event similar? To answer this question, we compute heat maps, which show the distances between all the persistence diagrams. Figure 5.13 shows the heat maps (both for W2 β_0 and W2 β_1 distances). This figure shows the heat maps as a (symmetric) square matrix, where the color of element (i, j) illustrates the distance between this element and the (i, i) one. By definition, the elements on the diagonal are zero. We see that the distances between the elements progressively increase as we move away from the diagonal, meaning that the topological properties of the system after and before an event are significantly different. The blue square regions (top left and bottom right) show that before and after an event, the distances between the PDs are very small (compared to the changes during an event).

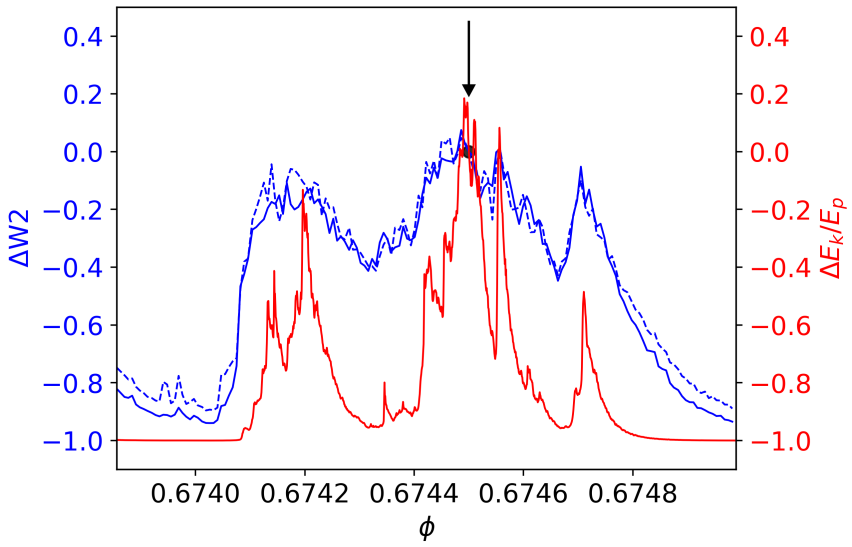

Figure 5.12 $\Delta W2$ distances both for β_0 (blue solid) and β_1 (blue dashed) as well as relative change of kinetic energy $\Delta E_k/E_p$ (red solid) for Event L1, and the arrow is pointing to the reference value used for normalization. The meaning of colors and line patterns is the same in the figures that follow.

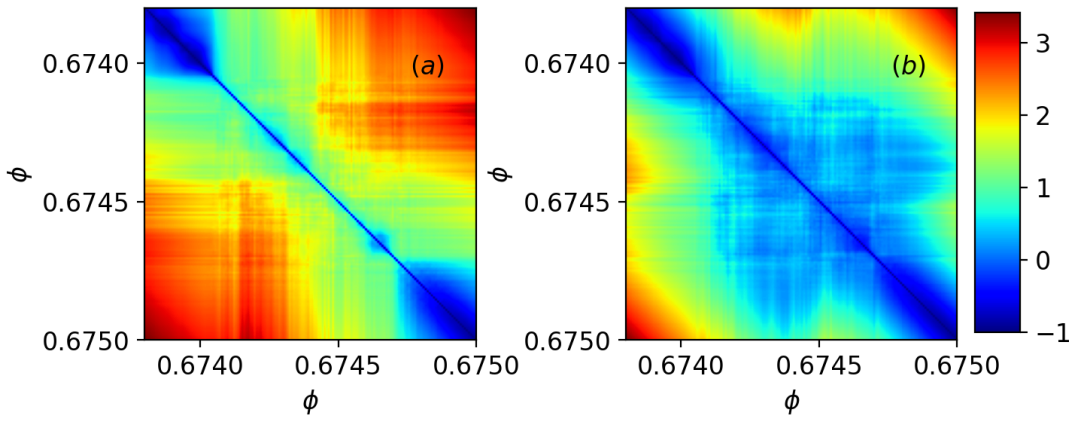

Figure 5.13 (a) Heat map (a symmetric matrix) of ΔW2 for β_0 of the event L1, where the color of element (i, j) illustrates the normalized distance of PDs for β_0 between $\phi = \phi_i$ and $\phi = \phi_j$, normalized by the same reference value used in Figure 5.12, (b) normalized ΔW2 β_1 distance.

To complete the discussion of the loading phase, Figure 5.14 shows two more events that occur for much larger ϕ. We see that the general features of the results are similar as already discussed. While TP1 closely follows the pressure, TP0 could increase or decrease during an event. Therefore, a general pattern of the results emerges: properties of the loops that form in the force networks are closely related to the material response, quantified by the pressure.

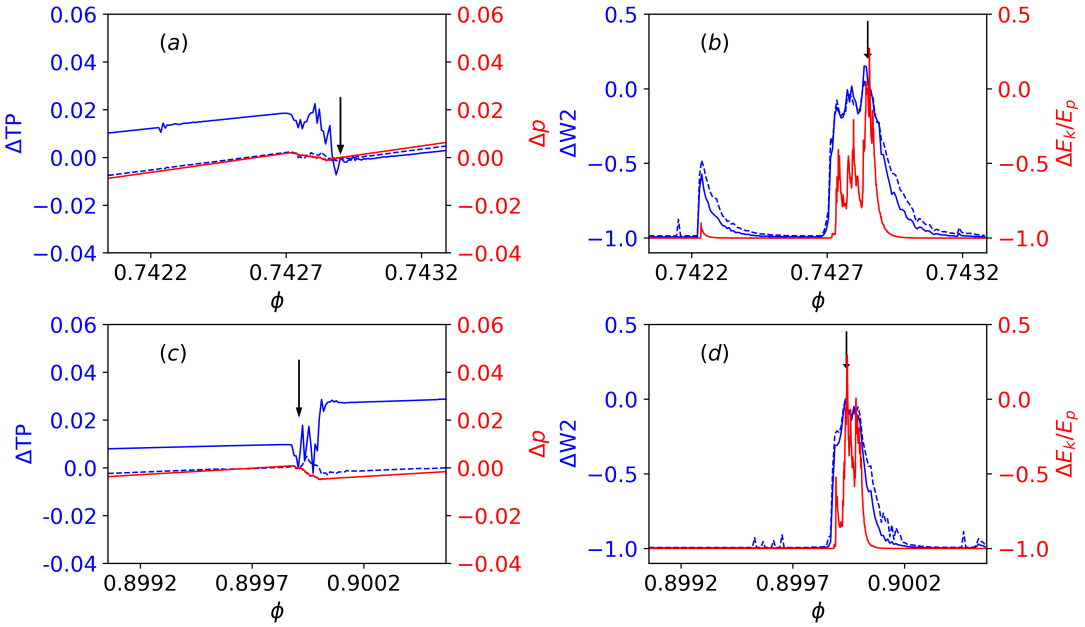

Figure 5.14 (a) L2, ΔTP0, ΔTP1 and Δp, (b) L2, ΔW2 of β_0 and β_1 and $\Delta E_k/E_p$; (c) L3, ΔTP0, ΔTP1 and Δp, (d) L3, ΔW2 of β_0 and β_1 and $\Delta E_k/E_p$, following the same format as in Figures 5.11 and 5.12.

Next, we proceed with discussing unloading. Figure 5.9 already suggests that this phase is smoother than the loading one, at least on the big scale. More careful analysis uncovers that there are still discrete elements during which rapid changes in the force network take place. Figure 5.15 shows three examples; we remind the reader that during unloading stage the system evolves from larger values of ϕ to smaller ones. The general features of the results are similar to the ones found for loading stage, with TP1 closely following the pressure, while TP0 evolves in a much more dramatic fashion, either increasing or decreasing during an event. Figure 5.15(c) shows an interesting feature for

$\phi \approx 0.7049$, where the distances between PDs show changes in the topology of force networks, although kinetic energy is unchanged - this example shows that the changes in the topology occur even without any motion of the particles.

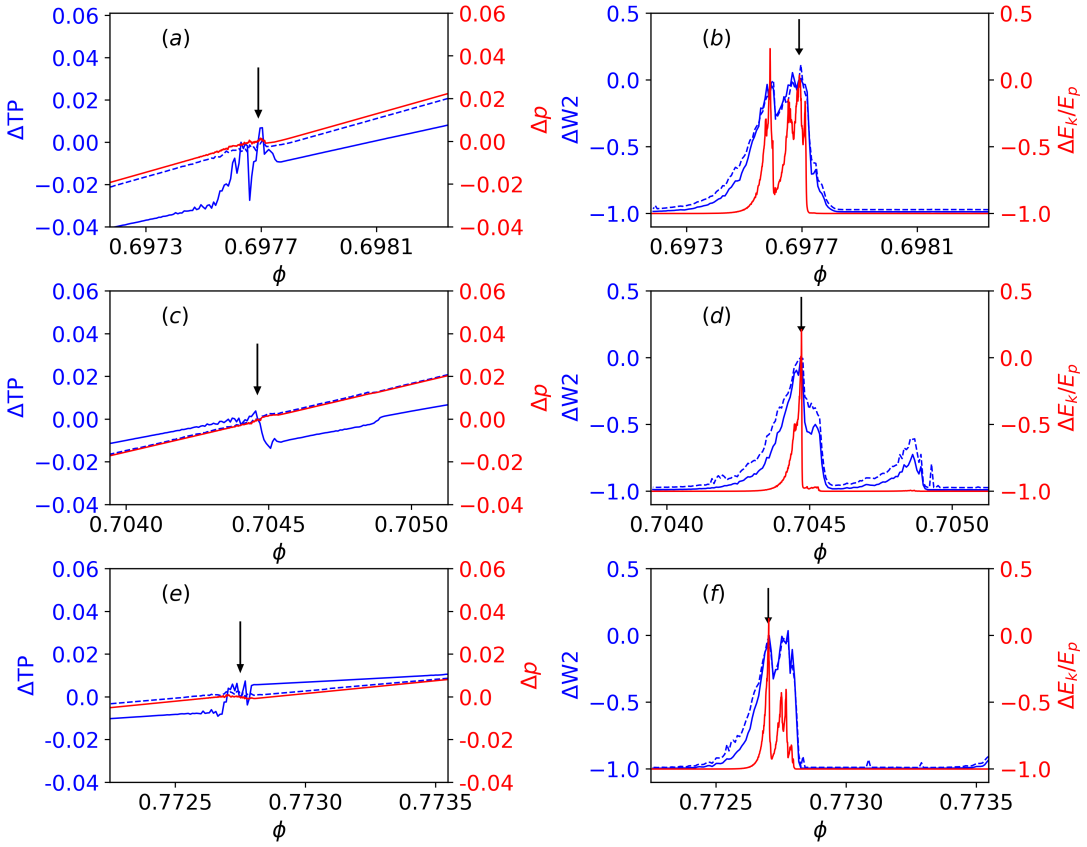

Figure 5.15 (a) UL1, ΔTP0, ΔTP1, and Δp, (b) UL1, ΔW2 of β_0 and β_1, and $\Delta E_k/E_p$; (c) UL2, ΔTP0, ΔTP1, and Δp, (d) UL2, ΔW2 of β_0 and β_1, and $\Delta E_k/E_p$; (e) UL3, ΔTP0, ΔTP1, and Δp, (f) UL3, ΔW2 of β_0 and β_1, and $\Delta E_k/E_p$, following the same format as in Figures 5.11 and 5.12.

Comparing loading and unloading phases, we note one perhaps unexpected feature of the results: all the events for the loading stage show pressure decrease; for unloading however, the pressure could either increase or decrease. This observation illustrates clearly the significant differences between loading and unloading phases.

Further discussion of some additional results that could be used to quantify the changes occurring during events could be obtained by considering in more detail the

ingredients that define TP: average lifespan of generators and their number. The corresponding results are given in Appendix E.

To conclude presentation of the frictionless results, we use the fact that a significant amount of information can be condensed in a visually simple-to-digest form using heat maps, and show in Figures 5.16 and 5.17 the heat maps for a set of ten loading and unloading events. Figure 5.16 shows that the distances are becoming larger as the system progresses to larger ϕ's. Generic features of the results do not appear to change significantly between loading and unloading.

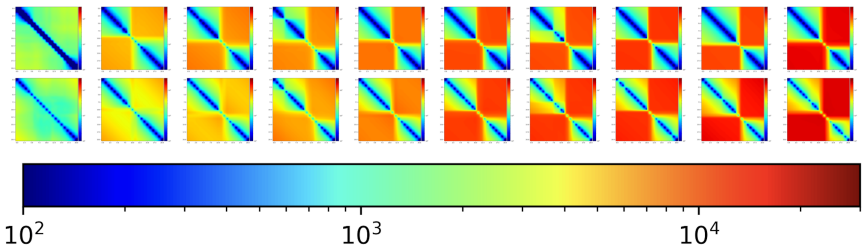

Figure 5.16 W2 β_0 (top) and W2 β_1 (bottom) heat maps for the selected ten events during loading; left to right, $\phi = 0.674, 0.700, 0.715, 0.742, 0.760, 0.798, 0.820, 0.840, 0.882, 0.899$. For this figure, the distances are computed only every eight outputs so to reduce computational cost.

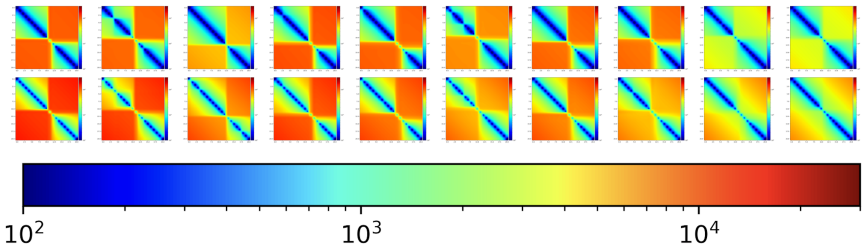

Figure 5.17 W2 β_0 (top) and W2 β_1 (bottom) heat maps in log-scale for the selected ten events during unloading; left to right, $\phi = 0.886, 0.866, 0.842, 0.798, 0.773, 0.761, 0.751, 0.729, 0.697, 0.694$.

5.5 Frictional Particles: Overview of the Results

In this section, we provide a brief description of the influence of friction between particles on the process of loading and unloading. Figure 5.18 shows the results for pressure, TP0

and TP1 for three values of the friction coefficient $\mu = 0.001,\ 0.1$ and 1. Total persistence is computed for both normal, Fn, and tangential, Ft, forces. The most obvious observation is that the transitions become increasingly smooth as μ increases, both for the pressure, and for the total persistence. For $\mu = 0.001$, the tangential forces are very noisy, however we should remember that these forces are very small in magnitude, since they are limited by the Coulomb threshold.

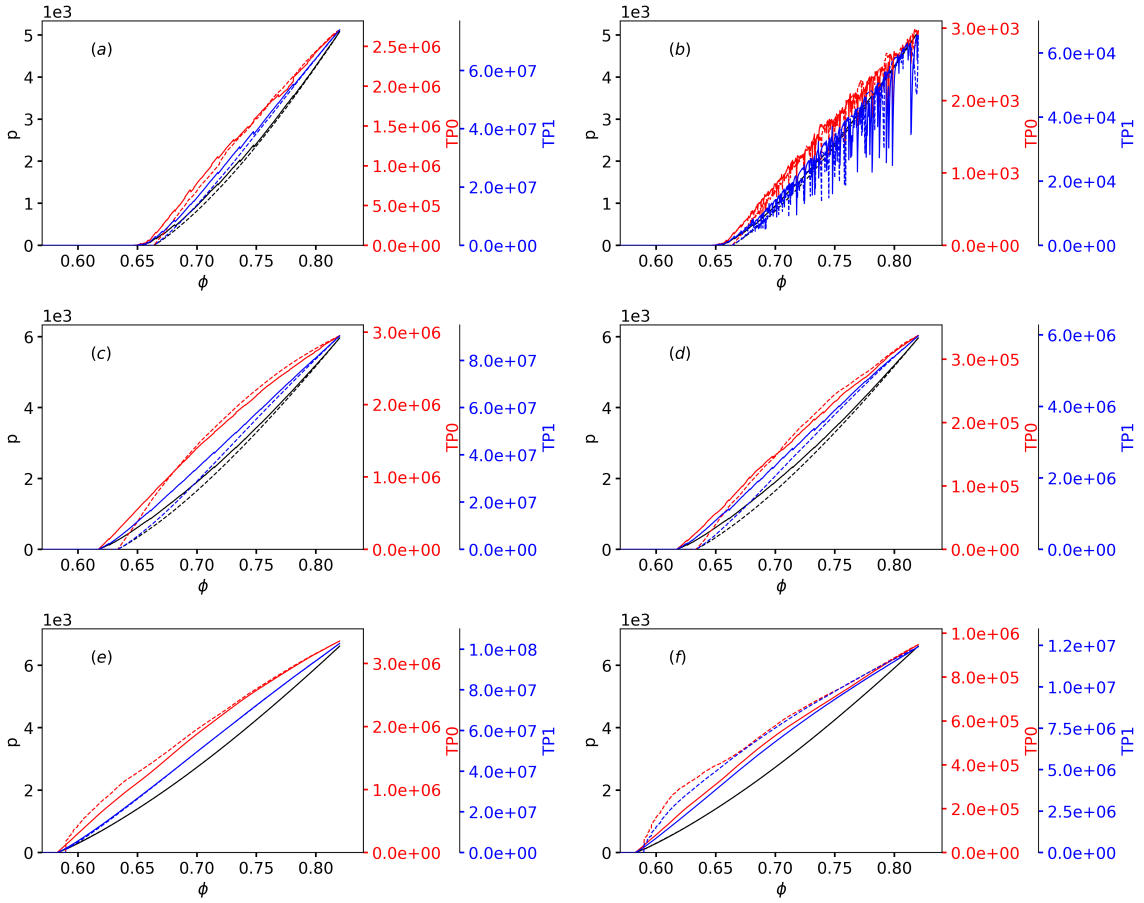

Figure 5.18 The pressure, TP0, and TP1 for μ=0.001: (a) Fn, (b) Ft; μ=0.1, (c) Fn, (d) Ft; μ=1, (e) Fn, (f) Ft. Loading branches are plotted by solid lines, and unloading ones by dashed lines. Note different vertical axes scales.

Next, we consider one of the transition events, so to illustrate the differences compared to the frictional results. For brevity, we focus here on $\mu = 0.1$ only, for both loading and unloading. Figure 5.19 shows the loading results for the similar range of volume fractions as in the corresponding figures showing frictionless results. Comparing

frictional and frictionless results, we note that if friction is present, the events are characterized by much smaller jumps in the corresponding quantities (such as pressure), and also they occur on a much faster time scales. The interpretation of this finding is that friction acts to quickly dissipate the energy associated with any of the transitions. Both normal and tangential forces show similar behavior.

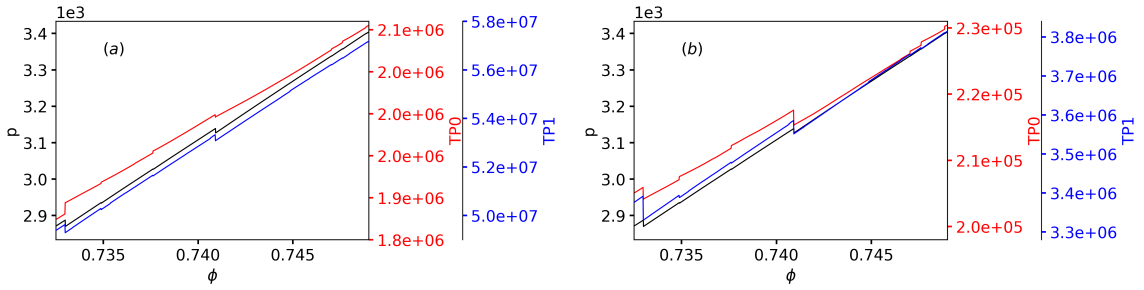

Figure 5.19 Zoom into the loading branch of μ=0.1, (a)TPs of Fn, (b) TPs of Ft.

Figure 5.20 shows the changes of E_k/E_p and of the PDs (measured by W2 distance) for the same range of volume fractions as in Figure 5.19. We note that any change of E_k/E_p is captured by W2 distance matrices; however, W2 β_1 distances also show changes that are not associated with any obvious change of E_k/E_p; this finding shows that in addition to the events that are characterized by particle rearrangements, there also ones that involve the change of force networks only, in particular of the structure of loops/cycles, without any rearrangment of the particles.

Figures 5.21 and 5.22 show the results for the unloading phase, with the main features of the results similar to the ones already discussed for loading.

5.6 Summary and Conclusion

In this chapter, we discuss the process of slow compression (loading) and decompression (unloading) for a three dimensional granular system. The main finding is that both loading and unloading proceed via a combination of reversible and irreversible processes, with the latter ones being associated with rapid and significant transitions. These transitions may be

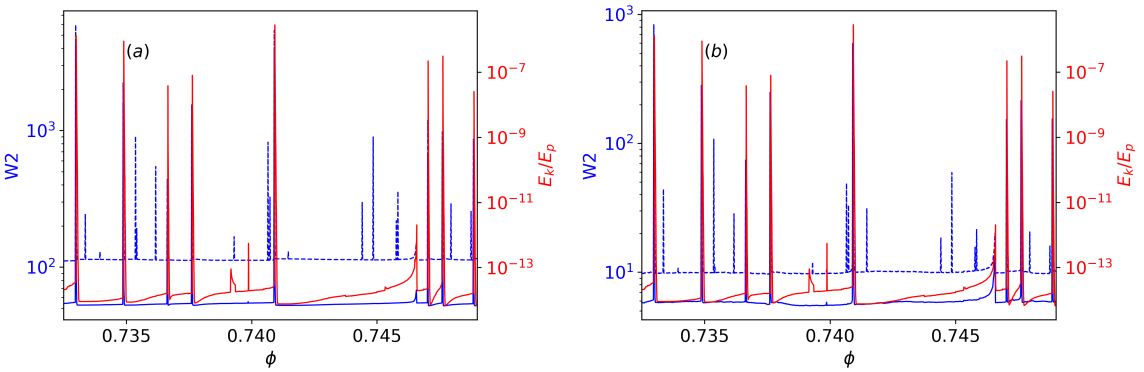

Figure 5.20 Loading branch of μ=0.1, (a) W2 of Fn, (b) W2 of Ft. Solid for β_0, dashed for β_1.

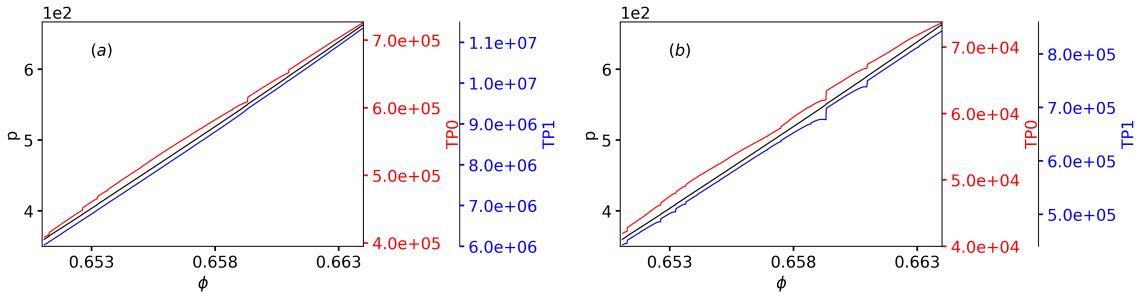

Figure 5.21 Unloading branch of μ=0.1, (a)TPs of Fn, (b) TPs of Ft.

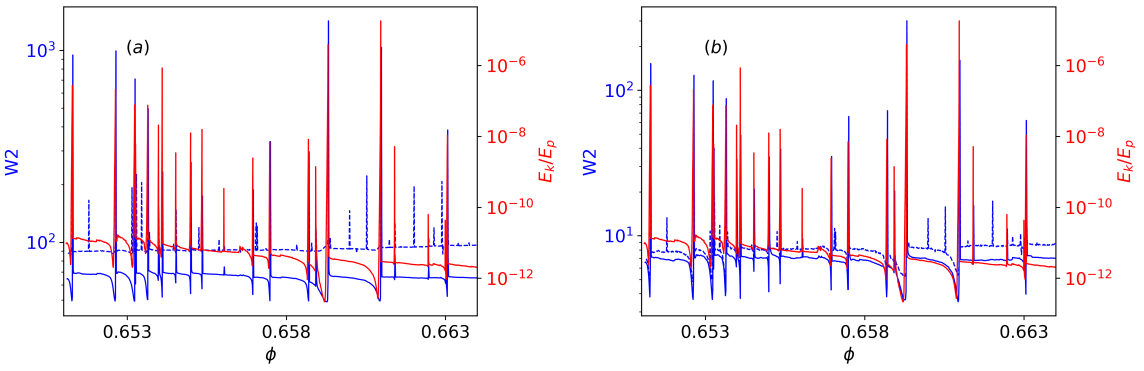

Figure 5.22 Unloading branch of μ=0.1, (a) W2 of Fn, (b) W2 of Ft. Solid for β_0, dashed for β_1.

associated with rearrangements of the particle contacts and associated particle dynamics, however we also find transitions that are associated with the changes in force networks only, without any obvious dynamics of the particles.

The analysis of the force networks is carried out using persistent homology, the technique that allows to quantify the evolution both during reversible and irreversible processes discussed above. While persistent homology allows for extraction of a number of features of the underlying force networks, in present work we focus mostly on the most condensed measure, total persistence, TP. This measure encodes the information about complex weighted three dimensional (3D) network into a single number. Even under such extreme information reduction, we find that TP provides insightful information about the underlying force network. In particular, we find that during the irreversible transitions, the changes of the total pressure are strongly correlated with the TP computed for the loops that spontaneously form in evolving force networks. This finding suggests that the force network loops play a significant role in determining the mechanical system properties.

Further insight regarding the evolving force networks can be obtained by comparing consecutive system configurations. Such a comparison is made meaningful by computing the differences between the persistence diagrams that describe the main features of the underlying network. The difference, known as Wasserstein distances, shows that the force network experience a significant change during the transitions discussed above, with the force networks differing before and after a transition. It should be emphasized that for obtaining such simple but insightful result, the data reduction provided by persistent homology method is crucial. This data reduction leads inevitably to an information loss, however we find that even under the most dramatic data compression, the emerging information still allows for reaching a relevant insight.

While the main part of this chapter focuses on loading and unloading of frictionless particles, we also discuss briefly frictional particles, characterized by a large range of friction coefficients. In the considered system, the main role of friction is to smooth

transitions observed for the frictionless case, leading to significantly smaller changes of system pressure, or of total persistence. In addition, transition events are much faster for frictional particles, compared to frictionless ones. The transitions are still followed by the changes of Wassestein distance, and in particular we observe transitions characterized only by changes in structure of the loops formed by the force network, without any underlying particle dynamics.

CHAPTER 6

SUMMARY AND CONCLUSION

In this work, we focus on the analysis and numerical simulations of intermittent dynamics of dense particulate systems, ranging from 2D stick-slip types of granular systems to 3D systems with intruders, and under compression and decompression.

In Chapter 2, we discussed the dynamics of the pullout of a spherical intruder initially buried at the bottom of a granular column. Analysis of the interparticle forces, using both classical and persistent homology, reveals the details of the failure process. The intruder and the granular particles are basically static before failure, but the force network goes through significant changes. The tangential forces between the particles increase as the applied force becomes larger, leading to a larger number of sliding contacts. The normal force between the particles evolves as well, and the force network based on the normal force becomes more structured, involving more loops and stronger forces between the particles, even when normalized by the mean. The changes in the force network are focused in particular on the strong forces when considering clusters of contacts, while the loops that form in a network are evolving at all considered levels of the interaction strength. By combining classical approaches and persistence homology for describing both statics and dynamics of a granular system, we have identified in this chapter precise and objective measures that can be used to describe a failure process in the considered system. We hope that both the methods and the results presented in this chapter will provide guidance for future research in this direction.

In Chapter 3, we focused on the experiments involving a slider moving on top of granular media of photo-elastic particles in two dimensions, which may vary from continuous motion to crackling, periodic motion, and stick-slip type of behavior. Using the tools of persistent homology, a clear correlation between the slider dynamics and

the response of the force network that spontaneously develop in the granular system. In particular, stick and slip regimes of the slider dynamics are well captured by the persistent homology measures. These results suggest that there is a potential for developing predictive capabilities by analyzing the response of the force network to an external perturbation. One open question is how precise should the information about the forces between the granular particles be so to allow for further development of this potential. We hope that our results set stage for this future work.

In Chapter 4, we discussed the stick-slip dynamics of dense granular system in 2D via discrete element simulations. We focused on the question of what type of information, static or dynamic, is needed to be able to predict an upcoming slip event. Static measures describe static properties of the system which are obtained from observing the state of the system at a given time, and dynamic measures which can be obtained by considering the system evolution information. We identified a set of dynamic measures that show promise in predicting avalanching type of behavior in the considered system. While our findings are based on the 2D simulation results, we hope that they will inspire future study that will be positioned to verify our findings in both three dimensions, and in experimental setups.

In Chapter 5, we investigated the process of slow compression and decompression for a three dimensional granular system. The evolution of the granular system is nontrivial, with smooth, continuous (de)compression periods interrupted by fast, irreversible transitions. These transitions may be associated with rearrangements of the particle contacts and associated particle dynamics.However, the transitions may be associated with the changes in force networks only, without any obvious dynamics of the particles. The analysis of the force network is carried out using persistence homology methods, that allow for extracting a number of features from the underlying force networks. The analysis shows that the evolution of pressure is strongly correlated with the evolution of the topological measures quantifying loops in the force networks. This finding suggests that the force network loops play a significant role in determining the mechanical system properties. We also briefly

considered frictional granular systems which are characterized by a large range of friction coefficients. In the considered systems, frictional effects are found to lead to smoother system evolution, decreasing the amplitude of the transition events, and their duration. In particular, we observed transitions characterized only by changes in the structure of the loops formed by the force network, without any underlying particle dynamics.

The overall conclusion of the presented work is that force networks in granular systems provide significant and important information about overall system properties, including macroscopic variables such as pressure, as well as regarding intermittency of the system response. To reach this conclusion, we have considered relatively coarse measures, such as total persistence, emerging from the analysis based on persistent homology. Still, a number of relevant insights has been obtained. We hope that the results presented in this work will serve as a basis for more elaborate and detailed analysis of force networks in particulate systems.

APPENDIX A

FORCE MODEL

Particles in simulations are either inelastic spheres in 3D or disks in 2D. The particles interact via normal and tangential forces including static friction. The particle-particle and particle-wall interactions include both normal and tangential components. In simulations, the linear force model is applied in 2D, and Hertzian force model is applied in 3D. This section applies to the simulations discussed in Chapter 4. In that chapter, only 2D systems and linear force model are considered; for completeness here we present the model for both 2D and 3D.

A.1 Linear Model

Let $\mathbf{F}^n_{L,ij}$ and $\mathbf{F}^t_{L,ij}$ be the force exerted on particle i from particle j in the normal and tangential directions in the linear force model. Therefore,

$$\mathbf{F}^n_{L,ij} = k_n x \mathbf{n} - \gamma_n \bar{m} \mathbf{v}^n_{ij}, \tag{A.1}$$

where $\mathbf{v}^n_{ij}$ is relative normal velocity, $\bar{m}$ is reduced mass, $\bar{m} = m_i m_j/(m_i + m_j)$, $\mathbf{n}$ is the normal direction pointing towards particle i from particle j, k_n is the spring constant in the normal direction, γ_n is the damping coefficient in the normal direction. Here, x is the overlap between the two contact particles, where

$$x = \frac{1}{2}(d_i + d_j) - r_{ij}. \tag{A.2}$$

Here, d is the particle diameter, r_{ij} is the distance between the centers of the two particles, where $r_{ij} = |\mathbf{r}_i - \mathbf{r}_j|$. The relative normal velocity $\mathbf{v}^n_{ij}$ between particle i and particle j can be calculated as

$$\mathbf{v}_{ij} = \mathbf{v}_i - \mathbf{v}_j - \frac{1}{2}(\omega_i + \omega_j) \times \mathbf{r}_{ij}, \tag{A.3}$$

$$\mathbf{v}_{ij}^n = (\mathbf{v}_{ij} \cdot \mathbf{n})\mathbf{n}. \tag{A.4}$$

For the tangential forces, we implement the commonly used Cundall-Strack model for static friction [47], where a tangential spring is introduced between particles for each new contact that forms at given time $t = t_0$ and is used to determine the tangential force during the contact of any two particles. Due to the relative motion of the particles, the tangential spring, ξ, evolves as

$$\xi = \int_{t_0}^{t} \mathbf{v}_{ij}^t(s)ds, \tag{A.5}$$

where the relative tangential velocity $\mathbf{v}_{ij}^t$ is calculated by

$$\mathbf{v}_{ij}^t = \mathbf{v}_{ij} - \mathbf{v}_{ij}^n. \tag{A.6}$$

The tangential direction is defined through the tangential velocity

$$t = \frac{\mathbf{v}_{ij}^t}{|\mathbf{v}_{ij}^t|}. \tag{A.7}$$

The contacts of particles can last for a few steps in Discrete Element Method (DEM) simulations. Therefore, we have to correct the direction of tangential spring which may be not remaining parallel to the current tangential direction.

$$\xi' = \xi - \mathbf{n}(\mathbf{n} \cdot \xi). \tag{A.8}$$

Hence, the test tangential force is obtained

$$\mathbf{F}_{L,ij}^{t*} = -k_t \xi' - \gamma_t \bar{m} \mathbf{v}_{ij}^t, \tag{A.9}$$

where k_t and γ_t are the spring constant and damping constant in the tangential direction. We compare the test force $\mathbf{F}_{ij}^{t*}$ with the Coulomb friction force, with the smaller one being the actual tangential force, that is

$$\mathbf{F}_{L,ij}^{t} = \min\left(\mu|\mathbf{F}_{L,ij}^{n}|, |\mathbf{F}_{L,ij}^{t*}|\right) \frac{\mathbf{F}_{L,ij}^{t*}}{|\mathbf{F}_{L,ij}^{t*}|}. \tag{A.10}$$

A.2 Hertzian Model

In Hertzian force model [58, 174], the normal force is

$$\mathbf{F}_{H}^{n} = \sqrt{\frac{d_i d_j}{d_i + d_j}}\sqrt{x}[k_n x\mathbf{n} - \gamma_n \bar{m}\mathbf{v}_{ij}^{n}]. \tag{A.11}$$

The test tangential force is

$$\mathbf{F}_{H}^{t*} = \sqrt{\frac{d_i d_j}{d_i + d_j}}\sqrt{x}[-k_t \xi' - \gamma_t \bar{m}\mathbf{v}_{ij}^{t}]. \tag{A.12}$$

Hence, the tangential force is

$$\mathbf{F}_{H}^{t} = \min\left(\mu|\mathbf{F}_{H}^{n}|, |\mathbf{F}_{H}^{t*}|\right) \frac{\mathbf{F}_{H}^{t*}}{|\mathbf{F}_{H}^{t*}|.} \tag{A.13}$$

APPENDIX B

NON-DIMENSIONALIZATION

This section applies to the scaling of simulations discussed in Chapter 4. In DEM simulations, we use 2500 bidisperse system particles, with 25% of large particles and 75% small particles. The small particle's diameter is $d = 1.27$ cm, and the large particle diameter is approximately $1.59d/1.27$ [58, 102]. In the following discussion, the small particle is referred as the basic particle upon which all the scaling parameters are based. The top wall is made of 40 basic particles which are spaced $1.5d$ away from each other so to decrease the slip of system particles relative to the wall, and the bottom wall is made of 60 basic particles that are closely arranged. Discrete element simulations are carried out using non-dimensional version of the model, formulated by using the scales as in Table B.1. After non-dimensionalization, the physical units are converted into real units, in terms of the diameter, collision time, and mass of the basic particle.

Table B.1 Basic Non-dimensionalization Units

Scaling	Symbol
Length	basic particle diameter, d
Time	basic particles collision time, τ_c
Mass	basic particle mass, m

The definition of particle diameter and particle mass is straightforward. However, the definition of collision time τ_c of two particles is defined differently under different force models. τ_c [124] is defined as :

$$\tau_c = I(\beta) \times (1+0.5\beta)^{\frac{1}{2+\beta}} \left(\bar{m} \frac{3(1-\sigma^2)}{Y d^{1-\beta}} \right)^{\frac{1}{2+\beta}} v_0^{\frac{-\beta}{2+\beta}}, \tag{B.1}$$

where

$$I(\beta) = \frac{\sqrt{\pi}\Gamma(\frac{1}{2+\beta})}{(1+\beta/2)\Gamma(\frac{4+\beta}{4+2\beta})}, \tag{B.2}$$

$\bar{m} = m_i m_j / m_i + m_j$ is the reduced particle mass, m_i and m_j is the mass of the two colliding particles, Y is the Young's modulus, σ is the Possion coefficient, and v_0 is the particle's relative velocity.

Under the linear force model assumption, $\beta = 0$, $I(\beta) = \pi$, hence Equation B.1 for linear collision time τ_c^l of two basic particles in 2D can be simplified as the following

$$\tau_c^l = \pi \times \sqrt{m\frac{3(1-\sigma^2)}{2Yd}}. \tag{B.3}$$

where $\sigma = 0.5$, $Y = 0.7$ MPa, $d = 1.27$ cm, $m = 1.32$ g (the thickness of disks is assumed to be 1 cm). These material properties are used in [102]. Hence, the resulting binary collision time for the time scale is $\tau_c^l = 1.25 \times 10^{-3}$ s.

The Hertzian force model is applied in 3D simulations only. We find the collision time of two identical spherical particles by setting the velocity of a particle to be $v_0 = 1.5$ cm/s, which is the same as the speed of the pulling spring, and the other one with zero velocity. Hence, the resulting collision time $\tau_c^h = 5.55 \times 10^{-3}$ s, which can be derived using $\beta = 0.5$, $I(\beta) = 2.94$, $\sigma = 0.5$, $Y = 0.7$ MPa, $m = 1.15$ g, $d = 1.27$ cm [102], and the relatively velocity $v_0 = 1.5$ cm/s in Equation B.1.

The normal spring constant k_n is related to the material properties, and in the linear model is defined as [58]

$$k_n^l = \frac{m}{2}\left(\frac{\pi}{\tau_c^l}\right)^2 = \frac{Yd}{3(1-\sigma^2)}. \tag{B.4}$$

In Hertzian model,

$$k_n^h = \frac{2Y}{3(1-\sigma^2).} \tag{B.5}$$

In both models, the tangential spring constant is given by $k_t = 6k_n/7$ [74].

The linear damping coefficient γ_n^l is obtained using the coefficient of restitution, $e = 0.5$, which is defined as the ratio of the speed of a particle after a collision v_f to its speed before the collision v_0, i.e.,

$$e = \frac{v_f}{v_0}.$$

Therefore, in linear damping coefficient [99],

$$\gamma_n^l = -\frac{2\ln e}{\tau_c^l} \tag{B.6}$$

In Hertzian model, we derive the normal damping coefficient γ_n^h which corresponds to the coefficient of restitution $e = 0.5$ by carrying out a numerical experiment. We initialize head-on collisions of two identical particles with the same initial relative velocity $v_0 = 1.5$ cm/s, but with various damping coefficients, and then use the value which gives the desired value of e. For both linear and Hertzian force, the tangential damping coefficient is set $\gamma_t = \gamma_n$[58].

The interaction between system particles and walls are handled differently for the top and bottom wall. Considering a basic particle colliding with the bottom wall, since the bottom wall is fixed, and therefore we consider that it has infinite mass. The top wall, on the other hand, is treated as having a mass equal to $40m$.

Table B.2 shows the scaling factors used to convert the discussed parameters into dimensionless units. In the following discussion, all parameters are in dimensionless units, which are scaled by the basic units in Table B.1.

In 2D simulations, spring constant of the pulling spring is $1/400$ of the normal spring constant of the particles, the speed of the spring $v_s = 1.5 \times 10^{-3}$, and the pressure applied on the top wall is $p = 0.02$, which is assumed here to be force/length. The value of pressure and the spring velocity are selected so that the system can exhibit stick-slip behavior. In 3D simulations, spring constant of the pulling spring is $1/400$ of the normal spring constant of the particles, the $v_s = 6.55 \times 10^{-3}$ under Hertzian model, whose corresponding physical

Table B.2 Scaling Parameters

Parameter	Scaling factor
Y	$\frac{m}{d \cdot \tau_c^2}$
k_n^l, k_t^l(linear)	$\frac{m}{(\tau_c^l)^2}$
γ_n^l, γ_t^l (linear)	$\frac{1}{\tau_c^l}$
k_n^h, k_t^h(Hertz)	$\frac{m}{d \cdot (\tau_c^h)^2}$
γ_n^h, γ_t^h (Hertz)	$\frac{1}{d \cdot \tau_c^h}$

value is 1.5 cm/s as well. The external pressure, $p = 2.0$ (force/area) is applied to ensure that the system exhibits stick-slip behaviors.

The frictional coefficient between system particles is $\mu_s = 0.7$, and the coefficient between system particles and wall particles is $\mu_w = 2.0$, which resembles a sticky wall and reduces the relative velocity difference between the wall and the system particles.

APPENDIX C

DEM SIMULATION TECHNIQUES

The code for the Discrete Element Method (DEM) simulations of stick-slip behavior discussed in Chapter 4, based on a predictor-corrector algorithm, is written in FORTRAN 90 and it is implemented in a way that resembles object-oriented programming style. The DEM code is set up into several modules and functions. ***.F90** denotes any FORTRAN 90 subroutine or function code used in the simulation.

makefile.config: Simulation specification parameters are set here, including the status of simulation whether it restarted from an earlier condition, the dimension of the simulation (in 2D or 3D), and force model selection (linear force model or Hertzian force model).

Parameters.F90: Particle physical parameters and scaling parameters are defined and assigned.

Initialization.F90: Initialize the geometry setting of the stick-slip system, particles' translational and angular velocities.

UpdateBounary.F90: Update the spring position, and apply the constant pressure on the top wall. Since the area of the top wall and its mass is constant, it is equivalent to applying a constant acceleration on top wall, which will be added later to wall particle in **MakeForce.F90**.

Predictor.F90: Particle's position **x0**, translational velocity **x1**, translational accelerration **x2**, angular related quantities $\mathbf{x1_{rot}}$, and $\mathbf{x2_{rot}}$ are updated by using the current values of these quantities based on Taylor expansion. Note, for computation efficiency, $\mathbf{x1_{rot}}$ is defined as $d \cdot d\theta/dt$, where d is particle's diameter, $d\theta/dt$ is particle's angular velocity.

Verlet.F90: Track and update the list of neighboring particles of each particle, reducing the computation cost for searching contacts in simulation. **Verlet.F90** builds on

top of **CellRoutines.F90** which divides the whole system into smaller subdomains based on the particle positions. Since the simulation time step is small, when searching possible contacts, only the particles in neighboring cells need to be searched.

MakeForce.F90: Calculation of the contact force and torque between particles, using the predicted value after **Predictor.F90**, and add all the forces and torques on every particle.

Corrector.F90: Correct particle's translational and angular quantities based on the forces and torques calculated from **MakeForce.F90**.

APPENDIX D

SUPPLEMENTARY MATERIAL FOR STICK-SLIP RESULTS

D.1 Additional Dynamic Measure Analysis

Here we present some additional results related to the material presented in Chapter 4.

Figure D.1 shows the evolution of system particles' velocity profile by showing the heat maps (a) and the average particle velocity (b) for the event shown in Figure 4.2. In Figure D.1, we divide the system particles into 10×10 blocks based on the x, y coordinates (approximately 25 particles in each block), and the magnitude of average velocity of particles in each blocks is calculated, as indicated by color. In part a, the x-axis and y-axis indicate the x and y coordinates of the system, and the color in each block indicates the value of the average velocity. In part b, the mean of the velocity of the blocks that have the same y coordinate is plotted against the y coordinate. $\Delta t = 0$ is when the slip begins. The dynamics of the heat maps in Figure D.1 shows that the velocity profile of the system particles remains constant most of the time. Only a small change in the velocity profile occurs at $\Delta t = -18$, which suggests there may be some particle motion relative to the others in the system, highlighted by the bright green color in part a. However, the event is transient.

Figures D.2 and D.3 show snapshots of the animation of the evolution of differential normal or tangential force networks (defined by Equation 4.1) for the event shown in Figure 4.2, with a cutoff value 5×10^{-4} to show only relatively large values. In Figure D.2 , a clear structure starts to form around $\Delta t = -18$, and we are able to see some relatively strong differential normal force at $\Delta t = -15$, and the network continues to percolate through the system at $\Delta t = -12$. As pointed out in Figure D.1, although at $\Delta t = -15$ and $\Delta t = -12$ there existed no relative particle movements, we could still see the percolating differential normal force. Similarly, Figure D.3 shows the differential tangential force networks with

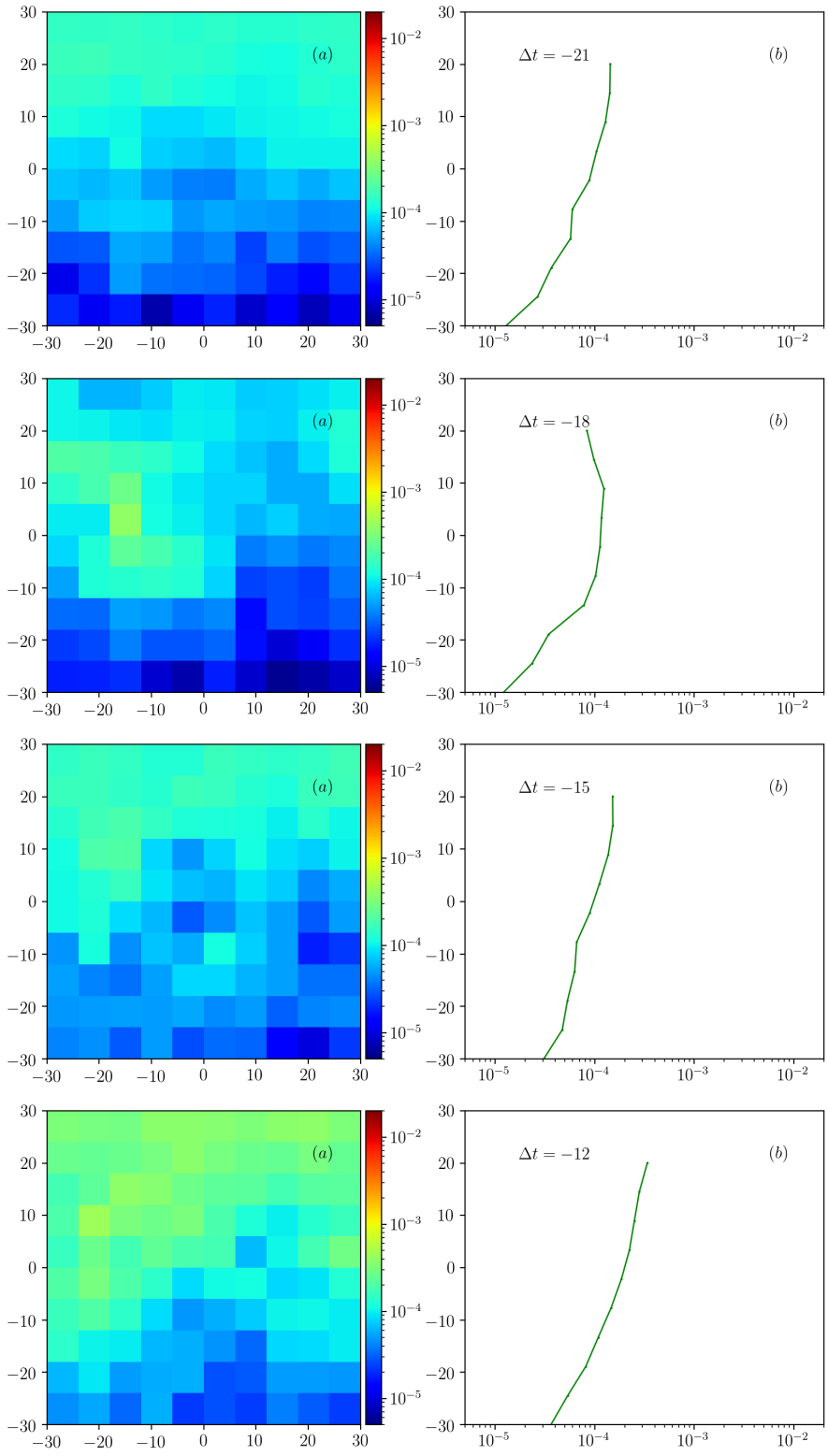

Figure D.1 (a): the evolution of system particle velocity heat map from $\Delta t = -21$ to $\Delta t = -12$ for the event in Figure 4.2, where the color indicates the mean of system particle speed in each block (The domain is divided into 10×10 blocks based on the x, y coordinates). (b): the average velocity of the blocks that have the same y coordinates plotted against y coordinates.

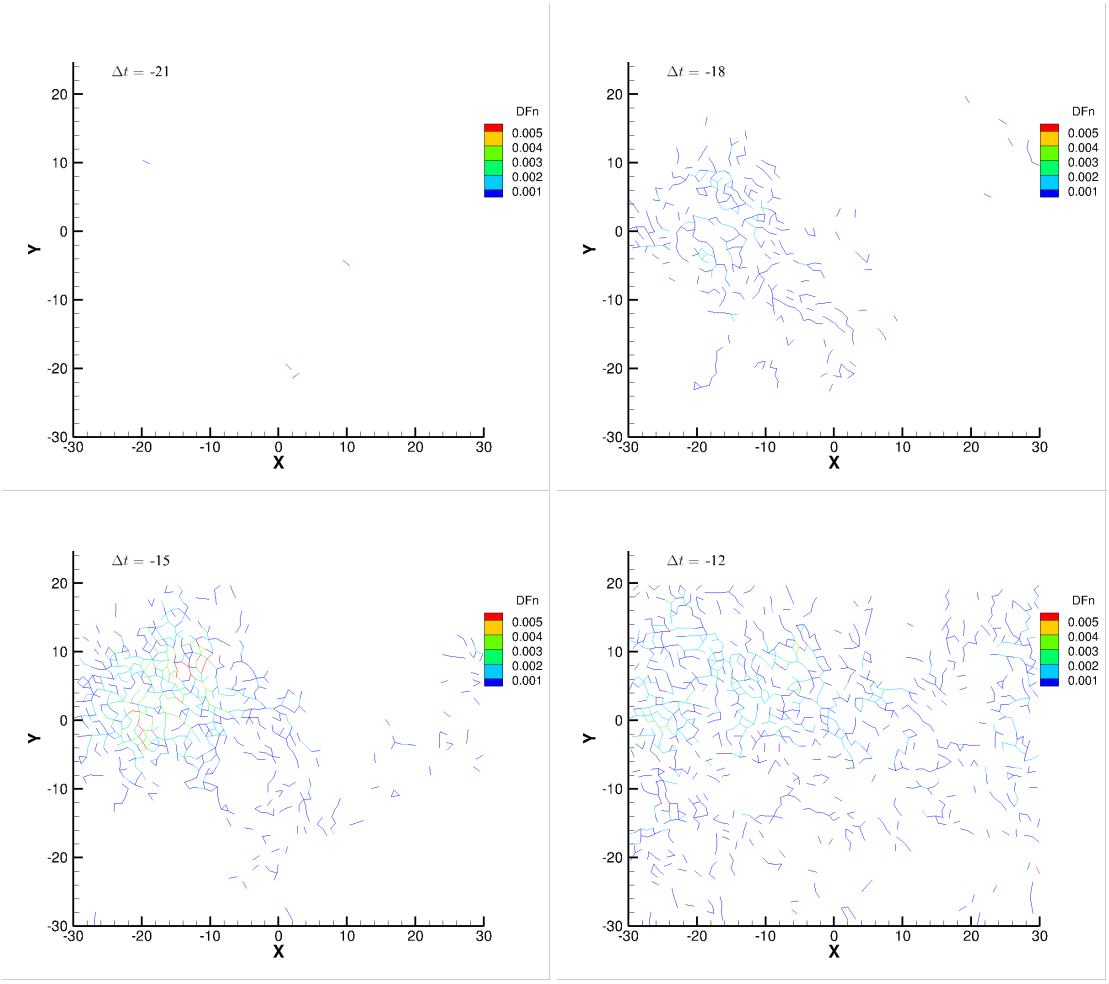

Figure D.2 The evolution of differential normal force networks for the event in Figure 4.2, with the cutoff value 5×10^{-4} to focus on the strong forces.

the same cutoff value, where the formation of differential tangential force networks is coupled with differential normal force networks, but it is much smaller in magnitude.

In Chapter 4, we only focus on the percolating differential normal contact force. In Figure D.4, the pre-slip percolating normal, tangential, and total contact force are investigated, for both horizontally and vertically; Figure D.5 shows the derivative of the percolating forces before slips. Figures D.4 and D.5 show that there is no much difference in using differential normal and total contact force for percolation, and the information carried by the horizontal percolation seems to provide more predictive power than the vertical one.

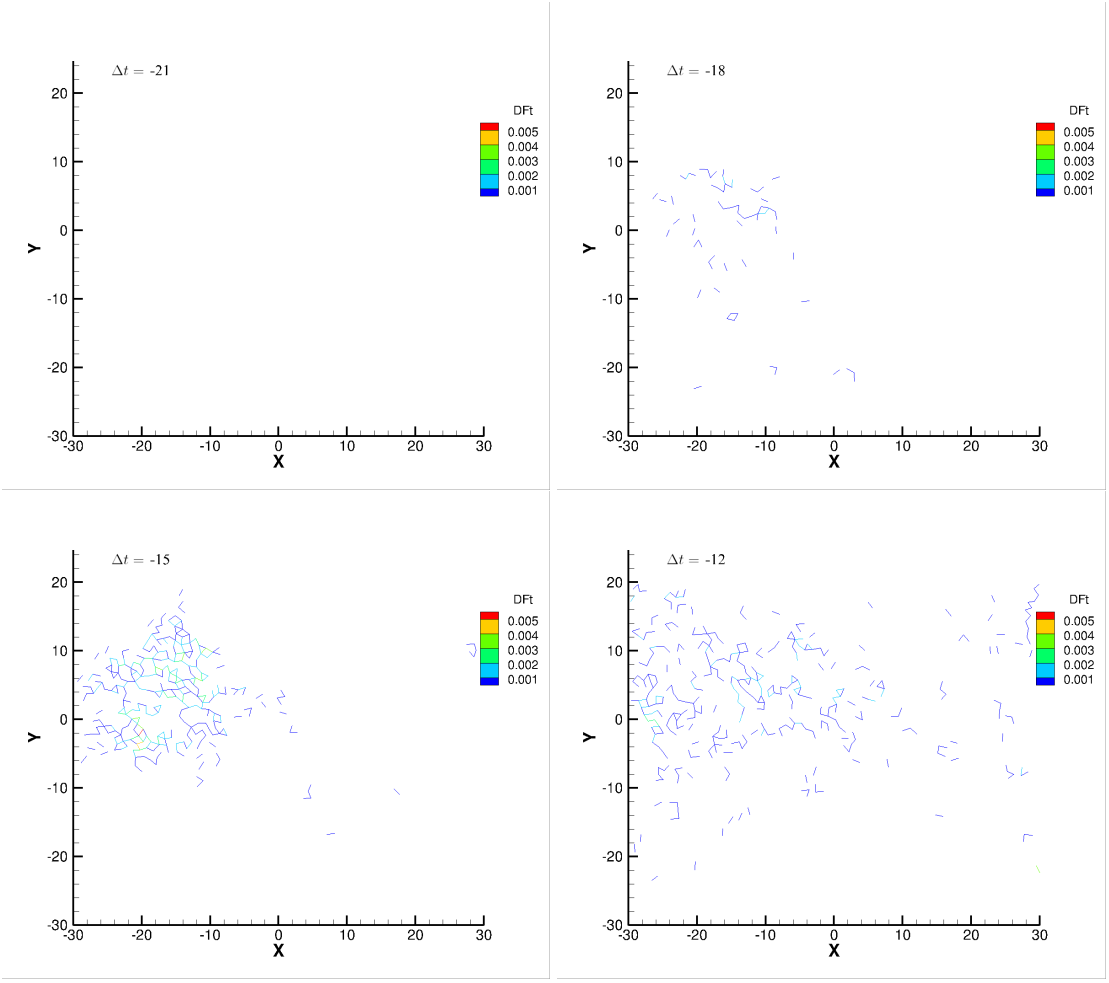

Figure D.3 The evolution of differential tangential force networks for the event in Figure 4.2, with the cutoff value 5×10^{-4}.

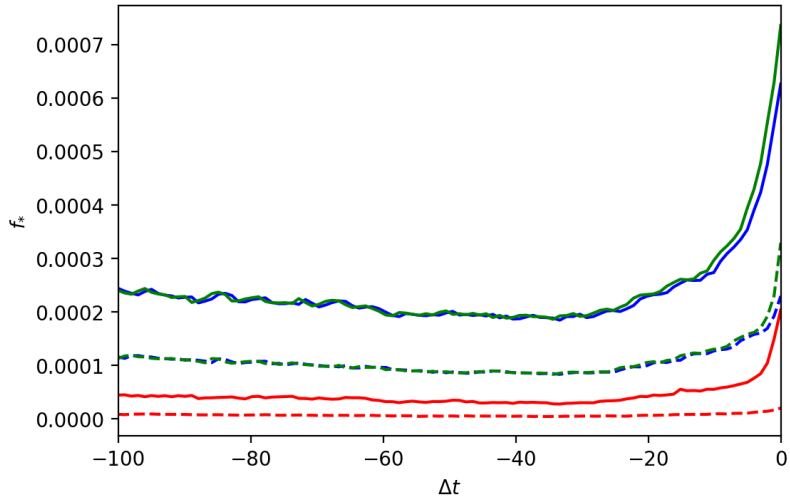

Figure D.4 The pre-slip percolating forces: normal (blue), tangential (red), and total (green). The solid lines show left-right percolation and dashed top-bottom.

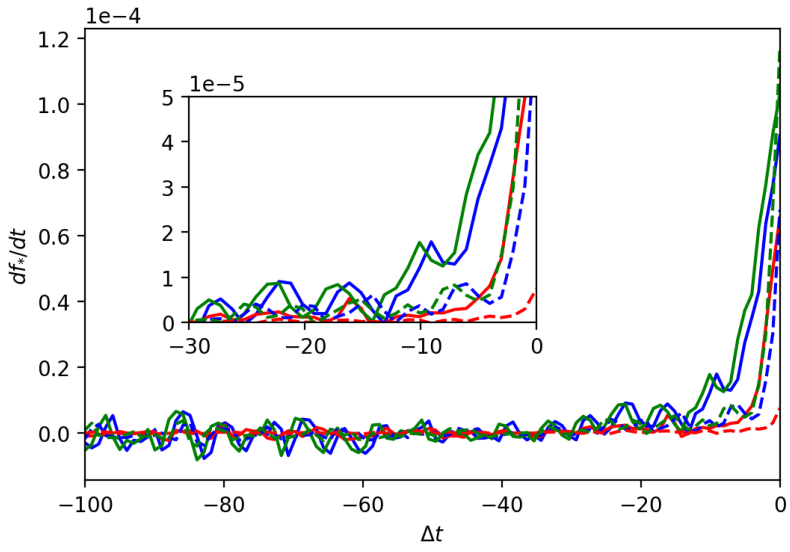

Figure D.5 The derivatives of pre-slip percolating forces, following the same color/style format as in Figure D.4.

D.2 Slip Events Statistics

Figures D.6 and D.7 shows the statistics of slip size and slip duration. Here the slip size is measured in the basic particle diameter d, and the slip duration is in δt, where $\delta t = 10\tau_c$. Figure D.6 shows that there exist two peaks, one peak from small slip sizes and one from relatively larger sizes. Such finding is also presented in [54]. In Figure D.7, the slip duration is plotted against slip size.

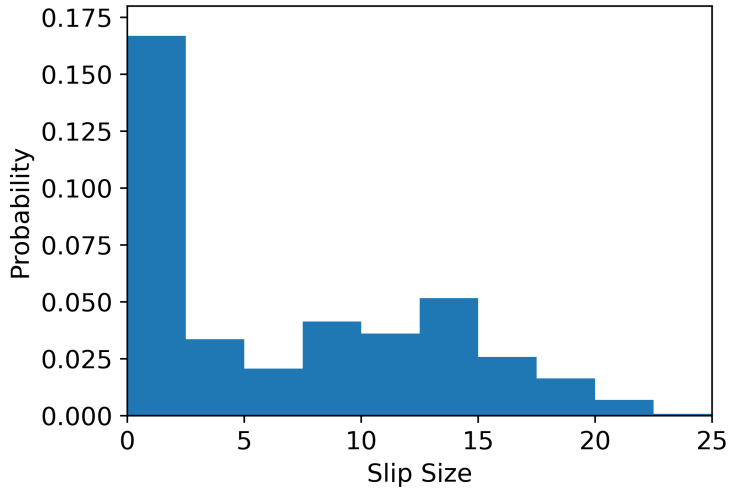

Figure D.6 Histogram of slip size, where the slip size is defined as the distance of the top wall traveled after the slip.

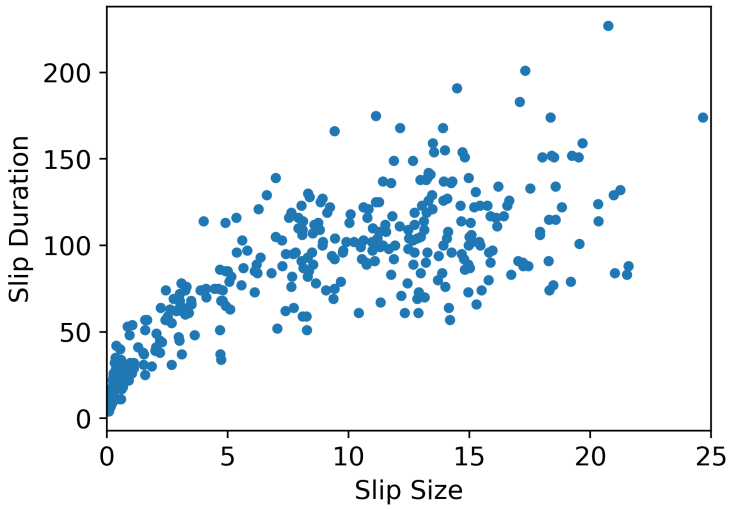

Figure D.7 The y-axis is the slip duration, which is measured in units of δt, the x-axis indicates the corresponding slip size.

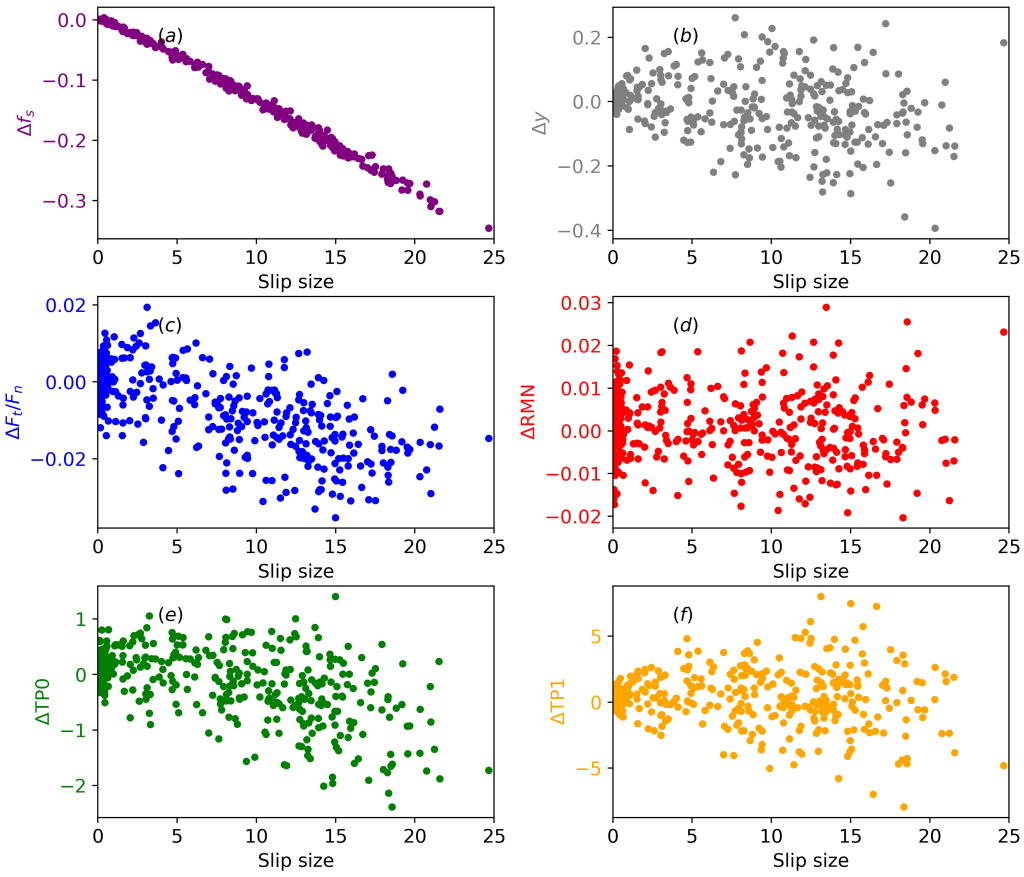

Figure D.8 The difference of the static measures between the start and the end of slip events (end - start) is plotted against the corresponding slip size. (a) spring force, f_s, (b) y position of the top wall, (c) the ratio of Ft/Fn, (d) the ratio of mobile to nonmobile contacts, RMN, (e) TP0, (f) TP1.

In Figure D.8, we measure the difference of static measures between the end and the start of the slip events, for example $\Delta f_x = f_x(end) - f_x(start)$. Some measures show relatively clear relations between the difference and slip size, such as spring force Δf_s, $\Delta F_t/F_n$, and ΔTP0, while some do not.

Furthermore, we investigate the relation between pre-slip static measures and the slip size. In Figure D.9, we categorize all the slip events into 4 categories based on the slip size, i.e., 0-2, 2-6, 6-14, and above 14. The pre-slip static measures are averaged over the events in each category. Figure D.8 indicates the slip events are well-separated in some

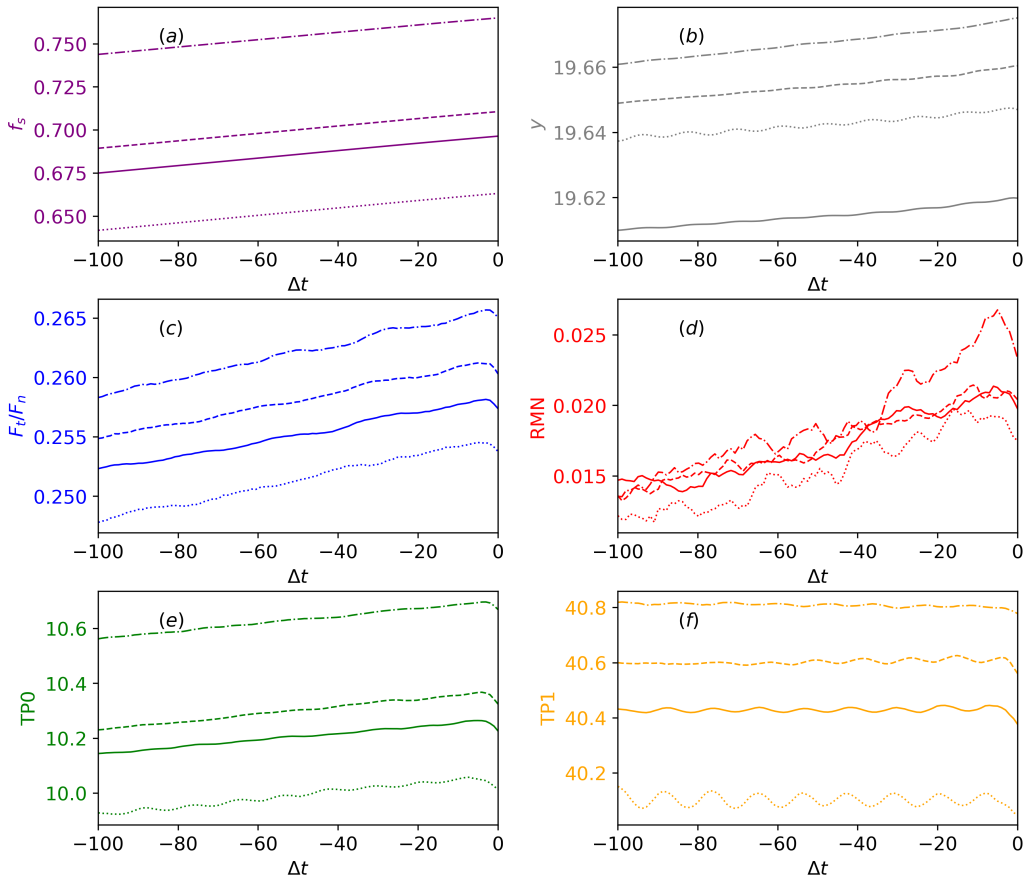

Figure D.9 The average value of static measures before slips averaged over different slip sizes, the solid lines are for slip size between 0 and 2, the dotted lines for slip size between 2 and 6, the dashed lines for between 6 and 14, and the dash-dotted for slip sizes greater than 14. (a) spring force, f_s, (b) y position of the top wall, (c) the ratio of F_t/F_n, (d) the ratio of mobile to non-mobile contacts, RMN, (e) TP0, (f) TP1. The time axis is in units of δt.

static measures, except RMN. However, the difference in the separation is not significant, as we could see that the difference is approximately 1%-3% of its value.

Similarly, we apply the same investigation to pre-slip dynamic measures as well. Figure D.10 indicates a similar finding as in Figure D.9 that the dynamic measures are not separated by the slip size.

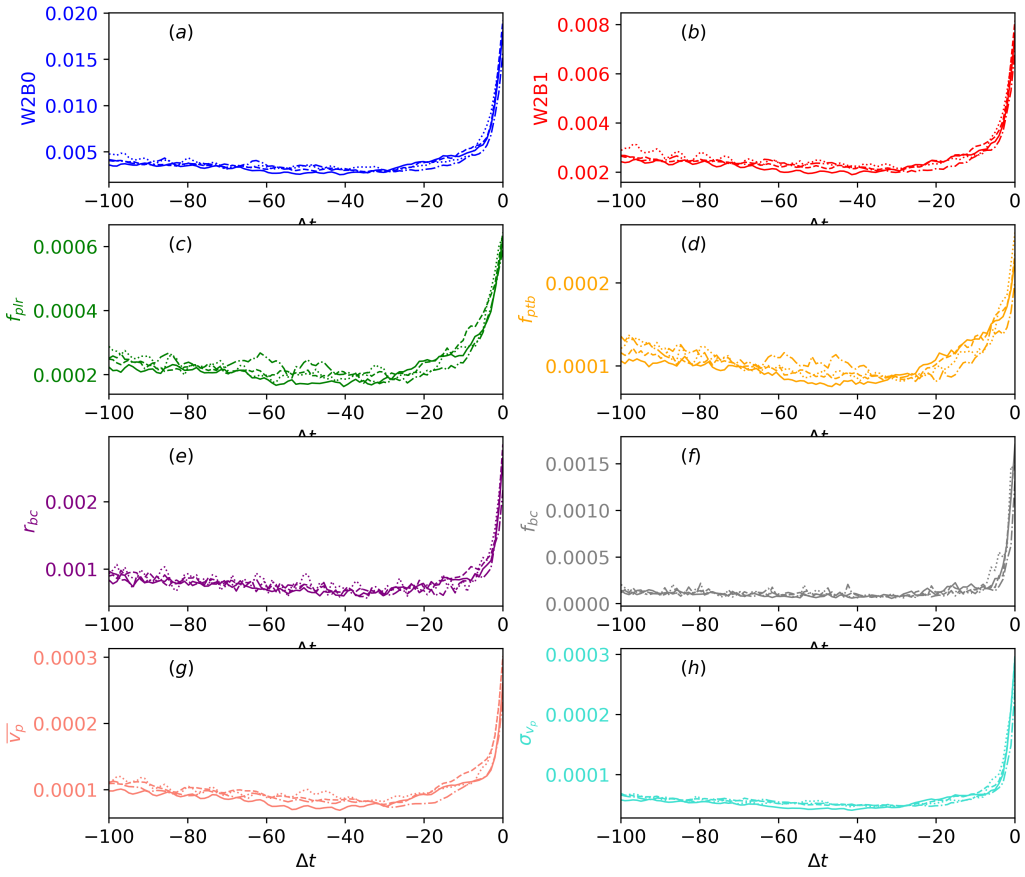

Figure D.10 The average value of dynamic measures before slips averaged over different slip sizes, with the line patterns as in Figure D.9. (a) W2B0, (b) W2B1, (c) the percolating differential normal force horizontally, f_{plr}, (d) the percolating differential normal force vertically, f_{ptb}, (e) the ratio of broken contacts to total contacts, r_{bc}, (f) the average broken normal force, f_{bc}, (g) the mean of system particle speed, $\bar{v}_p$, (h) the standard deviation of system particle speed, s_{v_p}.

APPENDIX E

SUPPLEMENTARY RESULTS FOR COMPRESSION STUDY

This section provides additional persistence analysis of frictionless events in Chapter 5.

E.1 Generators and Lifespans

The number of generators (G) of PD is defined as the number of data points in a PD, and the average lifespan of PD is the mean of lifespans of the generators. Figures E.1 - E.6 show G and LS for the three loading events and three unloading events in Chapter 5. For β_0, G decreases and LS increases after the event during loading, which suggests the force networks are forming into stronger force networks; G increases and LS decreases during unloading (from high volume fraction to low volume fraction), which suggests the force networks become weaker. For β_1, G can increase or decrease, and LS tends to move in the opposite direction of G during loading; for unloading, G and LS behave similarly as in loading.

The presented results do not seem show a clear trend, and it is at this point not clear what are the common features describing the changes in force networks during the events. Further research, perhaps including more detailed analysis of persistence diagrams is needed for this purpose.

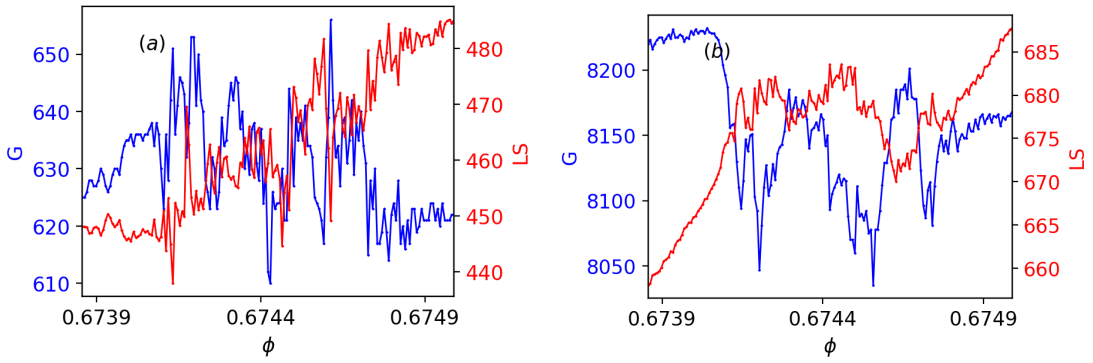

Figure E.1 Number of generators, G, and their corresponding lifespan, LS, of Event L1 for (a) β_0, (b) β_1.

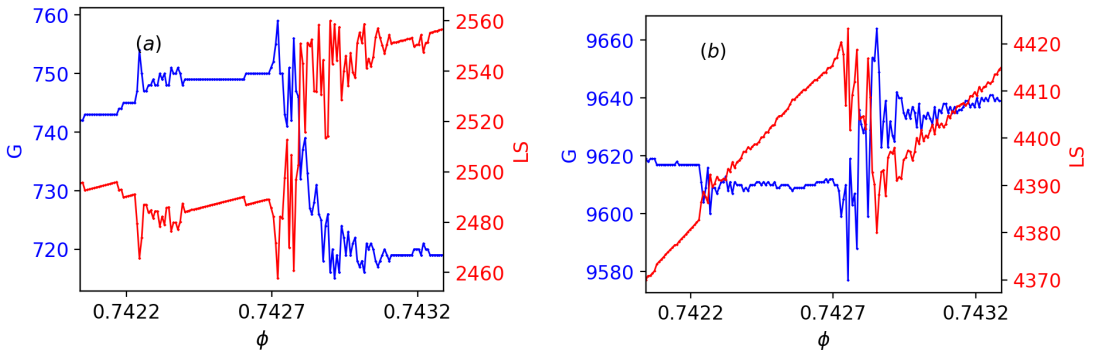

Figure E.2 Number of generators, G, and their corresponding lifespan, LS, of Event L2 for (a) β_0, (b) β_1.

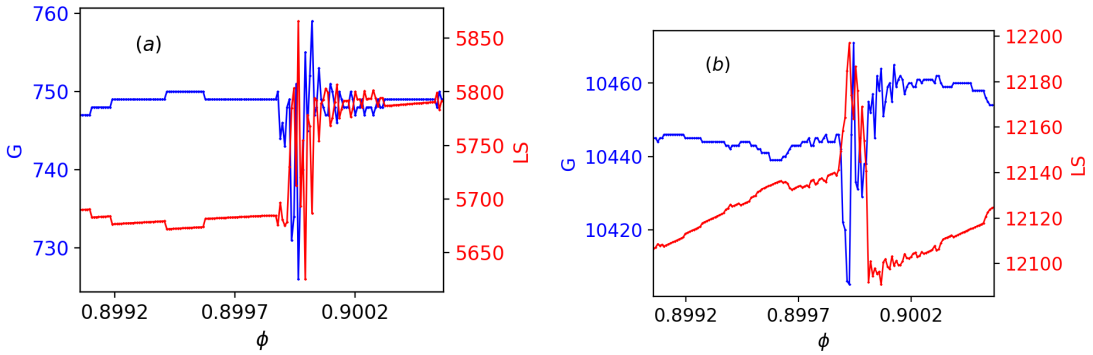

Figure E.3 Number of generators, G, and their corresponding lifespan, LS, of Event L3 for (a) β_0, (b) β_1.

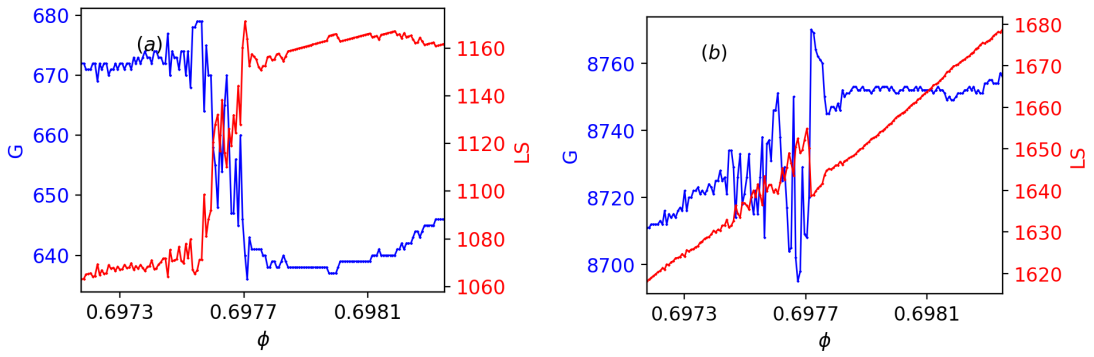

Figure E.4 Number of generators, G, and their corresponding lifespan, LS, of Event UL1 for (a) β_0, (b) β_1.

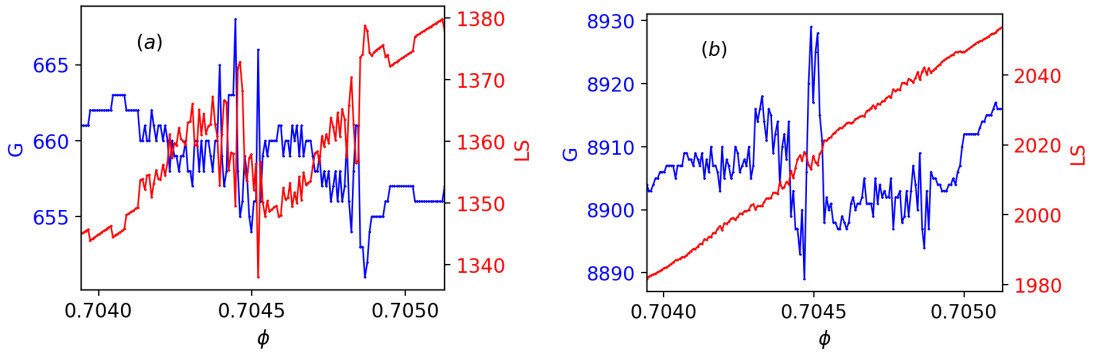

Figure E.5 Number of generators, G, and their corresponding lifespan, LS, of Event UL2 for (a) β_0, (b) β_1.

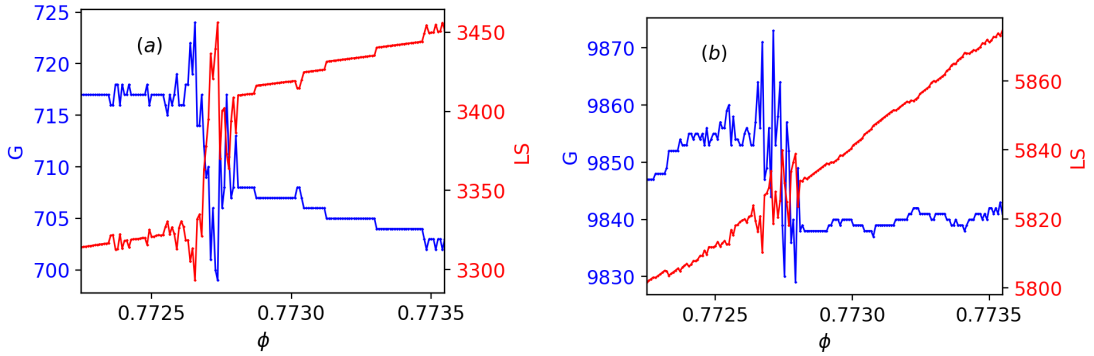

Figure E.6 Number of generators, G, and their corresponding lifespan, LS, of Event UL3 for (a) β_0, (b) β_1.

REFERENCES

[1] GUDHI: Geometry understanding in higher dimensions. `http://gudhi.inria.fr`, Inria, Sacley, France, accessed on 2012-04-12.

[2] A. Abed Zadeh, J. Barés, and R. P. Behringer. Crackling to periodic dynamics in granular media. *Physical Review E*, 99(4):040901, 2019.

[3] A Abed Zadeh, J. Barés, T. A. Brzinski, K. E. Daniels, J. Dijksman, N. Docquier, H. O. Everitt, J. E. Kollmer, O. Lantsoght, D. Wang, et al. Enlightening force chains: a review of photoelasticimetry in granular matter. *Granular Matter*, 21(4), 2019.

[4] A. Abed Zadeh, J Barés, J. E. S. Socolar, and R. P. Behringer. Seismicity in sheared granular matter. *Physical Review E*, 99:052902, 2019.

[5] A. Alenzi, M. Marinack, C. F. Higgs, and J. J. McCarthy. DEM validation using an annular shear cell. *Powder Technology*, 248:131–142, 2013.

[6] F. Alonso-Marroquin and H. J. Herrmann. Calculation of the incremental stress-strain relation of a polygonal packing. *Physical Review E*, 66, 2002.

[7] F. Alonso-Marroquin, S. Luding, H. J. Herrmann, and I. Vardoulakis. Role of anisotropy in the elastoplastic response of a polygonal packing. *Physical Review E*, 71(5):051304, 2005.

[8] E. Ando, J. Dijkstra, E. Roubin, C. Dano, and E. Boller. A peek into the origin of creep in sand. *Granular Matter*, 21:11, 2019.

[9] B. Andreotti, Y. Forterre, and O. Pouliquen. *Granular Media: Between Fluid and Solid*. Amsterdam, the Netherlands: Cambridge, 2013.

[10] S. Ardanza-Trevijano, I. Zuriguel, R. Arévalo, and D. Maza. Topological analysis of tapped granular media using persistent homology. *Physical Review E*, 89:052212, 2014.

[11] R. Arévalo, L. A. Pugnaloni, I. Zuriguel, and D. Maza. Contact network topology in tapped granular media. *Physical Review E*, 87:022203, 2013.

[12] R. Arévalo, I. Zuriguel, and D. Maza. Topology of the force network in jamming transition of an isotropically compressed granular packing. *Physical Review E*, 81:041302, 2010.

[13] S. Athani and P. Rognon. Mobility in granular materials upon cyclic loading. *Granular Matter*, 20:67, 2019.

[14] E. Azéma and F. Radjaï. Internal structure of inertial granular flows. *Physical Review Letters*, 112:078001, 2014.

[15] J. Baker, F. Guillard, B. Marks, and I. Einav. X-ray rheography uncovers planar granular flows despite non-planar walls. *Nature Communications*, 9(1):5119, 2018.

[16] M. M. Bandi, P. Das, O. Gendelman, H. G. E. Hentschel, and I. Procaccia. Universal scaling laws for shear induced dilation in frictional granular media. *Granular Matter*, 21(3):40, 2019.

[17] J. Barés, N. Brodu, H. Zheng, and J. A. Dijksman. Transparent experiments: releasing data from mechanical tests on three dimensional hydrogel sphere packings. *Granular Matter*, 22(1):21, 2020.

[18] J. Barés, A. Dubois, L. Hattali, D. Dalmas, and D. Bonamy. Aftershock sequences and seismic-like organization of acoustic events produced by a single propagating crack. *Nature Communications*, 9(1):1253, 2018.

[19] J. Barés, M. L. Hattali, D. Dalmas, and D. Bonamy. Fluctuations of global energy release and crackling in nominally brittle heterogeneous fracture. *Physical Review Letters*, 113:264301, 2014.

[20] T. Barker, D. Schaeffer, M. Shearer, and N. Gray. Well-posed continuum equations for granular flow with compressibility and $\mu(i)$-rheology. *Proceedings of the Royal Society A*, 473(2201):20160846, 2017.

[21] D. S. Bassett, E. T. Owens, K. E. Daniels, and M. A. Porter. Influence of network topology on sound propagation in granular materials. *Physical Review E*, 86:041306, 2012.

[22] D. S. Bassett, E. T. Owens, M. A. Porter, M. L. Manning, and K. E. Daniels. Extraction of force-chain network architecture in granular materials using community detection. *Soft Matter*, 11:2731–2744, 2015.

[23] A. S. Baumgarten and K. Kamrin. A general fluid-sediment mixture model and constitutive theory validated in many flow regimes. *Journal of Fluid Mechanics*, 861:721–764, 2019.

[24] R. P. Behringer, D. Bi, B. Chakraborty, S. Henkes, and R. R. Hartley. Why do granular materials stiffen with shear rate? Test of novel stress-based statistics. *Physical Review Letters*, 101(26), 2008.

[25] R. P. Behringer and B. Chakraborty. The physics of jamming for granular materials: a review. *Reports on Progress in Physics*, 82:012601, 2018.

[26] R. P. Behringer, K. E. Daniels, T. S. Majmudar, and M. Sperl. Fluctuations, correlations and transitions in granular materials: statistical mechanics for a non-conventional system. *Philosophical Transactions of the Royal Society A: Mathematical, Physical and Engineering Sciences*, 366(1865), 2008.

[27] H. Di Benedetto and F. Darve. Comparison of rheological laws in rotational kinematics. *Journal de Mecanique Theorique et Appliquee*, 2(5):769, 1983.

[28] N. Berger, E. Azema, J.-F. Douce, and F. Radjai. Scaling behaviour of cohesive granular flows. *Europhysics Letters*, 112:64004, 2015.

[29] L. Berthier and G. Biroli. Theoretical perspective on the glass transition and amorphous materials. *Reviews of Modern Physics*, 83:587–645, 2011.

[30] T. Bertrand, R. P. Behringer, B. Chakraborty, C. S. O'Hern, and M. D. Shattuck. Protocol dependence of the jamming transition. *Physical Review E*, 93, 2016.

[31] D. Bi and B. Chakraborty. Rheology of granular materials: dynamics in a stress landscape. *Philosophical Transactions of the Royal Society of London A: Mathematical, Physical and Engineering Sciences*, 367(1909):5073–5090, 2009.

[32] D. Bi, J. Zhang, B. Chakraborty, and R. P. Behringer. Jamming by shear. *Nature*, 480(7377):355–358, 2011.

[33] L. Bo, R. Mari, C. Song, and H. A. Makse. Cavity method for force transmission in jammed disordered packings of hard particles. *Soft Matter*, 10:7379–7392, 2014.

[34] J. Boschan, S. Luding, and B. P. Tighe. Jamming and irreversibility. *Granular Matter*, 21(3):58, 2019.

[35] N. Brodu, J. A. Dijksman, and R. P. Behringer. Spanning the scales of granular materials through microscopic force imaging. *Nature Communications*, 6:6361, 2015.

[36] J. Brujić, C. Song, P. Wang, C. Briscoe, G. Marty, and H. A. Makse. Measuring the coordination number and entropy of a 3D jammed emulsion packing by confocal microscopy. *Physical Review Letters*, 98(24):248001, 2007.

[37] J. Brujić, P. Wang, C. Song, D. L. Johnson, O. Sindt, and H. A. Makse. Granular dynamics in compaction and stress relaxation. *Physical Review Letters*, 95(12), 2005.

[38] B. Cambou, F. Darve, and F. Nicot. Particle methods in geomechanics. *International Journal for Numerical and Analytical Methods in Geomechanics*, 43:831–832, 2019.

[39] M. E. Cates, J. P. Wittmer, J.-P. Bouchaud, and P. Claudin. Jamming, force chains and fragile matter. *Physical Review Letters*, 81:1841, 1998.

[40] M. E. Cates, J. P. Wittmer, J.-P. Bouchaud, and P. Claudin. Jamming and static stress transmission in granular materials. *Chaos: An Interdisciplinary Journal of Nonlinear Science*, 9(3):511–522, 1999.

[41] C. Cheng, A. Abed Zadeh, and L. Kondic. Correlating the force network evolution and dynamics in slider experiments. (to appear in Powders & Grains, 2021). arXiv:2101.07218.

[42] X. Cheng, S. Xiao, A. S. Cao, and M. Hou. A review and analysis of granular shear experiments under low effective stress conditions. *Granular Matter*, 21(4):104, 2019.

[43] M. Pica Ciamarra and A. Coniglio. Jamming at Zero Temperature, Zero Friction, and Finite Applied Shear Stress. *Physical Review Letters*, 103(23):235701, 2009.

[44] M. Pica Ciamarra, L. de Arcangelis, E. Lippiello, and C. Godano. Granular failure: the origin of earthquakes? *International Journal of Modern Physics B*, 23:5374–5382, 2009.

[45] A. H. Clark, L. Kondic, and R. P. Behringer. Particle scale dynamics in granular impact. *Physical Review Letters*, 109:238302, 2012.

[46] B. Cui, G. Ruocco, and A. Zaccone. Theory of elastic constants of athermal amorphous solids with internal stresses. *Granular Matter*, 21(3):69, 2019.

[47] P. A. Cundall and O. D. L. Strack. A discrete numerical model for granular assemblies. *Géotechnique*, 29:47–65, 1979.

[48] J. Cyranka, S. Harker, and R. Levanger. TDA Persistence Explorer. `https://github.com/rachellevanger/tda-persistence-explorer`, accessed 2021-04-12.

[49] K. E. Daniels and R. P. Behringer. Characterization of a freezing/melting transition in a vibrated and sheared granular medium. *Journal of Statistical Mechanics: Theory and Experiment*, 2006(07):P07018, 2006.

[50] F. Darve. Liquefaction phenomenon of granular materials and constitutive stability. *International Journal of Engineering and Computer Science*, 13(7):5–28, 1996.

[51] F. Darve, E. Flavigny, and M. Meghachou. Yield surfaces and principle of superposition: revisit through incrementally non-linear constitutive relations. *International Journal of Plasticity*, 11(8):927–945, 1995.

[52] E. G. Daub and J. M. Carlson. Friction, Fracture, and Earthquakes. *Annual Review of Condensed Matter Physics*, 1:397–418, 2010.

[53] J. Davidsen and G. Kwiatek. Earthquake interevent time distribution for induced micro-, nano-, and picoseismicity. *Physical Review Letters*, 110(6):068501, 2013.

[54] L. de Arcangelis, M. Pica Ciamarra, E. Lippiello, and C. Godano. Micromechanics and statistics of slipping events in a granular seismic fault model. *Journal of Physics: Conference Series*, 319:012001, 2011.

[55] L. de Arcangelis, C. Godano, J. R. Grasso, and E. Lippiello. Statistical physics approach to earthquake occurrence and forecasting. *Physics Reports*, 628:1 – 91, 2016.

[56] D. V. Denisov, K. A. Lőrincz, W. J. Wright, T. C. Hufnagel, A. Nawano, X. Gu, J. T. Uhl, K. A. Dahmen, and P. Schall. Universal slip dynamics in metallic glasses and granular matter–linking frictional weakening with inertial effects. *Scientific Reports*, 7:43376, 2017.

[57] A. Di Renzo and F. P. Di Maio. Comparison of contact-force models for the simulation of collisions in dem-based granular flow codes. *Chemical Engineering Science*, 59:525–541, 2004.

[58] J. A. Dijksman, L. Kovalcinova, J. Ren, R. P. Behringer, M. Kramár, K. Mischaikow, and L. Kondic. Characterizing granular networks using topological metrics. *Physical Review E*, 97:042903, 2018.

[59] I. Einav. The unification of hypo-plastic and elasto-plastic theories. *International Journal of Solids and Structures*, 49(11-12):1305–1315, 2012.

[60] I. Einav and M. Liu. Hydrodynamic derivation of the work input to fully and partially saturated soils. *Journal of the Mechanics and Physics of Solids*, 110:205–217, 2018.

[61] I. Einav and A. M. Puzrin. Pressure-dependent elasticity and energy conservation in elastoplastic models for soils. *Journal of Geotechnical and Geoenvironmental Engineering*, 130(1):81–92, 2004.

[62] M. L. Falk and J. S. Langer. Deformation and failure of amorphous, solidlike materials. *Annual Review of Condensed Matter Physics*, 2:353–373, 2011.

[63] S. Farhadi and R. P. Behringer. Dynamics of sheared ellipses and circular disks: effects of particle shape. *Physical Review Letters*, 112(14):148301, 2014.

[64] B. T. Fasy, J. Kim, F. Lecci, C. Maria, D. L. Millman, and V. Rouvreau. TDA: Statistical Tools for Topological Data Analysis. `https://CRAN.R-project.org/package=TDA`, Inria, Sacley, France, accessed on 2012-04-12.

[65] B. Ferdowsi, M. Griffa, R. A. Guyer, P. A. Johnson, C. Marone, and J. Carmeliet. Three-dimensional discrete element modeling of triggered slip in sheared granular media. *Physical Review E*, 89:042204, 2014.

[66] T. Furuta, S. Kumar, K. A. Reddy, H. Niiya, and H. Katsuragi. Packing-dependent granular friction exerted on a rod withdrawn from a granular layer: the role of shear jamming. *New Journal of Physics*, 21(2):023001, 2019.

[67] M. Gameiro, A. Singh, L. Kondic, K. Mischaikow, and J. F. Morris. Interaction network analysis in shear thickening suspensions. *Physical Review Fluids*, 5:034307, 2020.

[68] J. Geng, D. Howell, E. Longhi, R. P. Behringer, G. Reydellet, L. Vanel, E. Clément, and S. Luding. Footprints in sand : The response of a granular material to local perturbations. *Physical Review Letters*, 87, 2001.

[69] K. Giannis, C. Schilde, J. H. Finke, A. Kwade, M. A. Celigueta, K. Taghizadeh, and S. Luding. Stress based multi-contact model for discrete-element simulations. *Granular Matter*, 23(2):1–14, 2021.

[70] C. Giusti, L. Papadopoulos, E. T. Owens, K. E. Daniels, and D. S. Bassett. Topological and geometric measurements of force-chain structure. *Physical Review E*, 94:032909, 2016.

[71] J. D. Goddard. Continuum modeling of granular media. *Applied Mechanics Reviews*, 66(5):050801, 2014.

[72] J. D. Goddard and K. Kamrin. Dissipation potentials from elastic collapse. *Proceedings of the Royal Society A*, 475(2226):20190144, 2019.

[73] J. D. Goddard and J. Lee. Regularization by compressibility of the $\mu(i)$ model for dense granular flow. *Physics of Fluids*, 30:073302, 2018.

[74] C. Goldenberg and I. Goldhirsch. Friction enhances elasticity in granular solids. *Nature*, 435:188, 2005.

[75] F. Göncü, O. Durán, and S. Luding. Jamming in frictionless packings of spheres: determination of the critical volume fraction. In *AIP Conference Proceedings "Powders and Grains 2009"*, volume 1145, pages 531–534, 2009.

[76] N. Hadda, L. Sibille, F. Nicot, and F. Darve. Failure in granular media from an energy viewpoint. *Granular Matter*, 18:50, 2016.

[77] J. P. Hansen and I. R. McDonald. *Theory of Simple Liquids*. San Diego, CA: Academic Press, 1986.

[78] X. He, W. Wu, G. Cai, J. Qi, J. R. Kim, D. Zhang, and M. Jiang. Work-energy analysis of granular assemblies validates and calibrates a constitutive model. *Granular Matter*, 22(1):28, 2020.

[79] D. L. Henann and K. Kamrin. A predictive, size-dependent continuum model for dense granular flows. *Proceedings of the National Academy of Sciences*, 110(17):6730–6735, 2013.

[80] S. Henkes and B. Chakraborty. Statistical mechanics framework for static granular matter. *Physical Review E*, 79:61301, 2009.

[81] S. Henkes, C. S. O'Hern, and B. Chakraborty. Entropy and temperature of a static granular assembly: an ab initio approach. *Physical Review Letters*, 99(3):038002, 2007.

[82] M. Herrera, S. McCarthy, S. Slotterback, W. Losert, and M. Girvan. Path to fracture in granular flows: Dynamics of contact networks. *Physical Review E*, 83:061303, 2011.

[83] Y. Hiraoka, T. Nakamura, A. Hirata, E. G. Escolar, K. Matsue, and Y. Nishiura. Hierarchical structures of amorphous solids characterized by persistent homology. *Proceedings of the National Academy of Sciences*, 113(26):7035–7040, 2016.

[84] A. Hirata, L. J. Kang, T. Fujita, B. Klumov, K. Matsue, M. Kotani, A. R. Yavari, and M. W. Chen. Geometric frustration of icosahedron in metallic glasses. *Science*, 341(6144):376–379, 2013.

[85] S. R. Hostler and C. E. Brennen. Pressure wave propagation in a granular bed. *Physical Review E*, 72:031303, 2005.

[86] P. S. Iliev, E. Giacomazzi, F. K. Wittel, M. Mendoza, A. Haselbacher, and H. J. Herrmann. Behavior of confined granular beds under cyclic thermal loading. *Granular Matter*, 21(3):59, 2019.

[87] O. I. Imole, M. Paulick, V. Magnanimo, M. Morgeneyer, B. E. Montes, M. Ramaioli, A. Kwade, and S. Luding. Slow stress relaxation behavior of cohesive powders. *Powder Technology*, 293:82–93, 2016.

[88] H. M. Jaeger, S. R. Nagel, and R. P. Behringer. Granular solids, liquids, and gases. *Reviews of Modern Physics*, 68(4):1259–1273, 1996.

[89] P. Jalali, Y. Zhao, and J. E. S. Socolar. Static and dynamic features of granular material failure due to upward pulling of a buried sphere by a slowly increasing force. *Soft Matter*, 17(10):2832—2839, 2021.

[90] Y. Jiang and M. Liu. Applying GSH to a wide range of experiments in granular media. *The European Physical Journal E*, 38(3):15, 2015.

[91] Y. Jiang and M. Liu. Why granular media are thermal, and quite normal, after all. *The European Physical Journal E*, 40(1):10, 2017.

[92] K. L. Johnson. *Contact mechanics*. New York, NY: Cambridge University Press, 1987.

[93] T. Kacynksi, K. M. Mischaikow, and M. Mrozek. *Computational Homology*. New York, NY: Springer, 2004.

[94] K. Kamrin and J. D. Goddard. Symmetry relations in viscoplastic drag laws. *Proceedings of the Royal Society A*, 470(2172):20140434, 2014.

[95] H. Katsuragi and D. J. Durian. Unified force law for granular impact cratering. *Nature Physics*, 3:420–423, 2007.

[96] C. Kloss, C. Goniva, A. Hager, S. Amberger, and S. Pirker. Models, algroithms and validation for opensource dem and cfd-dem. *Progress in Computational Fluid Dynamics*, 12:140–152, 2012.

[97] J. Koivisto, M. Korhonen, M. Alava, C. P. Ortiz, D. J. Durian, and A. Puisto. Friction controls even submerged granular flows. *Soft Matter*, 13:7657–7664, 2017.

[98] J. E. Kollmer and K. E. Daniels. Betweenness centrality as predictor for forces in granular packings. *Soft Matter*, 15:1793–1798, 2019.

[99] L. Kondic. Dynamics of spherical particles on a surface: Collision-induced sliding and other effects. *Physical Review E*, 60:751–770, 1999.

[100] L. Kondic, A. Goullet, C. S. O'Hern, M. Kramar, K. Mischaikow, and R. P. Behringer. Topology of force networks in compressed granular media. *Europhysics Letters*, 97:54001, 2012.

[101] L. Kondic, M. Kramár, L. A. Pugnaloni, C. M. Carlevaro, and K. Mischaikow. Structure of force networks in tapped particulate systems of disks and pentagons. ii. persistence analysis. *Physical Review E*, 93:062903, 2016.

[102] L. Kovalcinova, A. Goullet, and L. Kondic. Scaling properties of force networks for compressed particulate systems. *Physical Review E*, 93:042903, 2016.

[103] M. Kramár, A. Goullet, L. Kondic, and K. Mischaikow. Persistence properties of compressed granular matter. *Physical Review E*, 87:042207, 2013.

[104] M. Kramár, A. Goullet, L. Kondic, and K. Mischaikow. Evolution of force networks in dense particulate media. *Physical Review E*, 90:052203, 2014.

[105] M. Kramár, A. Goullet, L. Kondic, and K. Mischaikow. Quantifying force networks in particulate systems. *Physica D: Nonlinear Phenomena*, 283:37 – 55, 2014.

[106] M. Kramár, R. Levanger, J. Tithof, B. Suri, M. Xu, M. Paul, M. F. Schatz, and K. Mischaikow. Analysis of kolmogorov flow and rayleigh–bénard convection using persistent homology. *Physica D: Nonlinear Phenomena*, 334:82 – 98, 2016.

[107] H. Kruggel-Emden, S. Rickelt, S. Wirtz, and V. Scherer. A study on the validity of the multi-sphere discrete element method. *Powder Technology*, 188(2):153–165, 2008.

[108] N. P. Kruyt, O. Millet, and F. Nicot. Macroscopic strains in granular materials accounting for grain rotations. *Granular Matter*, 16:933–944, 2014.

[109] M. R. Kuhn and A. Daouadij. Stress fluctuations during monotonic loading of dense three-dimensional granular materials. *Granular Matter*, 21:10, 2019.

[110] N. Kumar. *Micro-Macro and jamming transition in granular materials*. PhD thesis, Universiteit Twente, Enschede, Netherlands, 2014.

[111] N. Kumar and S. Luding. Memory of jamming-multiscale models for soft and granular matter. *Granular Matter*, 18(3):1–21, 2016.

[112] N. Kumar, S. Luding, and V. Magnanimo. Incremental stress and microstructural response of granular soils under undrained axisymmetric deformation. In Kenichi Soga, Krishna Kumar, Giovanna Biscontin, and Matthew Kuo, editors, *Geomechanics from Micro to Macro*, pages 115–121, Reggio Calabria (Italy), 14-18 September 2009, 2014. CRC Press/Balkema.

[113] M. Lätzel, S. Luding, H. J. Herrmann, D. W. Howell, and R. P. Behringer. Comparing simulation and experiment of a 2D granular Couette shear device. *European Physical Journal E*, 11(4):325–333, 2003.

[114] Y. Li, Y. Xu, and C. Thornton. A comparison of discrete element simulations and experiments for 'sandpiles' composed of spherical particles. *Powder Technology*, 160(3):219–228, 2005.

[115] A. J. Liu and S. R. Nagel (Eds). *Jamming and Rheology*. New York, NY: Taylor & Francis, 2001.

[116] A. J. Liu and S. R. Nagel. Jamming is just not cool any more. *Nature*, 396:21, 1998.

[117] A. J. Liu and S. R. Nagel. The jamming transition and the marginally jammed solid. *Annual Review of Condensed Matter Physics*, 1:347–369, 2010.

[118] C. Liu, E. E. Ferrero, F. Puosi, J.-L. Barrat, and K. Martens. Driving rate dependence of avalanche statistics and shapes at the yielding transition. *Physical Review Letters*, 116(6):065501, 2016.

[119] A. A. Long, D. V. Denisov, P. Schall, T. C. Hufnagel, X. Gu, W. J. Wright, and K. A. Dahmen. From critical behavior to catastrophic runaways: comparing sheared granular materials with bulk metallic glasses. *Granular Matter*, 21(4):99, 2019.

[120] S. Luding. Introduction to discete element methods: Basics of contact force models and how to perform the micro-marco transition to continuum theory. *European Journal of Environmental and Civil Engineering*, 12(7-8):785–826, 2008.

[121] S. Luding. Towards dense, realistic granular media in 2D. *Nonlinearity*, 22(12):R101–R146, 2009.

[122] S. Luding. Granular matter: So much for the jamming point. *Nature*, 12(6):531–532, 2016.

[123] S. Luding and F. Alonso-Marroqu'in. The critical-state yield stress (termination locus) of adhesive powders from a single numerical experiment. *Granular Matter*, 13:109–119, 2011.

[124] S. Luding, E. Clément, A. Blumen, J. Rajchenbach, and J. Duran. Anomalous energy dissipation in molecular dynamics simulations of grains: The "detachment effect". *Physical Review E*, 50:4113, 1994.

[125] S. Luding and E. S. Perdahciouglu. A Local Constitutive Model with Anisotropy for Various Homogeneous 2D Biaxial Deformation Modes. *Chemie Ingenieur Technik*, 83(5):672–688, 2011.

[126] S. Mahajan, M. Tennenbaum, S. N. Pathak, D. Baxter, X. Fan, P. Padilla, C. Anderson, A. Fernandez-Nieves, and M. Pica Ciamarra. Reverse janssen effect in narrow granular columns. *Physical Review Letters*, 124:128002, 2020.

[127] T. S. Majmudar, M. Sperl, S. Luding, and R. P. Behringer. Jamming Transition in Granular Systems. *Physical Review Letters*, 98(5):058001, 2007.

[128] M. L. Manning and A. J. Liu. Vibrational modes identify soft spots in a sheared disordered packing. *Physical Review Letters*, 107(10):108302, 2011.

[129] R. Mari, R. Seto, J. F. Morris, and M. M. Denn. Discontinuous shear thickening in brownian suspensions by dynamic simulation. *Proceedings of the National Academy of Sciences*, 112(50):15326–15330, 2015.

[130] A. Merkel and S. Luding. Enhanced micropolar model for wave propagation in ordered granular materials. *International Journal of Solids and Structures*, 106-107:91–105, 2017.

[131] G. D. R. MiDi. On dense granular flows. *European Physical Journal E*, 14(4):341–365, 2004.

[132] B. Miller, C. O'Hern, and R. P. Behringer. Stress Fluctuations for Continuously Sheared Granular Materials. *Physical Review Letters*, 77:3110–3113, 1996.

[133] R. D. Mindlin and H. Deresiewicz. Elastic spheres in contact under varying oblique forces. *Journal of Applied Mechanics*, 20:327–340, 1953.

[134] K. A. Murphy, K. A. Dahmen, and H. M. Jaeger. Transforming mesoscale granular plasticity through particle shape. *Physical Review X*, 9(1):011014, 2019.

[135] B. Nadler, F. Guillard, and I. Einav. Kinematic model of transient shape-induced anisotropy in dense granular flow. *Physical Review Letters*, 120(19):198003, 2018.

[136] A. Nicolas, E. E. Ferrero, K. Martens, and J.-L. Barrat. Deformation and flow of amorphous solids: An updated review of mesoscale elastoplastic models. *Reviews of Modern Physics*, 90(4):045006, 2018.

[137] F. Nicot, A. Daouadji, F. Laouafa, and F. Darve. Second-order work, kinetic energy and diffuse failure in granular materials. *Granular Matter*, 13:19, 2011.

[138] C. S. O'Hern, Langer, and S. R. Nagel. Force distributions near jamming and glass transitions. *Physical Review Letters*, 86:111–114, 2001.

[139] C. S. O'Hern, A. J. Liu, and S. R. Nagel. Effective temperatures in driven systems: static versus time-dependent relations. *Physical Review Letters*, 93(16), 2004.

[140] S. Ostojic, E. Somfai, and B. Nienhuis. Scale invariance and universality of force networks in static granular matter. *Nature*, 439:828–830, 2006.

[141] L. Papadopoulos, M. A Porter, K. E. Daniels, and D. S. Bassett. Network analysis of particles and grains. *Journal of Complex Networks*, 6:485–565, 2018.

[142] E. Rojas Parra and K. Kamrin. Capturing transient granular rheology with extended fabric tensor relations. *Granular Matter*, 21(4):89, 2019.

[143] J. P. Peters, M. Muthuswamy, J. Wibowo, and A. Tordesillas. Characterization of force chains in granular material. *Physical Review E*, 72:041307, 2005.

[144] M. Pica Ciamarra, E. Lippiello, C. Godano, and L. de Arcangelis. Unjamming dynamics: The micromechanics of a seismic fault model. *Physical Review Letters*, 104:238001, 2010.

[145] T. Pöschel and S. Luding. *Granular Gases*, volume 564. Berlin, Germany: Springer, 2001.

[146] M. Pouragha, J. Duriez, A. Wautier, R. Wan, F. Nicot, and F. Darve. Preferential growth of force network in granular media. *Granular Matter*, 21(3):67, 2019.

[147] L. A. Pugnaloni, C. M. Carlevaro, M. Kramár, K. Mischaikow, and L. Kondic. Structure of force networks in tapped particulate systems of disks and pentagons. i. clusters and loops. *Physical Review E*, 93:062902, 2016.

[148] F. Radjai, D. E. Wolf, M. Jean, and J. J. Moreau. Bimodal character of stress transmission in granular packings. *Physical Review Letters*, 80:61–64, 1998.

[149] J. Ren, J. A. Dijksman, and R. P. Behringer. Reynolds pressure and relaxation in a sheared granular system. *Physical Review Letters*, 110:18302, 2013.

[150] S. Roy, S. Luding, and T. Weinhart. A general(ized) local rheology for wet granular materials. *New Journal of Physics*, 19:043014, 2017.

[151] K. Saitoh, N. Oyama, F. Ogushi, and S. Luding. Transition rates for slip-avalanches in soft athermal disks under quasi-static simple shear deformations. *Soft Matter*, 15:3487–3492, 2019.

[152] K. Saitoh, R. K. Shrivastava, and S. Luding. Rotational sound in disordered granular materials. *Physical Review E*, 99(1):012906, 2019.

[153] S. Sarkar, D. Bi, J. Zhang, R. P. Behringer, and B. Chakraborty. Origin of rigidity in dry granular solids. *Physical Review Letters*, 111:068301, Aug 2013.

[154] D. Schaeffer, T. Barker, D. Tsuji, P. Gremaud, M. Shearer, and J. M. N. T. Gray. Constitutive relations for compressible granular flow in the inertial regime. *Journal of Fluid Mechanics*, 874:926–951, 2019.

[155] J. P. Sethna, K. A. Dahmen, and C. R. Myers. Crackling noise. *Nature*, 410(6825):242–250, 2001.

[156] R. Seto, A. Singh, B. Chakraborty, M. M. Denn, and J. F. Morris. Shear jamming and fragility in dense suspensions. *Granular Matter*, 21(3):82, 2019.

[157] J. Shäfer, S. Dippel, D. E. Wolf, J. Shafer, S. Dippel, and D. E. Wolf. Force Schemes in Simulations of Granular Materials. *Journal de Physique I*, 6(1):5–20, 1996.

[158] S. Shah, C. Cheng, P. Jalali, and L. Kondic. Failure of confined granular media due to pullout of an intruder: from force networks to a system wide response. *Soft Matter*, 16:7685, 2020.

[159] L. Sibille, F. Nicot, and F. Darve. Analysis of failure occurrence from direct simulations. *European Journal of Environmental and Civil Engineering*, 13(2):187–201, 2009.

[160] L. Sibille, F. Nicot, F. V. Donze, and F. Darve. Material instability in granular assemblies from fundamentally different models. *International Journal for Numerical and Analytical Methods in Geomechanics*, 31:457–481, 2007.

[161] L. E. Silbert, D. Ertacs, G. S. Grest, T. C. Halsey, and D. Levine. Geometry of frictionless and frictional sphere packings. *Physical Review E*, 65(3):31304, 2002.

[162] A. Singh, V. Magnanimo, K. Saitoh, and S. Luding. Effect of cohesion on shear banding in quasistatic granular materials. *Physical Review E*, 90(2):022202, 2014.

[163] A. Singh, R. Mari, M. M. Denn, and J. F. Morris. A constitutive model for simple shear of dense frictional suspensions. *Journal of Rheology*, 62:457, 2018.

[164] J. H. Snoeijer, T. J. H. Vlugt, M. van Hecke, and W. van Saarloos. Force network ensemble: A new approach to static granular matter. *Physical Review Letters*, 92:054302, 2004.

[165] T. Takahashi, A. H. Clark, T. Majmudar, and L. Kondic. Granular response to impact: Topology of the force networks. *Physical Review E*, 97:012906, 2018.

[166] K. Tanaka, M. Nishida, T. Kunimochi, and T. Takagi. Discrete element simulation and experiment for dynamic response of two-dimensional granular matter to the impact of a spherical projectile. *Powder Technology*, 124:160–173, 2002.

[167] R. I. Tanner. Review article: Aspects of non-colloidal suspension rheology. *Physics of Fluids*, 30:101301, 2018.

[168] D. Taylor, F. Klimm, H. A. Harrington, M. Kramar, K. Mischaikow, M. A. Porter, and P. J. Mucha. Topological data analysis of contagion maps for examining spreading processes on networks. *Nature Communications*, 6, 2015.

[169] C. Thornton, S. J. Cummins, and P. W. Cleary. An investigation of the comparative behaviour of alternative contact force models during elastic collisions. *Powder Technology*, 210(3):189–197, 2011.

[170] B. P. Tighe, J. H. Snoeijer, T. J. H. Vlugt, and M. van Hecke. The force network ensemble for granular packings. *Soft Matter*, 6:2908–2917, 2010.

[171] A. Tordesillas, S. T. Tobin, M. Cil, K. Alshibli, and R. P. Behringer. Network flow model of force transmission in unbonded and bonded granular media. *Physical Review E*, 91:062204, 2015.

[172] A. Tordesillas, D. M. Walker, G. Froyland, J. Zhang, and R. P. Behringer. Transition dynamics of frictional granular clusters. *Physical Review E*, 86:011306, 2012.

[173] A. Tordesillas, D. M. Walker, and Q. Lin. Force cycles and force chains. *Physical Review E*, 81:011302, 2010.

[174] Y. Tsuji, T. Tanaka, and T. Ishida. Lagrangian numerical simulation of plug flow of cohesionless particles in a horizontal pipe. *Powder Technology*, 71:239–250, 1992.

[175] J. S. Urbach, R. C. Madison, and J. T. Markert. Interface depinning, self-organized criticality, and the barkhausen effect. *Physical Review Letters*, 75:276–279, 1995.

[176] M. van Hecke. Jamming of soft particles: geometry, mechanics, scaling and isostaticity. *Journal of Physics: Condensed Matter*, 22(3):033101, 2010.

[177] C. T. Veje, D. W. Howell, R. P. Behringer, S. Schöllmann, S. Luding, and H. J. Herrmann. Fluctuations and flow for granular shearing. In H. J. Herrmann, J. P. Hovi, and S. Luding, editors, *Physics of dry granular media - NATO ASI Series E 350*, page 237, Dordrecht, 1998. Kluwer Academic Publishers.

[178] P. A. Vermeer. *Continuous and Discontinuous Modelling of Cohesive-frictional Materials*, volume 568. Berlin, Germany: Springer, 2001.

[179] D. Vescovi, D. Berzi, and C. di Prisco. Fluid-solid transition in unsteady, homogeneous, granular shear flows. *Granular Matter*, 20:27, 2019.

[180] D. Vescovi and S. Luding. Merging fluid and solid granular behavior. *Soft Matter*, 12(41):8616–8628, 2016.

[181] A. Vijayan, Y. Gan, and R. K. Annabattula. Evolution of fabric in spherical granular assemblies under the inluence of various loading conditions through DEM. *Granular Matter*, 22(1):34, 2020.

[182] D. M. Walker and A. Tordesillas. Taxonomy of granular rheology from grain property networks. *Physical Review E*, 85:011304, 2012.

[183] D. M. Walker, A. Tordesillas, J. Ren, J. A. Dijksman, and R. P. Behringer. Uncovering temporal transitions and self-organization during slow aging of dense granular media in the absence of shear bands. *Europhysics Letters*, 107(1):18005, 2014.

[184] S. D. C. Walsh and A. Tordesillas. A thermomechanical approach to the development of micropolar constitutive models of granular media. *Acta mechanica*, 167(3):145–169, 2004.

[185] R. Wan and F. Nicot. Micromechanical formulation of stress dilatancy as a flow rule in plasticity of granular materials. *Journal of Engineering Mechanics*, 136(5):589–598, 2010.

[186] R. G. Wan, M. Pinheiro, and P. J. Guo. Elastoplastic modelling of diffuse instability response of geomaterials. *International Journal for Numerical and Analytical Methods in Geomechanics*, 35(2):140–160, 2011.

[187] D. Wang, J. Ren, J. A. Dijksman, H. Zheng, and R. P. Behringer. Microscopic origins of shear jamming for 2d frictional grains. *Physical Review Letters*, 120(20):208004, 2019.

[188] M. Wang, D. Wang, J. E. S. Socolar, H. Zheng, and R. P. Behringer. Jamming by shear in a dilating granular system. *Granular Matter*, 21(4):102, 2019.

[189] A. Wautier, S. Bonelli, and F. Nicot. Micro-inertia origin of instabilities in granular materials. *International Journal for Numerical and Analytical Methods in Geomechanics*, 42(9):1037–1056, 2018.

[190] T. Weinhart, R. Hartkamp, A. R. Thornton, and S. Luding. Coarse-grained local and objective continuum description of three-dimensional granular flows down an inclined surface. *Physics of Fluids*, 25(7):070605, 2013.

[191] M. Wiebicke, E. Ando, V. Smilauer, I. Herle, and G. Viggiani. A benchmark strategy for the experimental measurement of contact fabric. *Physics of Fluids*, 21(3):54, 2019.

[192] F. Xiong, P. Wang, A. H. Clark, T. Bertrand, N. T. Ouellette, M. D. Shattuck, and C. S. O'Hern. Comparison of shear and compression jammed packings of frictional disks. *Granular Matter*, 21(4):109, 2019.

[193] N. Xu and C. S. O'Hern. Measurements of the yield stress in frictionless granular systems. *Physical Review E*, 73:61303, 2006.

[194] N. Xu, C. S. O'Hern, and L. Kondic. Stabilization of nonlinear velocity profiles in athermal systems undergoing planar shear flow. *Physical Review E*, 72(4):041504, 2005.

[195] H. P. Zhang and H. A. Makse. Jamming transition in emulsions and granular materials. *Physical Review E*, 72:11301, 2005.

[196] L. Zhang, S. Cai, Z. Hu, and J. Zhang. A comparison between bridges and force-chains in photoelastic disk packing. *Soft Matter*, 10:109–114, 2014.

[197] Q. Zhang and K. Kamrin. Microscopic description of the granular fluidity field in nonlocal flow modeling. *Physical Review Letters*, 118:058001, 2017.

[198] S. Zhang and X. Cheng. Small-strain shear moduli modeling of sand: a non-equilibrium thermodynamic approach, including an application to leighton buzzard sand. *Granular Matter*, 21:68, 2019.

[199] Y. Zhang and R. P. Behringer. Pulling an intruder from granular material: a novel depinning experiment. *EPJ Web of Conferences*, 140:03040, 2017.

[200] J. Zhao and N. Guo. Unique critical state characteristics in granular media considering fabric anisotropy. *Géotechnique*, 63(8):695–704, 2013.

[201] H. Zheng, D. Wang, J. Barés, and R. P. Behringer. Jamming by compressing a system of granular crosses. *EPJ Web of Conferences*, 140:06014, 2017.

[202] W. Zylka. Gaussian approximation and brownian dynamics simulations for rouse chains with hydrodynamic interaction undergoing simple shear flow. *The Journal of Chemical Physics*, 94(6):4628–4636, 1991.